ERCOFTAC

Bulletin

September 2013   96

European Research Community on Flow, Turbulence and Combustion

ERCOFTAC is a leading European association of research, education and industry groups in the technology of flow, turbulence and combustion. The main objectives of *ERCOFTAC* are: To promote joint efforts of European research institutes and industries with the aim of **exchanging technical and scientific information**; to promote **Pilot Centres** for collaboration, stimulation and application of research across Europe; to stimulate, through the creation of **Special Interest Groups**, wellcoordinated European-wide research efforts on specific topics; to stimulate the creation of advanced training activities; and to be influential on funding agencies, governments, the European Commission and the European Parliament.

www.ercoftac.org

Honorary Presidents

Mathieu, J.   Spalding, D.B.

Executive Committee

Chairman	Tomboulides, A.
	University of Western
	Macedonia, Greece
	Tel: +30 246 105 6630
	atompoulidis@uowm.gr
	ananiast@auth.gr
Deputy Chairman	Von Terzi, D.
Deputy Chairman	Hirsch, C.
Treasurer	Hämäläinen, J.
Deputy Treasurer	Ooms, G.
SPC Chairman	Geurts, B.J.
SPC Deputy Chairman	Sagaut, P.
KNC Chairman	Hutton, A. G.
KNC Deputy Chairman	Geuzaine, P.
Horizon 10 Chairman	Jakirlic, S.
Ind. Engagement Officer	Seoud, R.E.
Knowledge Base Editor	Rodi, W.
Bulletin Editor	Elsner, W.

ERCOFTAC Seat of the Organisation

Director	Hirsch, C.
	Numeca International
	Chaussée de la Hulpe 189
	Terhulpsesteenweg
	B-1170 Brussels
	Belgium
	Tel: +32 2 643 3572
	Fax:+32 2 647 9398
	ado@ercoftac.be
Secretary	Jakubczak, M.
	magdalena.jakubczak@ercoftac.org

Scientific Programme Committee

Chairman	Geurts, B.J.
	University of Twente
	Mathematical Sciences
	PO Box 217
	NL-7500 AE Enschede
	The Netherlands
	Tel: +31 53 489 4125
	b.j.geurts@utwente.nl
Deputy Chairman	Sagaut, P.

Knowledge Network Committee (KNC)

Chairman	Hutton, A. G.
Deputy Chairman	Geuzaine, P.
	ERCOFTAC
	Crown House
	72 Hammersmith Road
	London W14 8TH
	United Kingdom
	Tel: +44 207 559 1430
	Fax:+44 207 559 1428
	richard.seoud-ieo@ercoftac.org

ERCOFTAC Central Administration Development & Office

ERCOFTAC CADO
Crown House
72 Hammersmith Road
London W14 8TH
United Kingdom
Tel: +44 207 559 1427
Fax:+44 207 559 1428

CADO Manager and Industrial Engagement Officer

Richard Seoud
Tel: +44 207 559 1430
Richard.Seoud-ieo@ercoftac.org

Admin Manager

Magdalena Jakubczak
Tel: +44 207 559 1429
Fax:+44 207 559 1428
magdalena.jakubczak@ercoftac.org

TABLE OF CONTENTS

NEXT *ERCOFTAC* EVENTS

ERCOFTAC Autumn Festival and Committee Meetings

September 26th - 27th
Cambridge, UK
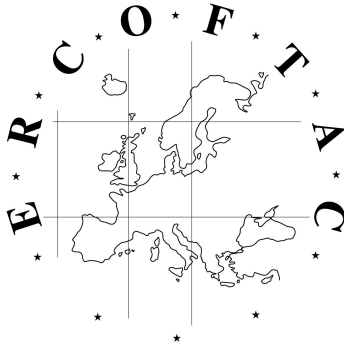
The ERCOFTAC Best Practice Guidelines for Industrial Computational Fluid Dynamics

The Best Practice Guidelines (BPG) were commissioned by ERCOFTAC following an extensive consultation with European industry which revealed an urgent demand for such a document. The first edition was completed in January 2000 and constitutes generic advice on how to carry out quality CFD calculations. The BPG therefore address mesh design; construction of numerical boundary conditions where problem data is uncertain; mesh and model sensitivity checks; distinction between numerical and turbulence model inadequacy; preliminary information regarding the limitations of turbulence models etc. The aim is to encourage a common best practice by virtue of which separate analyses of the same problem, using the same model physics, should produce consistent results. Input and advice was sought from a wide cross-section of CFD specialists, eminent academics, end-users and, (particularly important) the leading commercial code vendors established in Europe. Thus, the final document can be considered to represent the consensus view of the European CFD community.

Inevitably, the Guidelines cannot cover every aspect of CFD in detail. They are intended to offer roughly those 20% of the most important general rules of advice that cover roughly 80% of the problems likely to be encountered. As such, they constitute essential information for the novice user and provide a basis for quality management and regulation of safety submissions which rely on CFD. Experience has also shown that they can often provide useful advice for the more experienced user. The technical content is limited to single-phase, compressible and incompressible, steady and unsteady, turbulent and laminar flow with and without heat transfer. Versions which are customised to other aspects of CFD (the remaining 20% of problems) are planned for the future.

The seven principle chapters of the document address numerical, convergence and round-off errors; turbulence modelling; application uncertainties; user errors; code errors; validation and sensitivity tests for CFD models and finally examples of the BPG applied in practice. In the first six of these, each of the different sources of error and uncertainty are examined and discussed, including references to important books, articles and reviews. Following the discussion sections, short simple bullet-point statements of advice are listed which provide clear guidance and are easily understandable without elaborate mathematics. As an illustrative example, an extract dealing with the use of turbulent wall functions is given below:

- Check that the correct form of the wall function is being used to take into account the wall roughness. An equivalent roughness height and a modified multiplier in the law of the wall must be used.

- Check the upper limit on $y+$. In the case of moderate Reynolds number, where the boundary layer only extends to $y+$ of 300 to 500, there is no chance of accurately resolving the boundary layer if the first integration point is placed at a location with the value of $y+$ of 100.

- Check the lower limit of $y+$. In the commonly used applications of wall functions, the meshing should be arranged so that the values of $y+$ at all the wall-adjacent integration points is only slightly above the recommended lower limit given by the code developers, typically between 20 and 30 (the form usually assumed for the wall functions is not valid much below these values). This procedure offers the best chances to resolve the turbulent portion of the boundary layer. It should be noted that this criterion is impossible to satisfy close to separation or reattachment zones unless $y+$ is based upon $y*$.

- Exercise care when calculating the flow using different schemes or different codes with wall functions on the same mesh. Cell centred schemes have their integration points at different locations in a mesh cell than cell vertex schemes. Thus the $y+$ value associated with a wall-adjacent cell differs according to which scheme is being used on the mesh.

- Check the resolution of the boundary layer. If boundary layer effects are important, it is recommended that the resolution of the boundary layer is checked after the computation. This can be achieved by a plot of the ratio between the turbulent to the molecular viscosity, which is high inside the boundary layer. Adequate boundary layer resolution requires at least 8-10 points in the layer.

All such statements of advice are gathered together at the end of the document to provide a 'Best Practice Checklist'. The examples chapter provides detailed expositions of eight test cases each one calculated by a code vendor (viz FLUENT, AEA Technology, Computational Dynamics, NUMECA) or code developer (viz Electricité de France, CEA, British Energy) and each of which highlights one or more specific points of advice arising in the BPG. These test cases range from natural convection in a cavity through to flow in a low speed centrifugal compressor and in an internal combustion engine valve.

Copies of the Best Practice Guidelines can be acquired from:

ERCOFTAC CADO
Crown House
72 Hammersmith Road
London W14 8TH, United Kingdom

Tel: +44 207 559 1429
Fax: +44 207 559 1428
Email: magdalena.jakubczak@ercoftac.org

The price per copy (not including postage) is:

ERCOFTAC members

First copy	*Free*
Subsequent copies	75 Euros
Students	75 Euros

Non-ERCOFTAC academics	140 Euros
Non-ERCOFTAC industrial	230 Euros
EU/non EU postage fee	10/17 Euros

Special Theme: Reactive Flows and Combustion

C. Angelberger

IFP Energies Nouvelles, France

A main driver for combustion research in past decades has been the constantly increasing urge to limit the negative environmental impacts related to industrial combustion (including energy generation, the process industry, and air and surface transport), and at increasing its efficiency in order to limit fossil fuel consumption and reduce greenhouse gas emissions. This has led to extensive research exploiting advanced experimental and numerical techniques to explore the complex, non-linear fundamental mechanisms at stake in turbulent combustion of complex hydrocarbon fuels.

This research has not only led to an increased detailed understanding of the fundamentals of turbulent combustion. Its exploitation increasingly allows predicting the operation of industrial combustion devices under real operating conditions (industrial furnaces, gas turbines, piston engines), thus opening unprecedented means of designing, optimising and controlling them.

Despite the fact that environmental issues are major drivers for combustion research, other aspects come into play for many applications. The foremost objective of fire safety research is for example to predict the onset and development of fires in domestic and industrial contexts, with the aim of devising means to limit related destruction and life hazards by design or via efficient and selective fire fighting techniques. A longstanding major issue at stake in rocket engines is combustion instability, that may result from interactions between fluid flow, solid or liquid combustion, acoustics and fluid-structure interactions under extreme conditions. In general, issues as thermal loading of walls, stability and safety are also key drivers for combustion research.

The aim of the present special issue of the ERCOFTAC Bulletin is to propose a view at selected research activities carried out in Europe in the domain of reactive flows and combustion.

The topic covered in the first two articles is the development of numerical models describing specific aspects of turbulent combustion, namely the misalignment between stress and strain fields for variable density flows found in combustion, and the evolution of flame-turbulence interaction in premixed turbulent combustion, as developed by University of Manchester in collaboration with EDF.

Detailed and quantitative experimental studies are instrumental for acquiring fundamental understanding and supporting model validation work. Technical University of Darmstadt contributes an article summarising a detailed study of flame-wall interactions of premixed methane/air flames using Laser spectroscopy. Delft University of Technology proposes a contribution describing an experimentak study of the morphology of a liquid spray injected into a hot diluted coflow with low oxygen concentration by means of Phase Doppler Anemometry.

Large-Eddy Simulation has become a widely developed approach to study mixing and combustion in flames typical of stationary applications, and is the topic of three contributions. Technical U. of Darmstadt, in collaboration with Universities of Gabes and Sidney, present an investigation of spray formation and turbulent burning of a diluted ethanol spray with a FGM approach. Technical University of Munich presents the development and validation of a LES turbulent combustion model based on tabulated chemistry and a stochastic fields approach, especially aimed at reproducing auto-ignition lengths and regimes. CORIA uses LES to study the flame structure in a turbulent bluff-body flame with different equivalence ratio stratifications, based on a filtered laminar flame PDF model.

Piston engine combustion is another typical field of research in the combuston community. The Swiss Federal Institute of Technology in Zurich, in collaboration with Wärtsilä Switzerland Ltd., presents a joint experimental and numerical study of the impact of injector nozzle hole diameters on combustion in a marine Diesel engine.

Two articles provided by Institut de Mécanique des Fluides in Toulouse and Universität der Bundeswehr in Munich discuss different aspects of performing simulations of mixing and combustion under the supercritical conditions found in rocket engines.

Finally, the contribution from Ghent University summarises experimental research aimed at a detailed characterisation of well controlled and instrumented apartment fires, aimed at supporting models able to describe them in the view of fire forecasting.

Without pretending to be in any way exhaustive, we believe the presented articles illustrate the excellence of European research in this domain, and how it contributes addressing major industrial and societal challenges.

A Stress-strain Lag Eddy Viscosity Model for Variable Density Flow

M. Assad [1], R. Prosser [1], A. Revell [1] and B. Sapa[2]

[1] *Modelling and Simulation Centre, School of MACE, University of Manchester, M13 9PL, UK*
[2] *Electric de France, 6 quai Watier, 78491, Chatou, France.*

Abstract

A modified eddy viscosity model is proposed to model the misalignment between stress and strain fields for variable density flows. The stress-strain misalignment is quantified by introducing a C_{as} parameter. A transport equation for C_{as} is derived from a full Reynolds stress model (RSM). The C_{as} transport equation is coupled to a standard EVM model (e.g, $k - \omega\ SST$). The performance of the proposed model is investigated via a turbulent buoyant plume.

1 Introduction

Variable density flow has many industrial applications such as incidental fires. The incidental fires are unsteady complex phenomena of combustion that include turbulence and combustion chemistry interaction. Fires modelling involves modelling of combustion chemistry and turbulent buoyant flow. The buoyant plumes are usually used to study the buoyancy effects in the incidental fires.

The incidental fires and buoyant plume include high density fluctuations which significantly increase the unsteadiness and anisotropy of the flow which, in turn, impacts on flow properties such as Reynolds stresses. Two main types of CFD model may be used to capture flow unsteadiness; Reynolds-averaged Navier-Stokes (RANS), and Large Eddy simulations (LES). Using LES for variable density flow simulation is still computationally expensive for industrial applications due to the fine grids that must be used. RANS models are widely used and are computationally cheaper compared to LES models. RANS models historically have been developed for cold flows and then modified for hot flows to include buoyancy effects; many studies have applied Eddy Viscosity Models (especially the $k - \varepsilon$ model) to variable density flow [1, 2, 3, 4, 5, 6]. In the derivation of standard eddy viscosity models for steady quasi-equilibrium flows, several fundamental assumptions are used, such as isotropy of the normal stresses [7]. These assumptions no longer hold for variable density flow due to the anisotropy in Reynolds stress distributions. Reynolds stress models improve Reynolds stress predictions, which leads to improvement in the prediction of turbulence energy distribution [7]. However, Reynolds stress models are computationally expensive due to the requirement for solving an additional five transport equations, and the special numerical treatments required to make the calculation converge. An alternative simplified approach has been introduced by Revell [8] to codify the misalignment between induced stress and strain fields. The C_{as} model provides a new EVM which has been applied to cold flow applications, and improved results have been observed when compared to standard EVM approaches. [7, 8, 9, 10]. The C_{as} model is suitable for large mean flow unsteadiness, and is cheaper to compute than RSM models [7].

The aims of the present work are; to develop a C_{as} model for variable density flows that predicts the anisotropy and unsteadiness effects and; to quantify the misalignment between the stress and strain tensors for hot flows, by introducing a C_{as} parameter that can be modelled locally in the flow field. This parameter can be introduced to derive a new transport equation based on the Favre-averaged Reynolds stress transport equation. The proposed equation is solved in conjunction with classical EVM models. The model performance is compared to different RANS models for a turbulent buoyant plume.

2 Derivation of stress strain lag model

2.1 Background

For classical EVM models the production rate of the turbulence kinetic energy P_k is related to the square of the strain rate $\widetilde{S_{ij}}$. In the case of Reynolds stress models, the production rate is related linearly to the strain rate $\widetilde{S_{ij}}$. Classical EVM models thus overestimate the production rate of the turbulence kinetic energy P_k in the presence of high strain rate [9, 11], and different models have been proposed to correct the overestimate, as in the linear production model by Guiment and Laurence [11]. However, such models do not consider the effect of stress-strain lag in the unsteady flow.

The C_{as} model introduces the turbulence production rate as $P_k = \bar{\rho} C_{as} \widetilde{k} \|\widetilde{S}\|$, where C_{as} is a non-dimensional parameter representing the alignment between the stress and strain fields:

$$C_{as} = -\frac{\widetilde{a}_{ij}\widetilde{S}_{ij}}{\|\widetilde{S}\|}, \tag{1}$$

$$\widetilde{a}_{ij} = \frac{\widetilde{u_i'' u_j''}}{\widetilde{k}} - \frac{2}{3}\delta_{ij}, \widetilde{S}_{ij} = \left(\frac{\partial \widetilde{u}_i}{\partial x_j} + \frac{\partial \widetilde{u}_j}{\partial x_i}\right), \tag{2}$$

where $\widetilde{a}_{ij}$ is the stress anisotropy, $\widetilde{k} = \frac{1}{2}\widetilde{u_i'' u_i''}$ is the turbulent kinetic energy, δ_{ij} is the Kronecker delta function, $\widetilde{S}_{ij}$ is the strain rate and $\|\widetilde{S}\| = \sqrt{2\widetilde{S}_{ij}\widetilde{S}_{ij}}$ is the strain

invariant. For variable density flow, the strain rate tensor is replaced by the traceless form as

$$\widetilde{S}_{ij} = \left(\frac{\partial \widetilde{u}_i}{\partial x_j} + \frac{\partial \widetilde{u}_j}{\partial x_i} - \frac{1}{3} \frac{\partial \widetilde{u}_k}{\partial x_k} \delta_{ij} \right) \quad (3)$$

The effects of stress strain misalignment have been reviewed in [7, 12].

2.2 Derivation of the C_{as} model

The derivation of the C_{as} model starts with the total derivative of 1:

$$\frac{DC_{as}}{Dt} = -\frac{1}{\|\widetilde{S}\|} \left(\widetilde{a}_{ij} \frac{D\widetilde{S}_{ij}}{Dt} + \widetilde{S}_{ij} \frac{D\widetilde{a}_{ij}}{Dt} + C_{as} \frac{D\|\widetilde{S}\|}{Dt} \right). \quad (4)$$

The total derivative of the stress anisotropy $\widetilde{a}_{ij}$ in 4 can be written as

$$\frac{D\widetilde{a}_{ij}}{Dt} = \frac{1}{\bar{\rho}\widetilde{k}} \left(\frac{D\overline{\rho u_i'' u_j''}}{Dt} - \frac{\widetilde{u_i'' u_j''}}{\widetilde{k}} \frac{D\bar{\rho}\widetilde{k}}{Dt} \right). \quad (5)$$

The total derivative of the turbulence kinetic energy $\widetilde{k}$ is

$$\frac{D\bar{\rho}\widetilde{k}}{Dt} = \underbrace{\frac{\partial}{\partial x_k} \left(\left(\mu + \frac{\mu_t}{\sigma_k} \right) \frac{\partial \widetilde{k}}{\partial x_k} \right) + P_k - \bar{\rho}\widetilde{\varepsilon}}_{D_k}$$
$$\underbrace{-\overline{u_j''}(\frac{\partial \bar{p}}{\partial x_j} + \rho_\infty g_j)}_{G_k}, \quad (6)$$

where $\widetilde{\varepsilon}$ is the dissipation rate and G_k is the effect of buoyancy on production of kinetic energy, which can be approximated using a number of different models. The total derivative of Favre-averaged Reynolds stress equation $\widetilde{u_i'' u_j''}$ is

$$\frac{D\bar{\rho}\widetilde{u_i'' u_j''}}{Dt} = -\underbrace{\left(\bar{\rho}\widetilde{u_k'' u_i''} \frac{\partial \widetilde{u}_j}{\partial x_k} + \bar{\rho}\widetilde{u_k'' u_j''} \frac{\partial \widetilde{u}_i}{\partial x_k} \right)}_{P_{ij}} - \underbrace{\overline{\rho\varepsilon_{ij}}}_{\bar{\chi}_{ij}}$$
$$- \underbrace{\frac{\partial}{\partial x_k} \left(\overline{\rho u_i'' u_j'' u_k''} \right)}_{D_{ij}} - \underbrace{\left(\overline{u_i'' \frac{\partial p'}{\partial x_j}} + \overline{u_j'' \frac{\partial p'}{\partial x_i}} \right)}_{\phi_{ij}}$$
$$+ \underbrace{\left(\overline{u_i'' \frac{\partial \bar{p}}{\partial x_j}} + \overline{u_j'' \frac{\partial \bar{p}}{\partial x_i}} \right)}_{G_{ij}}, \quad (7)$$

where P_{ij} is production rate of the Reynold stress $\widetilde{u_i'' u_j''}$ and is an exact term need no modelling, $\bar{\chi}_{ij} = \frac{2}{3}\bar{\rho}\widetilde{\varepsilon}\delta_{ij}$ is the tensorial dissipation rate (assumed to be isotropic as in the constant density case [13]), ϕ_{ij} is the pressure-strain correlation which acts to redistribute the turbulence energy and G_{ij} is the fluctuating velocity-pressure gradient correlation representing buoyancy effects, and is equal to zero in the constant density case. 6 and 7 can be used to rewrite the transport equation of stress anisotropy as

$$\frac{D\widetilde{a}_{ij}}{Dt} = \frac{1}{\bar{\rho}\widetilde{k}} \left(D_{ij} + G_{ij} + P_{ij} + \phi_{ij} - \bar{\chi}_{ij} \right) - \frac{1}{\bar{\rho}\widetilde{k}}$$
$$\times \left(\left(\widetilde{a}_{ij} + \frac{2}{3}\delta_{ij} \right) \left(P_k + D_k - \bar{\rho}\widetilde{\varepsilon} + G_k \right) \right), \quad (8)$$

and 8 finally allows 4 to be rewritten as

$$\frac{DC_{as}}{Dt} = -\frac{1}{\|\widetilde{S}\|} \left(\widetilde{a}_{ij} + \frac{2C_{as}\widetilde{S}_{ij}}{\|\widetilde{S}\|} \frac{D\widetilde{S}_{ij}}{Dt} \right) \frac{D\widetilde{S}_{ij}}{Dt}$$
$$- \frac{\widetilde{S}_{ij}}{\bar{\rho}\widetilde{k}\|\widetilde{S}\|} \left(P_{ij} - \frac{2}{3}P_k\delta_{ij} + \widetilde{a}_{ij} \left(P_k - \bar{\rho}\widetilde{\varepsilon} \right) \right)$$
$$- \frac{\widetilde{S}_{ij}}{\bar{\rho}\widetilde{k}\|\widetilde{S}\|} \left(\left(\widetilde{a}_{ij} + \frac{2}{3}\delta_{ij} \right) \left(D_k + G_k \right) \right)$$
$$- \frac{\widetilde{S}_{ij}}{\bar{\rho}\widetilde{k}\|\widetilde{S}\|} \left(D_{ij} + G_{ij} + \phi_{ij} \right). \quad (9)$$

The production rate P_{ij} can be written as

$$P_{ij} = -\bar{\rho}\widetilde{k} \left(\frac{4}{3}\widetilde{S}_{ij} + \widetilde{a}_{ik}\widetilde{S}_{kj} + \widetilde{a}_{ki}\widetilde{\Omega}_{jk} + \widetilde{S}_{ik}\widetilde{a}_{kj} + \widetilde{\Omega}_{ik}\widetilde{a}_{jk} \right), \quad (10)$$

where $\widetilde{\Omega}_{ij} = \frac{1}{2} \left(\partial \widetilde{u}_i/\partial x_j - \partial \widetilde{u}_j/\partial x_i \right)$ is the vorticity tensor. The pressure-strain term ϕ_{ij} for variable density flow may be written as [13, 14, 15]:

$$\phi_{ij} = \phi_{ij,1} + \phi_{ij,2} + \phi_{ij,3} + \phi_{ij,4}, \quad (11)$$

where

$$\phi_{ij,1} + \phi_{ij,2} = \overline{u_i'' \frac{\partial p'}{\partial x_j}} + \overline{u_j'' \frac{\partial p'}{\partial x_i}} - \frac{2}{3}\delta_{ij}\overline{u_k' \frac{\partial p'}{\partial x_k}}, \quad (12)$$

$$\phi_{ij,3} = \frac{2}{3}\delta_{ij}\overline{p' \frac{\partial u_k'}{\partial x_k}}, \quad (13)$$

$$\phi_{ij,4} = -\frac{2}{3}\delta_{ij}\overline{p' u_k'}. \quad (14)$$

The terms $\phi_{ij,1}$ and $\phi_{ij,2}$ are the slow and rapid pressure-strain terms respectively, which can be combined and approximated as in constant density flow [13, 14, 15]:

$$\phi_{ij,1} + \phi_{ij,2} = -C_1\bar{\rho}\widetilde{\varepsilon}\widetilde{a}_{ij} - C_1^*\bar{\rho}P_k\widetilde{a}_{ij} + C_2\bar{\rho}\widetilde{\varepsilon} \left(\widetilde{a}_{ik}\widetilde{a}_{kj} \right)$$
$$- C_2\bar{\rho}\widetilde{\varepsilon} \left(\frac{1}{3}\delta_{ij}A_2 \right) + \left(C_3 - C_3^*\sqrt{A_2} \right) \bar{\rho}\widetilde{k}\widetilde{S}_{ij}$$
$$+ C_4\bar{\rho}\widetilde{k} \left(\widetilde{a}_{ik}\widetilde{S}_{jk} + \widetilde{a}_{jk}\widetilde{S}_{ik} - \frac{2}{3}\widetilde{a}_{lm}\widetilde{S}_{lm}\delta_{ij} \right)$$
$$+ C_5\bar{\rho}k \left(\widetilde{a}_{ik}\widetilde{\Omega}_{jk} + \widetilde{a}_{jk}\widetilde{\Omega}_{ik} \right), \quad (15)$$

where A_2 is the second invariant of the stress tensor $\widetilde{a}_{ij}\widetilde{a}_{ij}$ and the constants $C_1, \dots, C_5$ can be obtained from the LRR [16] or SSG [17] closures. The pressure-strain terms $\phi_{ij,3}$ and $\phi_{ij,4}$ are only required for reacting flow and represent the interaction of the heat release with mixing; more details can be found in [14, 18].

The general transport equation for C_{as} can therefore be rewritten as

$$\frac{DC_{as}}{Dt} = \alpha_1\frac{\widetilde{\varepsilon}}{\widetilde{k}}C_{as} + \alpha_1^*\|\widetilde{S}\|C_{as}^2 - \alpha_2\frac{\widetilde{S}_{ij}\widetilde{a}_{ik}\widetilde{a}_{kj}}{\eta}$$
$$+ \left(\alpha_3 + \alpha_3^*\sqrt{A_2} \right) \|\widetilde{S}\| + \alpha_4\frac{\widetilde{S}_{ij}\widetilde{a}_{ik}\widetilde{S}_{jk}}{\|\widetilde{S}\|}$$
$$+ \alpha_5\frac{\widetilde{S}_{ij}\widetilde{a}_{ik}\widetilde{\Omega}_{jk}}{\|\widetilde{S}\|} - \frac{1}{\|\widetilde{S}\|}\frac{D\widetilde{S}_{ij}}{Dt} \left(\widetilde{a}_{ij} + \frac{2C_{as}\widetilde{S}_{ij}}{\|\widetilde{S}\|} \right)$$
$$- \frac{\widetilde{S}_{ij}}{\bar{\rho}\widetilde{k}\|\widetilde{S}\|} \left(\left(\widetilde{a}_{ij} + \frac{2}{3}\delta_{ij} \right) \left(D_k + G_k \right) \right)$$
$$- \frac{\widetilde{S}_{ij}}{\bar{\rho}\widetilde{k}\|\widetilde{S}\|} \left(D_{ij} + G_{ij} + \phi_{ij,3} + \phi_{ij,4} \right), \quad (16)$$

where $\eta = \widetilde{k}\|\widetilde{S}\|/\widetilde{\varepsilon}$ is a strain rate parameter and $\alpha_1, \alpha_1^*, \alpha_2, \alpha_3, \alpha_3^*, \alpha_4, \alpha_5$ are new constants (see 1) related to constants $(C_1, \ldots, C_5)$ in the LRR (or SSG) pressure-strain closures as

$$\alpha_1 = (1 + C_1), \quad \alpha_1^* = (1 - C_1^*), \quad \alpha_2 = C_2,$$
$$\alpha_3 = \frac{\left(\frac{4}{3} - C_3\right)}{2}, \quad \alpha_3^* = \frac{C_3^*}{2}, \quad \alpha_4 = 2(1 - C_4),$$
$$\alpha_5 = 2(1 - C_5). \tag{17}$$

Table 1: Coefficients of the C_{as} model, based on the SSG [17] and LRR [16] pressure-strain models

	α_1	α_1^*	α_2	α_3	α_3^*	α_4	α_5
C_{as} LRR	-0.8	0	0	0.267	0	0.254	0.69
C_{as} SSG	-0.7	-1.9	1.05	0.267	0.325	0.75	1.6

The third-order moment correlation $T_{ijk} = \overline{\rho u_i'' u_j'' u_k''}$ can be expressed using the General Gradient Diffusion Hypothesis (GGDH) model as in the constant density case [13, 14, 15]:

$$T_{ijk} = C_s \frac{\bar{\rho}\widetilde{k}}{\widetilde{\varepsilon}} \left(\widetilde{u_k'' u_l''} \frac{\partial \widetilde{u_i'' u_j''}}{\partial x_l} \right), \tag{18}$$

where C_s is an empirical constant usually assigned the value 0.22 [13].

The implicit buoyancy effects in the transport equation for C_{as} are included in the fluctuating velocity-pressure gradient terms G_{ij} and G_k. The velocity fluctuation $\overline{u_i''}$ can be modelled either using simple gradient diffusion hypothesis (SGDH) or General Gradient Diffusion Hypothesis (GGDH) model as in 19[6]. The GGDH model take into account the effect of stress anisotropy, whereas the SGDH model assume an isotropic stress distribution:

$$\text{SGDH} \quad \overline{u_i''} = \frac{\mu_t}{\sigma_t \bar{\rho}^2 \widetilde{k}} \frac{\partial \bar{\rho}}{\partial x_k},$$
$$\text{GGDH} \quad \overline{u_i''} = \frac{3}{2} \frac{\mu_t}{\sigma_t \bar{\rho}^2 \widetilde{k}} \left(\widetilde{u_i'' u_k''} \frac{\partial \bar{\rho}}{\partial x_k} \right), \tag{19}$$

where μ_t is the turbulent viscosity and σ_t is the turbulent Prandtl number which usually have the value 0.85.

The transport equation of C_{as} for the variable density case (16) is similar to the equation proposed for constant density flow (see [8], for details), differing only in the term which represent buoyancy and diffusion terms arising from $\widetilde{u_i'' u_j''}$ and $\widetilde{k}$ equations. Revell [7] combined and approximated both the diffusion terms using SGDH as

$$Diff^{C_{as}} = \frac{\partial}{\partial x_k} \left[(\mu + \mu_t \sigma_{c_{as}}) \frac{\partial C_{as}}{\partial x_k} \right], \tag{20}$$

where $\sigma_{C_{as}} = 0.2$ is a constant. In this work the diffusion terms of are modelled as mention above (see 18 and 6).

The stress anisotropy in 16 can be closed either using a linear or non-linear EVM formulation. The cubic EVM [19] is a suitable model which yields a better prediction of the normal stress anisotropy compared with the classical linear EVM model.

2.3 The $SST - C_{as}$ model

To achieve the desired features of the C_{as} model, the transport equation for C_{as} is coupled and solved with a two-equation EVM model. In this work the shear-stress transport turbulence model (SST) is used due to its ability to predict more complex flow [20]. The coupled model is referred to as the $SST - C_{as}$.

Menter [20] defined the turbulent eddy viscosity for the SST model as

$$\mu_t = \bar{\rho}\widetilde{k} \min\left(\frac{1}{\omega}; \frac{a_1}{\|\widetilde{S}\|F_2} \right), \tag{21}$$

where $a_1 = 0.31$ is a model constant and F_2 is a blending function with a zero value at free shear layers and unity at the wall. The effect of stress-strain misalignment is incorporated into the SST model by modifying the turbulent eddy viscosity as

$$\mu_t = \bar{\rho}\widetilde{k} \min\left(\frac{1}{\omega}; \frac{a_1}{\|\widetilde{S}\|F_2}; \frac{C_{as}}{\|\widetilde{S}\|} \right). \tag{22}$$

The value of C_{as} in 22 is limited to ± 0.31 due to the limiting value in the boundary layer which is used for the calculation of P_k [12]. The negative value of C_{as} leads to negative production rate, but it might cause numerical instabilities which have been noticed for the cold flow calculation [7]. Hence, the limiter $\max(C_{as}, 0.0)$ is used for calculation of the turbulent diffusion terms and stress anisotropy to stabilise the calculation.

In the $SST - C_{as}$ model, the dissipation rate in 16 is calculated as $\widetilde{\varepsilon} = 0.09\widetilde{k}\omega$.

3 Numerical method

The simulations in this work were performed using *Code_Saturne*, an open-source CFD code developed by EDF [21]. *Code_Saturne* is an incompressible solver based on a collocated discretisation for the space domain and able to deal with structured and unstructured meshes. It employs either RANS or LES models to solve the turbulent Navier-Stokes equation for both reacting and non-reacting flows. An implicit Euler scheme is used for time discretisation. A second order centred difference scheme (CDS) is used for the convective terms. An improved Favre-averaged URANS algorithm (see [3, 22] for details) is used to account for the effect of thermal expansion in the continuity equation under a low Mach number assumption.

A number of RANS turbulence models which include the buoyancy effects are available in *Code_Saturne*; the standard $k - \varepsilon$ model [23], the SST model [20] and the quasi-linear SSG model [17]. These models were used as bases for comparison with the $SST - C_{as}$ model.

4 Turbulent buoyant plume

Accurate prediction of non-reacting buoyant plumes is an important precursor to understanding convective transport of fluids in fire prediction. In cases where the prediction of fire spreading rates and movement of smoke plume are required, the simulation can be simplified and cost can be minimised by modelling non-reacting buoyant plumes [6, 24, 25].

The turbulent buoyant plume itself has been the subject of many investigations in both experimental and
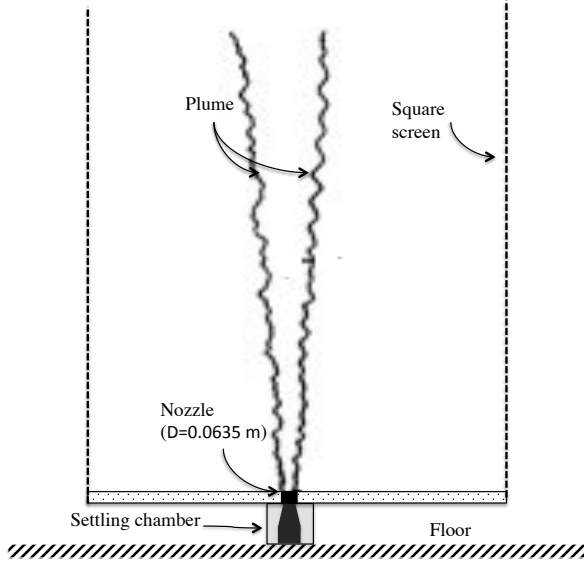
Figure 1: A Schematic sketch of the experimental facility for the thermal plume [28].

Figure 2: The computational domain for the axisymmetric plume.

numerical studies. There are many numerical studies undertaken for turbulent buoyant plumes using RANS models. Most of these works used EVM models (mainly the standard $k - \varepsilon$ model) with modifications related to the buoyancy terms [6, 24]. RSM models have been used in a limited number of studies to predict thermal plume behaviours, such as Milan and Younis [26]. More details about these numerical studies (and others) can be found in [25].

4.1 Case description

This test case has been experimentally studied by William and George [27] (see Figure 1 for the test configuration) to measure mean and fluctuating quantities for the buoyant plume at different heights above the nozzle exit. The plume is assumed to be axisymmetric without swirl, and profiles similarity have been established. The air flow enters a settling chamber heated it. The hot air is discharged into the room (ambient air at rest) through a nozzle ($D = 0.0635\,m$) at an average normal velocity $\widetilde{w} = 0.67\,m/s$ and turbulence intensity $I = 0.5\%$, and a temperature of $573.15 \pm 1\,K$. The average Reynolds number of the inlet air is 870 and the densitometric Froude number is 1.4. The plume is assumed to be fully developed above a distance $12D$ and to have reached a self-similar state where the non-dimensional analysis can be applied.

4.2 Numerical setup

An axisymmetric domain (r=1 m, L=3 m) with structured mesh is used to simulate the buoyant plume as shown in Figure 2. The computational domain is meshed with 19200 cells; 80 cells in the radial direction and 240 cells in the vertical direction, with a refined grid close to the nozzle exit and plume centre-line. The ambient air in the computational domain has a temperature of $302\,K$, a turbulent kinetic energy of $10^{-6}\,m^2/s^2$ and a turbulent dissipation rate of $10^{-9}\,m^2/s^3$. The inlet boundary condition for the hot air is imposed with a wall boundary around the nozzle. Neumann boundary conditions are specified for the outlet flow, with static pressure boundaries allowing flow into and out of the domain. The profiles of velocity, temperature and turbulence quantities
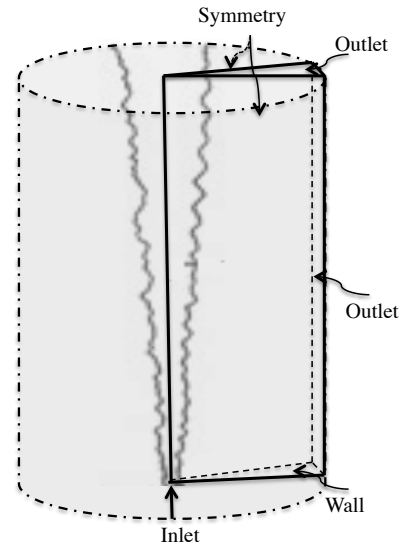
for the inlet flow were obtained from a 1D channel flow simulated for the same conditions. The simulations were run in the transient mode until steady-state conditions were achieved. The plume density is calculated using the ideal gas law as

$$\rho = \frac{P \, (M_W)_{air}}{R_0 T}, \tag{23}$$

where $R_0 = 8.314\,J/mole.K$ is the universal gas constant and $(M_W)_{air}$ is the molecular weight of air. The calculations were performed with classical RANS models: the $k - \varepsilon$ model, the SST model and the SSG model. The test case is also simulated using the proposed $SST - C_{as}$ model described in Section 2. The non-dimensionalising quantities used through this paper are:

$$\text{normalised mean vertical velocity} = \widetilde{w} F_0^{-1/3} z^{1/3},$$
$$\text{normalised mean temperature} = \beta \triangle T \, F_0^{-2/3} z^{5/3},$$
$$\text{normalised turbulent kinetic energy} = \widetilde{k} F_0^{-2/3} z^{2/3},$$
$$\text{normalised radial turbulent stress} = \widetilde{u''^2} F_0^{-2/3} z^{2/3}, \tag{24}$$

where $\widetilde{w}$ is mean vertical velocity, $F_0 = 0.01\,m^4/s^3$ is the integrated buoyancy flux at the source (nozzle) [28], z is the height, g is the gravitational acceleration, $\triangle T$ the temperature difference between the local and the ambient, and $\beta \approxeq \frac{1}{T_\infty}$ is the thermal expansion coefficient.

The turbulent buoyant plume reaches the self-similar state at $z = 1.75\,m$ above the exit nozzle [5, 18]. Hence, the normalised profiles of mean and fluctuating quantities are calculated at $z = 1.75\,m$ for all the simulations in this work.

4.3 Results

Figures 3, 4, 5 and 6 provide a comparison of the original SST model and the proposed $SST - C_{as}$ model with the experimental data for the normalised profiles of mean vertical velocity, temperature, turbulent kinetic energy and radial turbulent normal stress, respectively.

In Figure 3, the original SST model underpredicts the vertical velocity close to the plume centreline, whereas
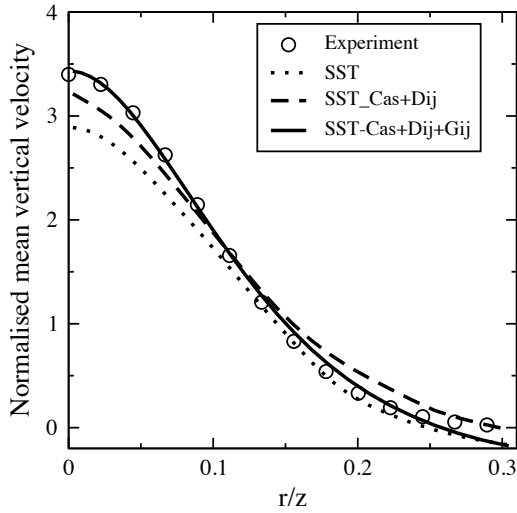
Figure 3: Normalised mean vertical velocity profile at axial position $z = 1.75\,m$.

Figure 4: Normalised temperature profile at axial position $z = 1.75\,m$.

Figure 5: Normalised turbulent kinetic energy profile at axial position $z = 1.75\,m$.
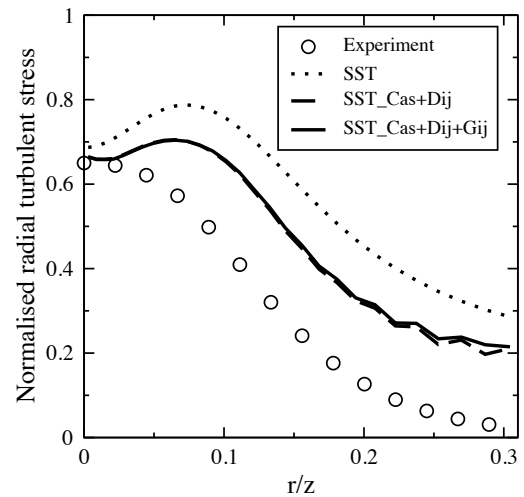
Figure 6: Normalised radial turbulent normal stress profile at axial position $z = 1.75\,m$.

the proposed $SST - C_{as}$ model shows good agreement with the experimental data. Adding the diffusion term D_{ij} to $SST - C_{as}$ improves the model prediction. Additional improvements are obtained with the buoyancy effect term G_{ij} in the C_{as} transport equation. The $SST - C_{as}$ model improves the prediction of vertical velocity by 20% at the plume centreline compared with the SST model.

In Figure 4, the temperature profile is overestimated by the original SST model. The $SST - C_{as}$ model shows a slightly improvement. This improvement can be related to the new formulation of turbulent viscosity μ_t which explicitly controls the turbulent scalar flux in the energy equation. The new buoyancy term in the C_{as} transport equation shows stronger effects close to the plume centreline due to the high density gradient, which decreases far from plume centreline.

The profiles of the normalised turbulent kinetic energy in Figure 5 are in poor agreement with the experimental data for both the original SST model and the $SST - C_{as}$ model. The $SST - C_{as}$ model reduces the value of turbulent kinetic energy close to the plume centreline, which is expected, whereas the classical EVM models usually overpredict the value of turbulent kinetic energy in the

presence of strong strain rate. A similar prediction pattern is observed for the profile of the radial turbulent normal stress in Figure 6. The $SST - C_{as}$ model yields a better prediction of the radial turbulent normal stress due to its ability to capture the anisotropy of these normal stresses over the classical EVM.

Figures 7 and 8 present the profiles of the normalised mean vertical velocity and temperature, respectively, which were obtained with different RANS models. The predicted profile of the normalised temperature and vertical velocity for the SSG model are overpredicted close to the plume centreline and underpredicated far from the centreline. The SSG model yields a high value of normalised velocity and temperature close to the centreline, which indicates a poor prediction of growth rate of the axisymmetric jet. This may be attributed to the numerical effects of the coordinate singularity, such was noticed in [26]. To overcome this effect a 3D simulation is currently being undertaken (ongoing work). A similar pattern is also predicted for the normalised velocity profile using the $k - \varepsilon$ model, but the $k - \varepsilon$ model is in better agreements with experimental data. The $SST - C_{as}$ model generally provide a better prediction for the mean and fluctuating quantities compared to the SSG and classical EVM.
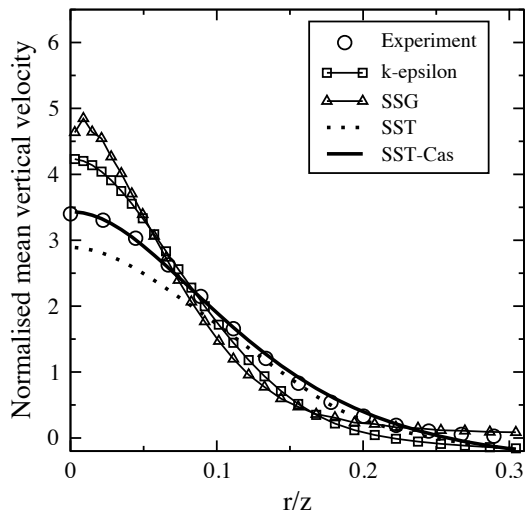
Figure 7: Normalised mean axial profile at axial position $z = 1.75\,m$.
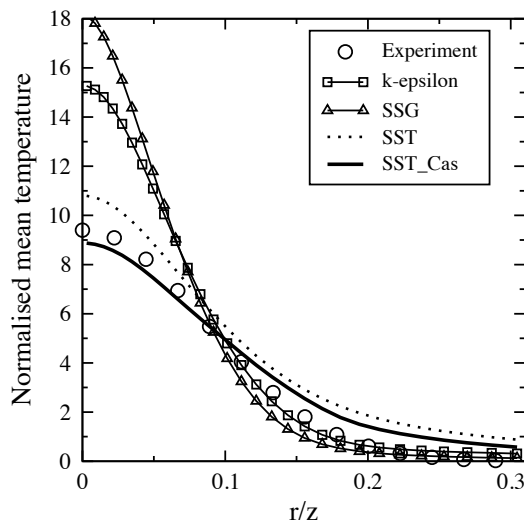
Figure 8: Normalised temperature profile at axial position $z = 1.75\,m$.

5   Conclusions

In this paper, the $SST - C_{as}$ model has been developed and extended to hot flows. The Favre-averaged transport equation for C_{as} was derived and closed by modelling the newly emergent terms. A turbulent buoyant plume was simulated using RANS models. The behaviour of the proposed model shows a significant improvement for velocity and temperature profiles over the classical EVM models. The level of unsteadiness for the turbulent buoyant plume is however not enough to show significant effects of stress-strain misalignment. Hence, other test cases with higher levels of unsteadiness will be the subject of the ongoing work.

References

[1] W. K. Chow and W. K. Mok, "CFD Fire simulations with four turbulence models and their combinations," *Journal of Fire Sciences*, vol. 17, no. 3, pp. 209–239, 1999.

[2] T. Hara and S. Kato, "Numerical simulation of thermal plumes in free space using the standard $k - \varepsilon$ model," *Fire Safety Journal*, vol. 39, no. 2, pp. 105–129, 2004.

[3] G. Laurent, B. Sapa, and F. Nmira, "MAGIC and Code_Saturne developments and simulations for mechanically ventilated compartment fires," *Fire Safety Journal*, pp. 1–13, 2013.

[4] V. Novozhilov, "Computational fluid dynamics modeling of compartment fires," *Progress in Energy and Combustion science*, vol. 27, no. 6, pp. 611–666, 2001.

[5] B. Sapa, *Contribution á l'extension d'un schéma incompressible pour les flammes à bas nombre de Froude - Pré-requis à la modélisation de l'incendie.* Ph.D thesis, L'UNIVERSITE DE POITIERS, France, 2011.

[6] K. V. Vanmaele and B. Merci, "Application of two buoyancy-modified $k-\varepsilon$ turbulence models to different types of buoyant plumes," *Fire Safety Journal*, vol. 41, no. 2, pp. 122–138, 2006.

[7] A. Revell, *Stress-strain Lag Eddy Viscosity Model for Mean Unsteady Turbulent Flows.* Ph.D thesis, The Univeristy of Manchester, UK, 2006.

[8] A. Revell, G. Iaccarino, and X. Wu, "Advanced RANS modeling of wingtip vortex flows," in *Proceedings of the 2006 Summer Program*, pp. 73–85, CTR/ University of Stanford, USA, 2006.

[9] A. Revell, S. Benhamadouche, T. Craft, and D. Laurence, "A stress-strain lag Eddy viscosity model for unsteady mean flow," *International Journal of Heat and Fluid Flow*, vol. 27, no. 5, pp. 821–830, 2006.

[10] A. Revell, T. Craft, and D. Laurence, "Turbulence Modelling of Strongly Detached Unsteady Flows : The Circular Cylinder," in *Advances in Hybrid RANS-LES Modelling* (H. Peng, S and W. Haase, eds.), ch. NNFM 97, pp. 279–288, Berlin, Germany: Springer-Verlag Berlin Heidelberg, 2008.

[11] V. Guimet and D. Laurence, "A linearised turbulent production in the $k - \varepsilon$ model for engineering applications," in *ETMM5*, (Mallorca, Spain), Elsevier, 2002.

[12] A. J. Revell, T. J. Craft, and D. R. Laurence, "Turbulence modelling of unsteady turbulent flows using the stress strain lag model," *Flow, Turbulence and Combustion*, vol. 86, pp. 129–151, 2011.

[13] W. P. Jones, *Models for Turbulent Flows with Variable Density and Combustion.* New York, USA: (W. Kollman, Ed) Hemisphere, 1980.

[14] K. N. C. Bray, "Turbulent transport in flames," *Proceedings: Mathematical and Physical Sciences*, vol. 451, no. 1941, pp. 231–256, 1995.

[15] R. W. Dibble, W. Kollman, M. Farshchi, and R. W. Schefer, "Second-order closure for turbulent non-premixed flames: scalar dissipation and heat release effects," *Symposium (International) on Combustion*, vol. 21, no. 1, pp. 1329–1340, 1988.

[16] B. E. Launder, G. J. Reece, and W. Rodi, "Progress in the development of a Reynolds-stress turbulence closure," *Journal of Fluid*, vol. 68, no. 3, pp. 537–566, 1975.

[17] C. G. Speziale, S. Sarkar, and T. G. Gatski, "Modelling the pressure-strain correlation of turbulence: an invariant dynamical systems approach," *Journal of Fluid Mechanics*, vol. 227, pp. 245–272, 1991.

[18] M. Assad, *Improved Fire Modelling.* Ph.D thesis, The University of Manchester, UK, unpublished work.

[19] T. J. Craft, B. E. Launder, and K. Suga, "Development and application of a cubic eddy-viscosity model of turbulence," *International Journal of Heat and Fluid Flow*, vol. 17, pp. 108–115, 1996.

[20] F. Menter, "Two-equation eddy-viscosity turbulence models for engineering applications," *AIAA Journal*, vol. 32, no. 8, pp. 269–289, 1994.

[21] F. Archambeau, N. Mechitoua, and M. Sakiz, "Code Saturne: A Finite Volume Code for Turbulent flows," *International Journal on Finite Volumes*, vol. 1, no. 1, 2004.

[22] B. Sapa, H. El-Rabii, L. Gay, N. Mechitoua, P. Plion, and H. Y. Wang, "URANS Approach for Buoyancy Dominated Turbulent Diffusion Flames," in *the 6th Mediterranean Combustion Symposium*, (Ajaccio, France, June 7-11), Combustion Institute and the International Centre for Heat and Mass Transfer, 2009.

[23] B. E. Launder and D. B. Spalding, "The numerical computation of turbulent flows," *Computer methods in applied mechanics and Engineering*, vol. 3, pp. 269–289, 1974.

[24] W. Chung and C. B. Devaud, "Buoyancy-corrected $k - \varepsilon$ models and large eddy simulation applied to a large axisymmetric helium plume," *International Journal For Numerical in Fluids*, vol. 58, no. 1, pp. 57–89, 2008.

[25] V. E. Sanderson, *Turbulence Modelling of Turbulent Buoyant Jets and Compartment Fires.* Ph.D thesis, Cranfield University, UK, 2001.

[26] B. A. Malin, M. R.; Younis, "Calculation of turbulent buoyant plumes with a reynolds stress and heat flux transport closure," *International Journal of Heat and Fluid Flow*, vol. 33, no. 10, pp. 2247–2264, 1990.

[27] K. William, J. George, R. L. Alpert, and F. Ramanini, "Turbulence measurement in an axisymetric buoyant plume," *International Journal of Heat and Mass Transfer*, vol. 20, pp. 1145–1154, 1977.

[28] A. Shabbir and W. George, "Experiments on a round turbulent buoyant plume," *Journal of Fluid Mechanics*, vol. 275, pp. 1–32, 1994.

AN EVOLUTION EQUATION FOR FLAME TURBULENCE INTERACTION IN PREMIXED TURBULENT COMBUSTION

U.Ahmed[1*], R.Prosser[1] and A.J.Revell[1]

Modelling & Simulation Centre, School of MACE, University of Manchester, M13 9PL, UK[1]
*umair.ahmed@manchester.ac.uk

Abstract

Flame turbulence interaction is one of the leading order terms in the scalar dissipation $\widetilde{\epsilon}_c$ transport equation [1] and is thus an important phenomenon in premixed turbulent combustion. Swaminathan and Grout [2] and Chakraborty and Swaminathan [3, 4] have shown that the effect of strain rate on the transport of $\widetilde{\epsilon}_c$ is dominated by the interaction between the fluctuating scalar gradients and the fluctuating strain rate (denoted here by $\overline{\rho}\widetilde{\Delta}_c = \overline{\rho\alpha\nabla c'' S''_{ij}\nabla c''}$); which represents the flame turbulence interaction phenomenon.

In order to obtain an accurate representation of the flame turbulence interaction, a new evolution equation for $\widetilde{\Delta}_c$ has been proposed by Ahmed *et al* [5]. This equation gives a detailed insight into the flame turbulence interaction phenomenon and provides a more flexible approach to model the important physics represented by $\widetilde{\Delta}_c$. An order of magnitude analysis similar to that proposed by Swaminathan and Bray [1] has been carried out on the evolution equation to determine the leading order terms. A priori analysis of the leading order terms has been undertaken via the DNS results of Dunstan *et al* [6]. It has been found that the behaviour of $\widetilde{\Delta}_c$ is determined by the competition between the source terms (pressure gradient and the reaction rate), diffusion processes, turbulent strain rate and the dilatation rate. Comparisons between the leading order model predictions and the DNS data set have been carried out and are presented in this paper. A new time scale for the flame turbulence interaction is proposed. The new time scale gives a measure of the characteristic time required by the flame gradient to change alignment with respect to the strain rate eigenvectors.

1 Introduction

Turbulent premixed flames are usually modelled in terms of temperature (or a reactive scalar mass fraction) defined as $c \equiv (T - T_R) / (T_P - T_R)$, where T is the local temperature and the subscripts, R and P denote the reactant and product mixtures respectively. A transport equation for the Favre averaged progress variable $\widetilde{c}$ requires closures for mean reaction rate $\overline{\omega}_c$ and the turbulent transport of $\widetilde{c}$. The mean reaction rate $\overline{\omega}_c$ is usually closed as [7]:

$$\overline{\omega}_c \simeq \frac{1}{2C_m - 1}\overline{\rho}\widetilde{\epsilon}_c, \tag{1}$$

where $\widetilde{\epsilon}_c$ is the scalar dissipation, $\overline{\rho}\widetilde{\epsilon}_c = \overline{\rho\alpha(\nabla c''\nabla c'')}$ (double primes denote the Favre fluctuations), α represents the molecular diffusivity of the progress variable and C_m is a model constant. Recently, a transport equa-

tion for $\widetilde{\epsilon}_c$ has been proposed [1]:

$$\overline{\rho}\frac{D\widetilde{\epsilon}_c}{Dt} = D_1 - D_2 + T_1 + T_2 + T_3 + T_4 \tag{2}$$

where the nomenclature of the RHS of 2 reflects the most common usage [1, 3, 8]. Each of the terms on the RHS of 2 represent a particular physical process; for example

$$T_3 = -2\overline{\rho\alpha}\frac{\partial\widetilde{c}}{\partial x_i}\underbrace{\left(\widetilde{\frac{\partial c''}{\partial x_j}\frac{\partial u''_i}{\partial x_j}}\right)}_{T_{31}} -2\overline{\rho\alpha}\underbrace{\left(\widetilde{\frac{\partial c''}{\partial x_i}S''_{ij}\frac{\partial c''}{\partial x_j}}\right)}_{T_{32}}$$

$$-2\overline{\rho\alpha}\underbrace{\left(\widetilde{\frac{\partial c''}{\partial x_i}\frac{\partial c''}{\partial x_j}}\right)\widetilde{S}_{ij}}_{T_{33}} \tag{3}$$

represents the combined effects of flame turbulence interaction.

An order of magnitude analysis under joint assumptions of high Reynolds (Re) and Damköhler (Da) numbers shows term T_{32} to be of leading order in 2 [1]; the behaviour of T_3 is thus dominated by the behaviour of T_{32} [2]. Here T_{32} is denoted by $-2\overline{\rho}\widetilde{\Delta}_c$, defined as:

$$\overline{\rho}\widetilde{\Delta}_c \equiv \overline{\rho\alpha\frac{\partial c''}{\partial x_i}S''_{ij}\frac{\partial c''}{\partial x_j}}, \tag{4}$$

where $S''_{ij} = 0.5\left(\partial u''_i/\partial x_j + \partial u''_j/\partial x_i\right)$.

In the case of statistically multidimensional flames, $\widetilde{\Delta}_c$ can be decomposed using the eigendecomposition and written as [8, 9]:

$$\overline{\rho}\widetilde{\Delta}_c = \overline{\rho\alpha\left|\nabla c''\right|^2\left(e_\alpha\cos^2\theta_\alpha + e_\beta\cos^2\theta_\beta + e_\gamma\cos^2\theta_\gamma\right)}, \tag{5}$$

where e_α, e_β and e_γ are the eigenvalues of the turbulent strain rate tensor S''_{ij}. The eigenvalues are ranked as $e_\alpha > e_\beta > e_\gamma$, with e_α being the most extensive principal strain rate. The angle between the scalar gradient and the eigenvector for e_α strain rate is denoted by θ_α. The source or sink behaviour of $-2\overline{\rho}\widetilde{\Delta}_c$ is dependent on the statistics of the alignment between the scalar gradient and the directions of the principal strain rates [10, 8]. It is well known that in case of the cold turbulence, the scalar gradient preferentially aligns with the most compressive principal strain rate [11, 12], thus giving a source contribution from $-2\overline{\rho}\widetilde{\Delta}_c$. In case of flows with intense heat release, it has been shown by Chakraborty and Swaminathan [3] and Swaminathan and Grout [2] that the scalar gradient preferentially aligns with the

most extensive principal strain rate. The variation between the alignment characteristics is due to the competition between dilatation rate and turbulent strain rate [2]. In the case of strong heat release, the dilatation usually occurring in the flame normal direction overcomes the turbulence effects thus causing the scalar gradient to align with the most extensive strain rate [10]. When the dilatation rate overcomes the turbulence strain rate, $-2\overline{\rho}\widetilde{\Delta}_c$ dissipates the scalar gradient.

The treatment of flame turbulence interaction presents a major difficulty in obtaining an accurate closure for the scalar dissipation $\widetilde{\epsilon}_c$ and thus the mean reaction rate $\overline{\dot{\omega}}_c$. An evolution equation for $\widetilde{\Delta}_c$ has recently been proposed by Ahmed *et al* [5], and is discussed in the next Section.

2 Flame turbulence interaction evolution equation

An evolution equation for $\widetilde{\Delta}_c$ can be used to represent the degree of misalignment between the scalar gradient and the strain rate eigenvectors. After much algebra the transport equation for $\widetilde{\Delta}_c$ can be obtained as (details of the derivation can be found in [13]) [5]:

$$\overline{\rho}\frac{D}{Dt}\left(\overline{\alpha\frac{\partial c''}{\partial x_i}S_{ij}\frac{\partial c''}{\partial x_j}}\right)=\overline{\rho}\frac{D\widetilde{\Delta}_c}{Dt}$$

$$=-\frac{\partial}{\partial x_n}\left(\overline{\rho\alpha\, u''\frac{\partial c''}{\partial x_i}S_{ij}''\frac{\partial c''}{\partial x_j}}\right)$$

$$\underbrace{+2\overline{\rho\alpha\alpha\frac{\partial c''}{\partial x_i}S_{ij}''\frac{\partial}{\partial x_j}\left(\frac{\partial}{\partial x_n}\left(\frac{\partial c''}{\partial x_n}\right)\right)}}_{D_{f1}}$$

$$\underbrace{+\overline{\alpha\frac{\partial c''}{\partial x_i}\frac{\partial c''}{\partial x_j}\frac{\partial}{\partial x_n}\left(\frac{\partial \tau_{in}''}{\partial x_j}\right)}}_{D_{f2}}$$

$$+F_1+F_2+F_3+F_4+F_5. \qquad (6)$$

D_{f1} and D_{f2} represent diffusion terms. F_1 represents the source terms due to pressure gradient and the reaction rate :

$$F_1=\overline{2\alpha\frac{\partial c''}{\partial x_i}S_{ij}''\frac{\partial \dot{\omega}_c''}{\partial x_j}}-\overline{\alpha\frac{\partial c''}{\partial x_i}\frac{\partial c''}{\partial x_j}\frac{\partial}{\partial x_i}\left(\frac{\partial P'}{\partial x_j}\right)}, \qquad (7)$$

F_2 represents the terms arising due to the scalar flux :

$$F_2=\underbrace{2\overline{\rho\alpha}\frac{\partial c''}{\partial x_i}S_{ij}''u_n''\frac{\partial}{\partial x_n}\left(\frac{\partial c''}{\partial x_j}\right)}_{F_{21}}$$

$$\underbrace{-2\overline{\rho\alpha}\frac{\partial c''}{\partial x_i}S_{ij}''u_n''\frac{\partial}{\partial x_n}\left(\frac{\partial \widetilde{c}}{\partial x_j}\right)}_{F_{22}}$$

$$\underbrace{+\overline{\rho\alpha}\frac{\partial c''}{\partial x_i}\frac{\partial c''}{\partial x_j}u_n''\frac{\partial}{\partial x_n}\left(\frac{\partial u_i''}{\partial x_j}\right)}_{F_{23}}\underbrace{-\overline{\rho\alpha}\frac{\partial c''}{\partial x_i}\frac{\partial c''}{\partial x_j}u_n''\frac{\partial}{\partial x_n}\left(\frac{\partial \widetilde{u}_i}{\partial x_j}\right)}_{F_{24}},$$

$$(8)$$

F_3 represents the dilatation terms:

$$F_3=\underbrace{2\overline{\rho\alpha}\frac{\partial c''}{\partial x_i}S_{ij}''\frac{\partial c''}{\partial x_j}\frac{\partial u_l''}{\partial x_l}}_{F_{31}}+\underbrace{2\overline{\rho\alpha}\frac{\partial \widetilde{u}_l}{\partial x_l}\widetilde{\Delta}_c}_{F_{32}}$$

$$\underbrace{+2\overline{\rho\alpha}\frac{\partial \widetilde{c}}{\partial x_j}\frac{\partial c''}{\partial x_i}S_{ij}''\frac{\partial u_l''}{\partial x_l}}_{F_{33}}\underbrace{-2\overline{\rho\alpha}\frac{\partial c''}{\partial x_j}\frac{\partial u_l''}{\partial x_l}\frac{\partial c''}{\partial x_i}S_{ij}''}_{F_{34}}$$

$$\underbrace{+\overline{\alpha\frac{\partial \rho}{\partial x_j}\frac{\partial p'}{\partial x_i}\frac{\partial c''}{\partial x_j}\frac{\partial c''}{\partial x_i}\frac{1}{\rho}}}_{F_{35}}\underbrace{-\overline{\alpha\frac{\partial \rho}{\partial x_j}\frac{\partial \tau_{in}''}{\partial x_n}\frac{\partial c''}{\partial x_i}\frac{\partial c''}{\partial x_j}\frac{1}{\rho}}}_{F_{36}}, \qquad (9)$$

F_4 represents turbulent straining terms :

$$F_4=\underbrace{-2\overline{\rho\alpha}\frac{\partial c''}{\partial x_i}S_{ij}''\frac{\partial c''}{\partial x_n}\frac{\partial u_n''}{\partial x_j}}_{F_{41}}\underbrace{-2\overline{\rho\alpha}\frac{\partial c''}{\partial x_i}S_{ij}''\frac{\partial c''}{\partial x_n}\frac{\partial \widetilde{u}_n}{\partial x_j}}_{F_{42}}$$

$$\underbrace{-2\overline{\rho\alpha}\frac{\partial \widetilde{c}}{\partial x_n}\frac{\partial c''}{\partial x_i}S_{ij}''\frac{\partial u_n''}{\partial x_j}}_{F_{43}}\underbrace{+2\overline{\rho\alpha}\frac{\partial c''}{\partial x_n}\frac{\partial u_n''}{\partial x_j}\frac{\partial c''}{\partial x_i}S_{ij}''}_{F_{44}}$$

$$\underbrace{-\overline{\rho\alpha}\frac{\partial c''}{\partial x_i}\frac{\partial c''}{\partial x_j}\frac{\partial u_n''}{\partial x_j}\frac{\partial u_i''}{\partial x_n}}_{F_{45}}\underbrace{-\overline{\rho\alpha}\frac{\partial c''}{\partial x_i}\frac{\partial c''}{\partial x_j}\frac{\partial u_n''}{\partial x_j}\frac{\partial \widetilde{u}_i}{\partial x_n}}_{F_{46}}$$

$$\underbrace{-\overline{\rho\alpha}\frac{\partial \widetilde{u}_n}{\partial x_j}\frac{\partial c''}{\partial x_i}\frac{\partial c''}{\partial x_j}\frac{\partial u_i''}{\partial x_n}}_{F_{47}}\underbrace{+\overline{\rho\alpha}\frac{\partial c''}{\partial x_i}\frac{\partial c''}{\partial x_j}\frac{\partial u_n''}{\partial x_j}\frac{\partial u_i''}{\partial x_n}}_{F_{48}}, \qquad (10)$$

and F_5 represents the dilatation due to scalar flux :

$$F_5=\overline{\alpha\frac{\partial c''}{\partial x_i}S_{ij}''\frac{\partial c''}{\partial x_j}\frac{\partial}{\partial x_n}\left(\rho u_n''\right)}. \qquad (11)$$

2.1 Leading order terms in $\widetilde{\Delta}_c$ evolution equation

Using an order of magnitude analysis under the joint assumptions of high *Re* and *Da*, 6 simplifies to [5]:

$$D_f+F_1+F_D+F_{TS}+F_5+F_{21}+F_{23}\simeq 0 \qquad (12)$$

where D_f represents leading order diffusion terms as:

$$D_f=\overline{-2\rho\alpha\alpha\frac{\partial}{\partial x_n}\left(\frac{\partial c''}{\partial x_j}\right)\frac{\partial}{\partial x_n}\left(\frac{\partial c''}{\partial x_i}S_{ij}''\right)}$$

$$\overline{-2\rho\alpha\alpha\frac{\partial}{\partial x_n}\left(\frac{\partial c''}{\partial x_i}\frac{\partial c''}{\partial x_j}\frac{\partial}{\partial x_n}S_{ij}''\right)}$$

$$\overline{-2\rho\alpha\alpha\frac{\partial}{\partial x_n}\left(\frac{\partial c''}{\partial x_j}S_{ij}''\frac{\partial}{\partial x_n}\left(\frac{\partial c''}{\partial x_i}\right)\right)}$$

$$\overline{+\alpha\frac{\partial c''}{\partial x_i}\frac{\partial c''}{\partial x_j}\frac{\partial}{\partial x_n}\left(\frac{\partial \tau_{in}''}{\partial x_j}\right)}, \qquad (13)$$

F_D represents the leading order dilatation terms:

$$F_D=F_{31}+F_{34}+F_{35}+F_{36}, \qquad (14)$$

and F_{TS} represents the leading order turbulent straining terms:

$$F_{TS} = F_{41} + F_{44} + F_{45} + F_{48}. \quad (15)$$

Recently, closures for these terms have been proposed by Ahmed *et al* [5], the performance of which is assessed here via comparisons with a Direct Numerical Simulation (DNS) data from a turbulent premixed V-flame with $Da > 1$ and $Ka < 1$. The details of the DNS are discussed in the next Section.

3   DNS data

The DNS data set produced by Dunstan *et al* [6] for a turbulent premixed V-flame has been used for model comparisons. In the V-flame configuration, a stationary, non-planar flame is produced which is oblique to the mean flow, and subject to mean shear, strong tangential convection by the mean flow and flow divergence [14]. This type of configuration is characterised by a developing flame in a statistically two dimensional mean flow field; the turbulence intensity along the leading edge of the flame brush decreases significantly while the individual flame elements are convected in the stream wise direction [14].

The V-flame in the DNS is representative of a lean, unit Lewis number flame with pre-heated reactants. The combustion kinetics are approximated by a single step reaction, as the physics of interest are well captured by single-step chemistry within the range of combustion regimes considered [6, 14]. Details on the solution algorithm used in the DNS can be found in [6, 14, 15]. The domain for the V-flame simulations is a cube of side $29.69\delta_L^0$. The domain is discretised by a $512 \times 512 \times 512$ node uniform grid, ensuring a resolution of about 10 grid points to resolve the laminar flame thickness δ_L^0. The flame is stabilised by a flame holder positioned at $3.49\delta_L^0$ from the inlet plane; this is achieved by fixing the mass fraction through a Gaussian weighting function and restricting velocities to their mean values (further details on the flame holder can be found in [6]). A schematic of the computational domain is given in 1.
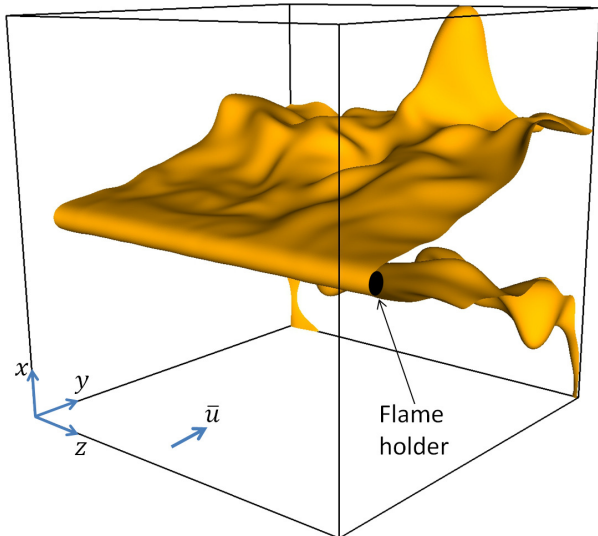
Figure 1: Computational domain for the V-flame DNS

During the post processing of the DNS, the data was averaged in time over 21 instantaneous realisations of the flow and space averaged in the spanwise periodic (z) direction. Spatial derivatives of fluctuating quantities required by the terms in 12 are calculated using the same numerical algorithm used in the DNS; 10th order central differencing for interior nodes, reducing to 4th order one-sided at the inflow and 2nd order one-sided on all outflows. The global thermochemical parameters used in the DNS are; planar, unstretched laminar flame speed $u_L^0 = 0.6034 \, m/s$; laminar flame thermal thickness $\delta_L^0 = (T_{ad} - T_0)/max|\nabla T| = 0.43 \, mm$ (where $T_{ad} = 2113.3 \, K$ is the adiabatic flame temperature and $T_0 = 600.0 \, K$ is the inlet reactant temperature); heat release parameter $\tau = (T_{ad} - T_0)/T_0 = 2.52$; characteristic laminar flame time is given by $\tau_f = \delta_L^0/u_L^0 = 0.71 \, ms$ and the laminar diffusive thickness $\delta_L = \alpha/u_L^0 = 0.1207 \, mm$. For the purpose of comparison with real air-fuel mixture flames, this is representative of a premixed methane-air flame with an equivalence ratio of $\phi \approx 0.6$ [6].

The values of the turbulent Reynolds number Re_{l_t}, Karlovitz number, Ka and Damköhler number, Da based on the laminar diffusive thickness and inlet flow conditions are summarised in 1, where u'_{in} is the rms velocity at the inlet, $\overline{u}_{in}$ is the mean inlet velocity in the $y-$direction, ν is the kinematic viscosity and l_t is the integral length scale.

u'_{in}/u_L^0	$\overline{u}_{in}/u_L^0$	$Re_{l_t,in}$	$l_{t,in}/\delta_L$	Ka_{in}	Da_{in}
2.0	16.6	37	12.82	0.79	6.41

Table 1: DNS database parameters at inlet plane

2 shows the contours of $\widetilde{c}$ $(0.1 - 0.9)$ in the V-flame DNS, where x^+ and y^+ represent the domain normalised by the thermal thickness of the the flame δ_L^0.
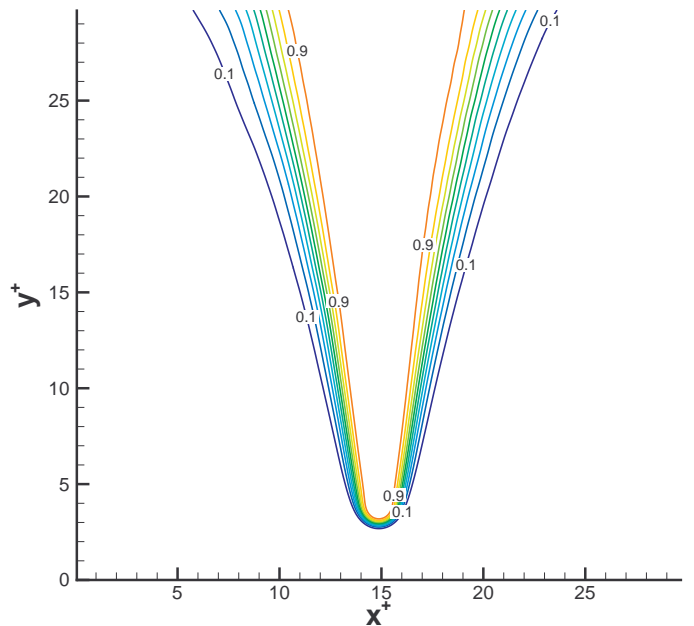
Figure 2: Favre averaged progress variable $\widetilde{c}$ contours $0.1 - 0.9$

4   Results and discussion

The present analysis is restricted to $y^+ > 20$, as beyond this location the flame has sufficient time to develop after ignition [6, 16]. Three sampling locations downstream of the flame holder at $y^+ \approx 23$, $y^+ \approx 25$ and $y^+ \approx 27$ are used. All the results have been normalised using ρ_R, u_L^0 and δ_L^0. As $\widetilde{c}$ varies monotonically from the flame centre-line ($x^+ = 15$), $\widetilde{c}$ is used instead to denote the location inside the flame brush in the results discussed below.
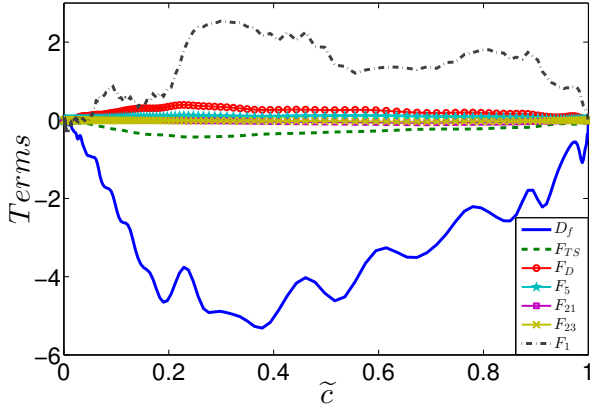
Figure 3: Normalised leading order terms at $y^+ \approx 27$

3 shows the profiles for the leading order terms in the $\widetilde{\Delta}_c$ evolution equation at $y^+ \approx 27$. The leading order terms show similar trends for $y^+ > 20$, hence trends for $y^+ \approx 27$ only are shown. It can be seen in 3 and 4 that there is a competition between the turbulent strain rate (F_{TS}) and the dilatation rate (F_D), which is in agreement with theories proposed in earlier studies [10, 2]. It can also be seen in 3 that there are additional mechanisms responsible for overall behaviour of $\widetilde{\Delta}_c$ evolution, as $\widetilde{\Delta}_c$ is controlled by a competition between the source terms (pressure gradient and reaction rate), diffusion process, turbulent strain rate and the dilatation rate [5].

Term F_{21} and F_{23} have been ignored in the current analysis, as they are small in comparison to the rest of the leading order terms; this can be seen in 3 and 4. Term F_5 shows similar trends to that of the dilatation rate as shown in 5, hence F_5 has been included in the dilatation rate terms for modelling [5].
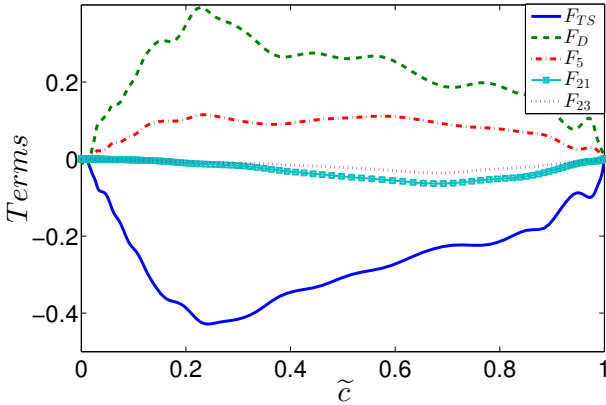
Figure 4: Normalised leading order terms without the diffusion and source terms at $y^+ \approx 27$

4.1 Model for F_{TS}

Turbulent straining represented by the term F_{TS} scales as $\backsim \widetilde{\epsilon}/\widetilde{k}$, thus leading to [5]:

$$F_{TS} \approx C_b \overline{\rho} \frac{\widetilde{\epsilon}}{\widetilde{k}} \widetilde{\Delta}_c, \qquad (16)$$

where C_b is a model constant. Following earlier modelling strategies used in the $\widetilde{\epsilon}_c$ transport equation [4], C_b is heuristically expressed as a function based on the local Karlovitz number Ka_L. The current functional form of
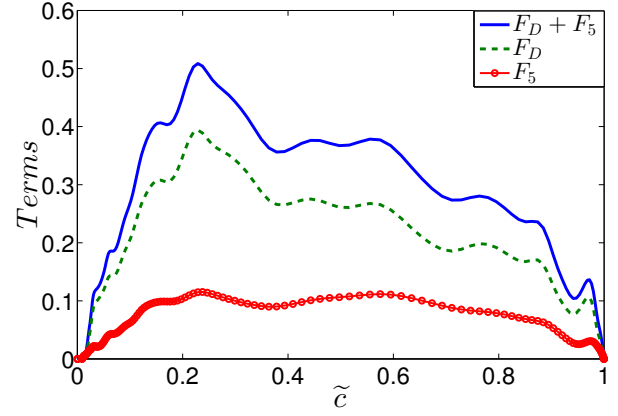
Figure 5: Comparisons of normalised F_5 and F_D in the DNS at $y^+ \approx 27$

C_b is based on the observations from the current DNS results [5]:

$$C_b = \frac{-6.4}{1 + \sqrt{Ka_L}}, \qquad (17)$$

where Ka_L is defined as:

$$Ka_L = \left(u'/u_L^0\right)^{3/2} \left(\delta_L/l_t\right)^{1/2}. \qquad (18)$$

It should be noted that the function for C_b is one of several possible empirical relations which lead to a physically realisable result. Note that $\widetilde{\Delta}_c$ has been introduced in 16 to include the effects of the interaction between scalar gradient and the strain rate eigenvectors. The model in 16 is only valid for high Damköhler number flames, and further tests need to be carried out to check the validity of the model for different combustion conditions. Comparisons of the model against the DNS data set are given in 6-8. The model predictions improve as the distance from the flame holder increases.
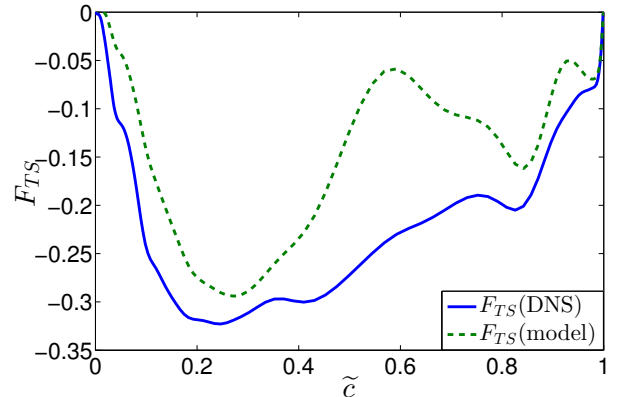
Figure 6: Comparisons of F_{TS} model predictions and the normalised DNS results at $y^+ \approx 23$

4.2 Model for $F_D + F_5$

Scaling the dilatation rate effects represented by terms $F_D + F_5$ as $\backsim \tau u_L^0/\delta_L$, leads to the model [5]:

$$F_D + F_5 \approx C_c \tau Da_L \overline{\rho} \widetilde{\Delta}_c \frac{u_L^0}{\delta_L} \qquad (19)$$
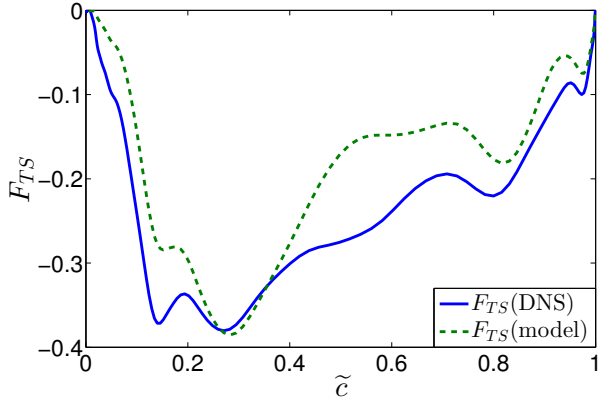
Figure 7: Comparisons of F_{TS} model predictions and the normalised DNS results at $y^+ \approx 25$
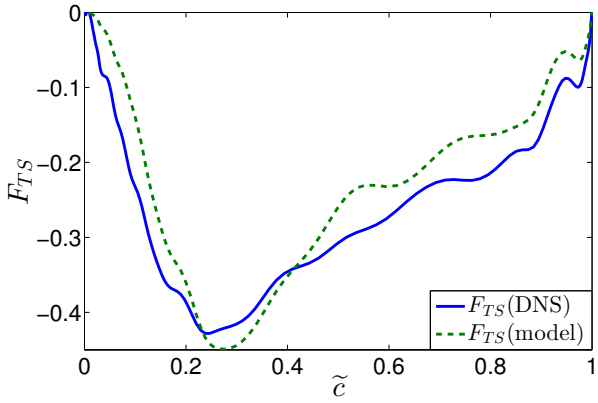
Figure 8: Comparisons of F_{TS} model predictions and the normalised DNS results at $y^+ \approx 27$

where Da_L represents the local Damköhler number and is defined as:

$$Da_L = \frac{\left(u_L^0/\delta_L\right)}{\left(\widetilde{\epsilon}/\widetilde{k}\right)}, \tag{20}$$

The constant C_c is defined as [5]:

$$C_c = \frac{0.01 + 0.1 Ka_L}{1 - Ka_L}. \tag{21}$$

$\widetilde{\Delta}_c$ has been introduced in 19 to include the effects of the interaction between scalar gradient and the strain rate eigenvectors. The expression for C_c in 21 is only valid for $Da > 1$ and $Ka < 1$ flames. A more robust model for C_c is needed to extend the range of applicable combustion regimes and forms part of the future work. The model proposed in 19 has an explicit dependence on the heat release parameter τ and the local Damköhler number Da_L, thus the model vanishes in the limiting case of cold flow turbulence. The model comparisons against the DNS data set are given in 9-11.

4.3 Model for diffusion D_f and F_1 source terms

It can be seen in 3 that term F_1 is dominantly a source and D_f is dominantly a sink for $\widetilde{\Delta}_c$ transport. The combined effects of diffusion and source terms $(D_f + F_1)$ can be modelled in flames with joint high Re and Da. Terms represented by $D_f + F_1$ scales as the flame normal strain $\sim \widetilde{\Delta}_c/\widetilde{\epsilon}_c$, thus leading to [5]:
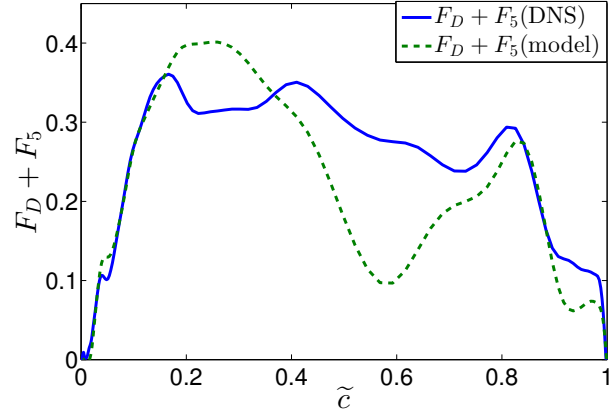
Figure 9: Comparisons of $(F_D + F_5)$ model predictions and the normalised DNS results at $y^+ \approx 23$
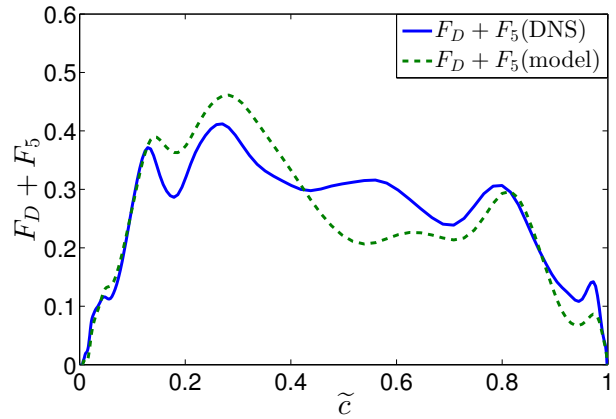
Figure 10: Comparisons of $(F_D + F_5)$ model predictions and the normalised DNS results at $y^+ \approx 25$

$$D_f + F_1 \approx -C_a \overline{\rho} \frac{\widetilde{\Delta}_c^2}{\widetilde{\epsilon}_c}. \tag{22}$$

The value of C_a in 22 is a matter of calibration and is dependent on the DNS data set used for model calibration. Here the value of C_a is 50, and the negative sign is used due to the over all sink nature of $D_f + F_1$ as shown in 12-14 . The ratio $\widetilde{\Delta}_c^2/\widetilde{\epsilon}_c$ in 22 represents the rate of change of flame turbulence interaction, $\widetilde{\Delta}_c^2/\widetilde{\epsilon}_c \approx d\widetilde{\Delta}_c/dt$; as the sum of terms D_f and F_1 has a dominant effect in $\widetilde{\Delta}_c$ transport thus controlling the overall behaviour of $\widetilde{\Delta}_c$ evolution.

In order to obtain a more accurate value of C_a, more DNS data sets are required and remain part of the future studies. The performance of the model against the DNS data set is given in 12-14.

5 Time scale for flame turbulence interaction

A time scale for flame turbulence alignment behaviour can be obtained by combining the models for the leading order terms as:

$$-C_a \frac{\widetilde{\Delta}_c^2}{\widetilde{\epsilon}_c} + C_b \widetilde{\Delta}_c \frac{\widetilde{\epsilon}}{\widetilde{k}} + C_c \widetilde{\Delta}_c \tau \frac{u_L^0}{\delta_L} \approx 0. \tag{23}$$

23 leads to :

$$\frac{\widetilde{\Delta}_c}{\widetilde{\epsilon}_c} \propto \frac{\widetilde{\epsilon}}{\widetilde{k}} + \tau \frac{u_L^0}{\delta_L} \tag{24}$$
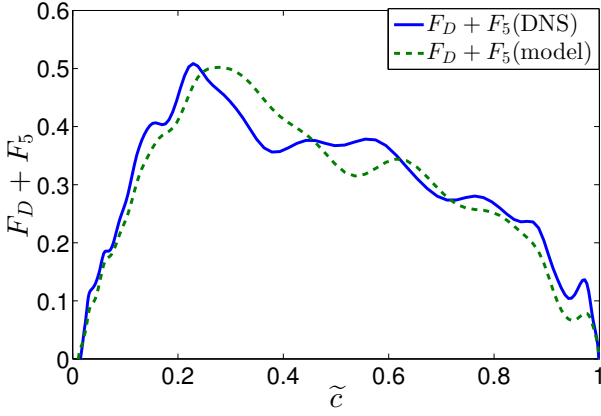
Figure 11: Comparisons of $(F_D + F_5)$ model predictions and the normalised DNS results at $y^+ \approx 27$
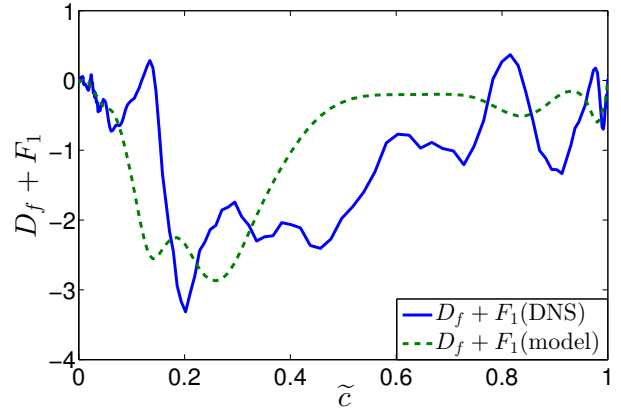
Figure 13: Comparisons of $(D_f + F_1)$ model predictions and the normalised DNS results at $y^+ \approx 25$
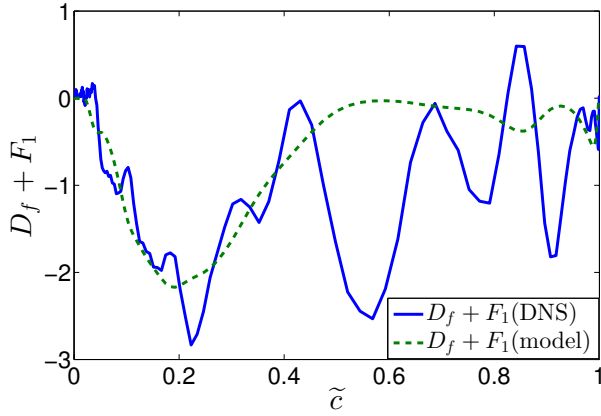
Figure 12: Comparisons of $(D_f + F_1)$ model predictions and the normalised DNS results at $y^+ \approx 23$
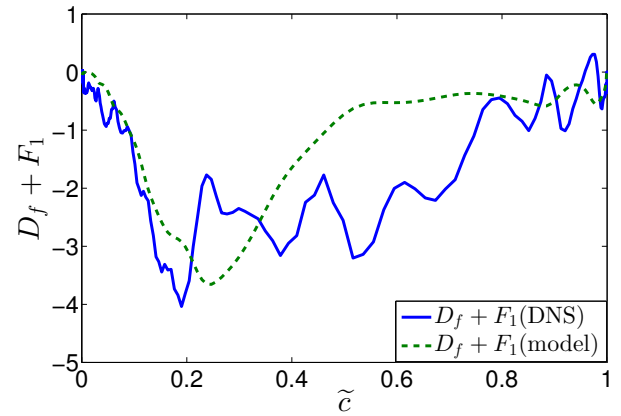
Figure 14: Comparisons of $(D_f + F_1)$ model predictions and the normalised DNS results at $y^+ \approx 27$

24 implies that the flame normal strain rate is directly related to the competition between the dilatation rate and the turbulent strain rate. Thus giving a time scale for the change in the alignment characteristics of the flame turbulence interaction. The time scale is represented as :

$$\tau_{FTI} = \frac{\widetilde{\epsilon}_c}{\widetilde{\Delta}_c}, \qquad (25)$$

where τ_{FTI} represents the time taken by the scalar/flame gradient to change alignment from the compressive strain rate e_γ to the extensive strain rate e_α and vice-versa.

6 Summary and Conclusion

Flame turbulence interaction is an important quantity in turbulent premixed combustion modelling. It has been shown in previous studies that the effect of strain rate on the transport of scalar dissipation is dominated by the interaction between the fluctuating scalar gradients and the fluctuating strain rate (here denoted by $\widetilde{\Delta}_c$). An accurate representation of the flame turbulence interaction can be obtained from the leading order terms in the evolution equation for $\widetilde{\Delta}_c$ [5]. A priori analysis of the leading order terms has been undertaken via the DNS results of Dunstan et al [6]. It has been found that the turbulent strain rate and the dilatation rate compete in $\widetilde{\Delta}_c$ evolution, which is in agreement with the theories proposed in earlier studies [10, 2]. It has also been found that the overall behaviour of the $\widetilde{\Delta}_c$ evolution equation is

determined by the competition between the source terms (pressure gradient and reaction rate), diffusion processes, turbulent strain rate and the dilatation rate.

A new time scale representing the time required by the flame gradient to change alignment with the strain rate eigenvectors has been proposed. Closures for the leading order terms have been compared against the DNS data set at different locations. The comparisons of modelled predictions and the DNS values are in good agreement for the combustion conditions considered here. More investigations of DNS data sets with different combustion conditions are needed to understand the behaviour of the leading order terms in $\widetilde{\Delta}_c$ transport equation, which would lead to more robust modelling strategies applicable to a wide range of combustion conditions. This forms part of the ongoing work.

Acknowledgements

References

[1] N. Swaminathan and K. N. C. Bray, "Effect of dilatation on scalar dissipation in turbulent premixed flames," *Combustion and Flame*, vol. 143, pp. 549–565, Dec. 2005.

[2] N. Swaminathan and R. W. Grout, "Interaction of

turbulence and scalar fields in premixed flames," *Physics of Fluids*, vol. 18, no. 4, p. 045102, 2006.

[3] N. Chakraborty and N. Swaminathan, "Influence of the Damkohler number on turbulence-scalar interaction in premixed flames. I. Physical insight," *Physics of Fluids*, vol. 19, no. 4, p. 045103, 2007.

[4] N. Chakraborty and N. Swaminathan, "Influence of the Damkohler number on turbulence-scalar interaction in premixed flames. II. Model development," *Physics of Fluids*, vol. 19, no. 4, p. 045104, 2007.

[5] U. Ahmed, R. Prosser, and A. J. Revell, "A Transport Equation for Flame Turbulence Interaction in Premixed Turbulent Combustion," in *Proc. European Combustion Meeting ECM2013*, (Lund, Sweden), 2013.

[6] T. D. Dunstan, N. Swaminathan, K. N. C. Bray, and R. S. Cant, "Geometrical Properties and Turbulent Flame Speed Measurements in Stationary Premixed V-flames Using Direct Numerical Simulation," *Flow, Turbulence and Combustion*, vol. 87, pp. 237–259, July 2010.

[7] K. N. C. Bray, "The interaction between turbulence and combustion," *Symposium (International) on Combustion*, vol. 17, no. 1, pp. 223–233, 1979.

[8] H. Kolla, J. W. Rogerson, N. Chakraborty, and N. Swaminathan, "Scalar dissipation rate modeling and its validation," *Combustion Science and Technology*, vol. 181, pp. 518–535, Feb. 2009.

[9] Y. Minamoto, N. Fukushima, M. Tanahashi, T. Miyauchi, T. D. Dunstan, and N. Swaminathan, "Effect of flow-geometry on turbulence-scalar interaction in premixed flames," *Physics of Fluids*, vol. 23, no. 12, p. 125107, 2011.

[10] N. Chakraborty, M. Champion, A. Mura, and N. Swaminathan, "Modelling methods, Scalar dissipation rate approach," in *Turbulent Premixed Flames* (N. Swaminathan and K. N. C. Bray, eds.), pp. 74–102, Cambridge University Press, 2011.

[11] W. T. Ashurst, a. R. Kerstein, R. M. Kerr, and C. H. Gibson, "Alignment of vorticity and scalar gradient with strain rate in simulated Navier Stokes turbulence," *Physics of Fluids*, vol. 30, no. 8, p. 2343, 1987.

[12] G. Batchelor, "The effect of homogeneous turbulence on material lines and surfaces," *Proceedings of the Royal Society of London. Series A, Mathematical and Physical Sciences*, vol. 213, no. 1114, pp. 349–366, 1952.

[13] U. Ahmed, "Flame turbulence interaction in premixed turbulent combustion." Ph.D. thesis, University Of Manchester, unpublished.

[14] T. D. Dunstan, N. Swaminathan, and K. N. C. Bray, "Influence of flame geometry on turbulent premixed flame propagation: a DNS investigation," *Journal of Fluid Mechanics*, vol. 709, pp. 191–222, Aug. 2012.

[15] K. Jenkins and R. Cant, "Direct numerical simulation of turbulent flame kernels," in *Recent Advances in DNS and LES: Proceedings of the Second AFOSR Conference, Rutgers - The State University of New Jersey, New Brunswick, USA* (D. Knight and L. Sakell, eds.), pp. 191–202, Kluwer, Dordrecht, 1999.

[16] T. D. Dunstan, Y. Minamoto, N. Chakraborty, and N. Swaminathan, "Scalar dissipation rate modelling for Large Eddy Simulation of turbulent premixed flames," *Proceedings of the Combustion Institute*, vol. 34, pp. 1193–1201, Jan. 2013.

Multiphase Turbulent Combustion

H.R.C.Rodrigues and D.J.E.M.Roekaerts

[1]*Department of Process and Energy, Section Fluid Mechanics, Delft University of Technology*

Abstract

Dilution of the oxidiser stream with products of combustion is an effective technique for reducing nitrogen oxide emissions of hydrocarbon combustion. To study this technology for the case of liquid fuels, a laboratory scale experimental setup was built with a fuel spray from a pressure atomizer issuing in hot diluted coflow. Phase Doppler anemometry results reveal that the coflow temperature determines the 'lifetime' of droplets and their penetration into the coflow. Coflow entrainment and momentum exchange between the continuous and dispersed phase determines the overall flow field. The turbulent shear stress in the near field is high, as a results of liquid jet break-up, and significant mixing takes place at the flame base leading to an increase of flame stability.

1 Characteristics of Turbulent Spray Flames

Many practical devices, such as industrial furnaces, diesel engines, and liquid propellant rockets, utilize combusting sprays as primary energy source. From a general point of view, spray flames are two-phase reacting flows with a continuous (gas) and a dispersed phase (droplets). A great deal can be learned by comparison with turbulent gas flames. Turbulent gas flames, for either laminar or turbulent flows, can be categorized in nonpremixed, premixed, or partially premixed depending on the degree of pre-mixing prior to combustion. At the global level, gas flames are formed from two reactants: a fuel and an oxidizer. When injected separately, these two are brought together through convection and diffusion, and after the mixing has occurred reaction can take place. These flames are labelled as nonpremixed flames. In a premixed system, an ignitable mixture is already present in the reactants stream. Diffusion is still needed to transport the heat and radical species from the reaction zone to the cold flammable mixture.

A big challenge in turbulent combustion is the strong coupling of fluid dynamics and chemical kinetics over wide ranges of spatial and temporal scales. The interaction of turbulence and chemistry produces temporal and spatial fluctuations in the mixing rates influencing the flame stability, relations among species concentrations and, ultimately, the formation of pollutants. The relative importance of the rates of chemical reaction and fluid dynamic mixing is characterized by the Damköhler number (Da) and is used to identify different regimes of premixed and nonpremixed turbulent combustion. Conceptually, Da $\rightarrow$ 0 represents a chemically frozen situation where the reaction time is excessively long relative to the characteristics flow time available for the reaction to proceed. The other extreme represents a situation of fast-chemistry where reaction is completed instantly.

In the case of the two-phase reacting flows considered here, the characteristics of the gas flames are strongly influenced by the release of reactant by evaporating droplets. A large number of of works dealing with single droplet combustion can be found in the literature since it was regarded as the building block of spray combustion [1, 2, 3, 4]. However, the relevance of single droplet burning to practical spray systems is limited. Droplets are known to evaporate and burn as a group, interacting with one another in practical environments [5, 6]. A mathematical treatment of the effect of collective drop vaporization and combustion has been developed by Chiu and has been the subject of several reviews [7, 8, 9]. However, the subject of group combustion theoretically is dealt with predominantly considering a spherically symmetric, hence one-dimensional, geometry leaving out important convective-diffusive nature of the full problem.

The creation of a spray of droplets most often starts with the injection of a liquid jet. Through the effects of flow instabilisties it disintegrates into ligaments and droplets. These initial liquid fragments, depending on the aerodynamic forces exerted can show additional breakup until the surface tension overcomes the aerodynamic forces. These two atomization stages of fragmentation are referred to as primary and secondary atomization [10, 11]. Since the total surface area of the liquid is extremely enlarged through the atomization process, also the effect of droplet evaporation becomes significant. Furthermore, the presence of relative velocities between droplets and the gas contributes to an enhanced droplet evaporation rate and gaseous mixing. Eventually, the reactive mixture may be or may not be well mixed by the time ignition takes place and the flame propagates through a partially premixed inhomogeneous mixture.

A first challenge arises in the primary atomization of the liquid jet. Different atomizers, often tailored to specific combustor geometries, produce different patterns and the resulting droplet distributions are mainly predicted empirically. The local mixture fraction and overall spray combustion processes are strongly dictated by the droplet dynamics and several regimes of turbulent gas flames can be present simultaneously. Moreover, the turbulence structure of the continuous phase is known to be modulated by the presence of the dispersed phase since the relative motion between the fluctuating velocities of the dispersed and continuous phase provides an additional mechanism for turbulent energy dissipation [12, 13]. This alteration may, in turn, depending on the local droplet mass loading manifest itself as significant changes in the Damköhler number.

2 Hot low oxygen environment as a clean combustion concept for liquid hydrocarbons

In recent years, there has been a strong drive to increase combustion efficiency while keeping the nitric oxide emissions level as low as possible. It is known that a reduction in the flame temperature leads to significant decrease of thermal nitric oxide formation rates. However, this gives rise to problems associated with flame stability. A theoretical analysis of a diffusion flame can show how to overcome the issue. Consider a system with two separate fuel (subscript 1) and oxidizer (subscript 2) streams in the gas state, it is possible to quantify the degree of mixing by a mixture fraction variable that represents the chemical elements locally available. In the limit of infinitely fast irreversible reactions ($Da \to \infty$) and assuming Lewis (Le) numbers equal to one, and constant specific heat, the temperature T as a function of the mixture fraction is given by [14]:

$$T = T_M(Z) + \frac{Q\, Y_{F,1}}{c_p}\, Z_{st}\, \frac{1-Z}{1-Z_{st}}, \qquad Z \leq Z_{st} \quad (1)$$

$$T = T_M(Z) + \frac{Q\, Y_{O_2}}{c_p}\, Z, \qquad Z > Z_{st} \quad (2)$$

$$Z_{st} = \left[1 + \frac{s Y_{F,1}}{Y_{O_2,2}}\right]^{-1} \quad (3)$$

where $T_M = Z T_1 + (1-Z)T_2$ is the temperature after non-reactive mixing, Q is the heat released per kg fuel and s is the oxidiser to fuel mass ratio for complete combustion.
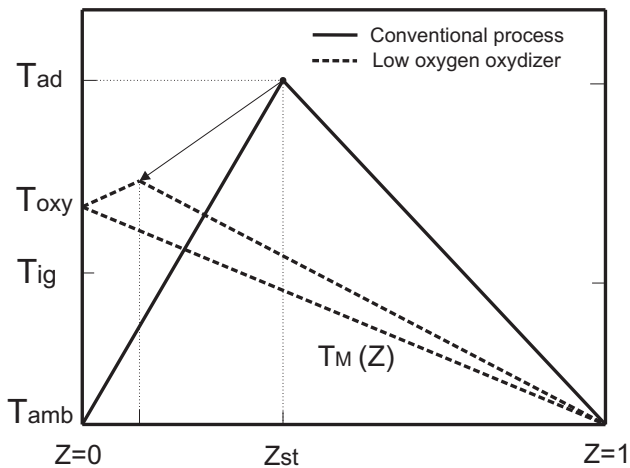
Figure 1: Illustration of the Burke-Schumann solution as a function of mixture fraction for conventional and depleted oxygen environment combustion process for the same fuel. T_{ig}, T_M and T_{oxy} refer to ignition, mixture and hot oxydizer temperature respectively

The linear profiles as function of mixture fraction are known as Burke-Schumann solutions and are shown in Figure 1. Conceptually, a decrease of the oxygen concentration (Y_{O_2}) in the oxidizer stream leads to a reduction in the peak flame temperature and, therefore, lowers thermal nitric oxide formation. However, the dilution causes a shift of the peak adiabatic temperature towards leaner mixtures. This can lead to practical problems associated with flame stability when the temperature of both streams is below the fuel auto-ignition temperature.

Thus, an increase of temperature of the oxidizer stream can be used to overcome this. The concept of low oxygen high temperature oxidiser stream has been applied with success in industrial scale furnaces [15, 16] but to widen its use to different fuels and application fields more investigations are needed on the local characteristics of the combustion process. Detailed studies are almost impossible in full scale systems but an interesting way out of this is the use of labscale experiments in so-called Jet-in-Hot-Coflow (JHC) burners. This is the approach we have used here extending earlier work on gas phase flameless combustion [19-22] to spray flameless combustion.

3 Experimental methods

3.1 Burner facility

Figure 2 shows a schematic of the burner facility at Delft University of Technology. The burner consists of a pressure-swirl atomizer that produces a spray of fine fuel droplets issuing in a coflow of hot combustion products. The purpose of laboratory-scale experiments in spray flames is to provide insight in the turbulent multiphase combustion phenomena without the presence of complex recirculating flow patterns. Ethanol is used as liquid fuel which has a relatively simple chemistry and well known refractive index.
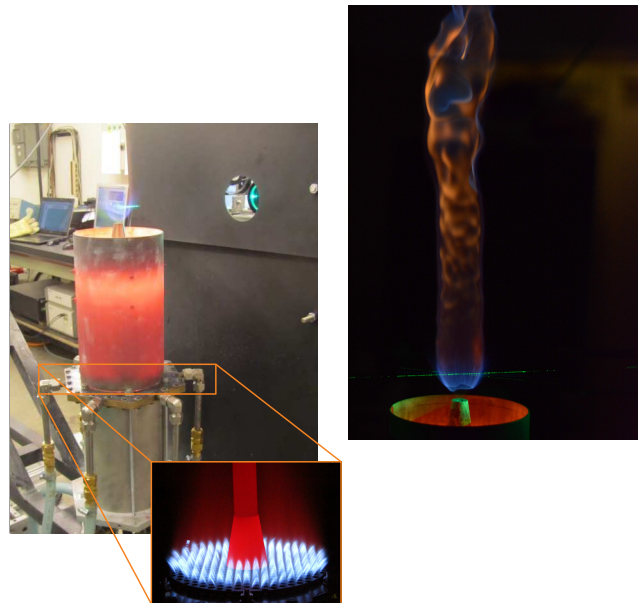
Figure 2: Burner facility and a photograph of a spray flame in hot diluted coflow (ISO speed: ISO4000, Exposure time:1/1000sec)

Hot coflow is produced by the secondary burner where air and Dutch Natural Gas (DNG) mix creating a matrix of lean flames. The heat transfer through the vertical round pipe establishes an enthalpy deficit in the hot combustion products to reach temperatures in the same range as that found in flameless combustion burners. Moreover, it shields the hot coflow from mixing with the surrounding air during this process. The air/DNG ratio in combination with the pipe length dictates the coflow temperature, oxygen concentration and, also, the turbulence levels. Since the energy needed to ignite the mixture is contained in the coflow, i.e. coflow temperature is higher than the ignition temperature, the spray flame is robust and no blow-off is achieved within the experimental capabilities.

3.2 Measurement techniques

Complementary single-point measurement techniques, Coherent Anti-Stokes Raman Scattering(CARS) and Laser Doppler Anemometry (LDA), were applied in the coflow to provide temperature and velocity statistics of the coflow. Refractory powder (Al_2O_3) was used to seed the coflow for the LDA measurements. Phase Doppler Anemometry (PDA) was applied in the spray region to obtain droplet velocity and diameter distribution at many locations. The results shown hereafter refer mainly to the PDA measurements. They can provide information on droplets dispersion relative to the mean and turbulent motion of the gas phase. How to obtain gas phase velocity from PDA measurements is explained in the next Section.

3.3 Measurement of the continuous phase velocity by Phase Doppler Anemometry

An LDA system measures the velocities of both 'seeding' particles that faithfully follow the gas phase but contributions to the signal are also made by droplets, and a a reliable method is needed to assign each velocity measurement to seeding particles or droplets. This is not trivial though and 'cross-talk' from the velocity distribution of the droplets to that of the seeding particles results in significant velocity bias in the continuous phase statistics [17, 18]. The advent of Phase Doppler Anemometry, additionally to the velocity statistics, brought forth the possibility to include the sizing information of spherical particles based on spatial frequency of a scattered interference pattern. However, due to their inherent aspherical shape, seeding particles cannot be sized unambiguously. Alternatively it is possible to extract information on the velocity characteristics of the continuous phase from small droplets provided they behave as tracers, i.e. follow the flow. Whether or not they do can be estimated from the Stokes number, defined in 4.

$$St = \frac{\text{Characteristic droplet relaxation time}}{\text{Characteristic gas phase time scale}} = \frac{\tau_d}{\tau_k} \quad (4)$$

were τ_d is given by:

$$\tau_d = \frac{\rho_d d_d^2}{18\mu_g} \quad (5)$$

The subscript "g" denotes the gas phase and "d" for droplet. Using Figure 4 it can be estimated whether small droplets relax quickly enough to the turbulent velocity fluctuations in the continuous phase to be considered as tracers. Knowledge of the coflow temperature is required to evaluate the Stokes number since the dynamic viscosity depends on temperature. Based on an estimate of the coflow temperature, in the analysis presented in the next Section droplets smaller than 6 μm are considered as flow tracers.

4 Reacting Spray Behavior and Morphology

The aim of this Section is to bring out the morphology of a reacting spray in hot diluted coflow and describe gas and droplets dynamics. The coflow velocity and oxygen volume fraction is 3.25 m/s and 6.5%, respectively. The liquid mass flow rate is 1.36 kg/hr corresponding to an injection pressure of approximately 12 bar. An image of the spray flame for the test case is shown in Figure 2. By visual inspection it is possible to divide the spray flame in three regions: liquid spray with no visible reaction, a faint blueish-reaction zone and faint rich-sooty region far downstream. Within the experimental setup capabilities, increase of the liquid mass flow rate does not lead to blow-off or changes in the flame appearance.
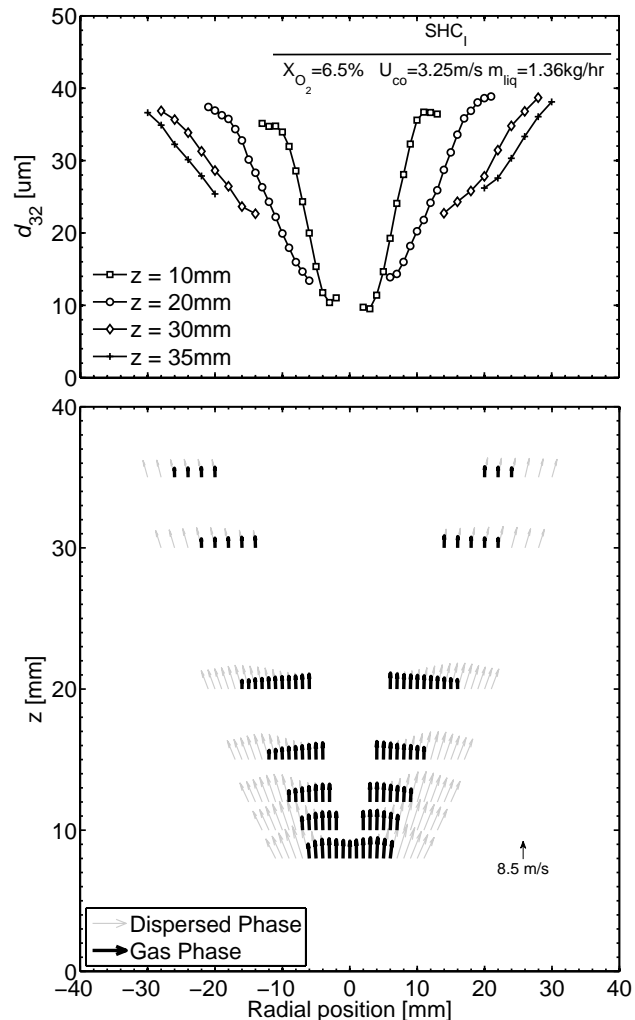
Figure 3: Sauter mean diameter (d_{32}) profiles and mean velocity field of gas and dispersed phase for a reacting spray in hot coflow for several axial stations

Mean velocity fields of the continuous and dispersed phase are presented in Figure 3 to show the global spray development. Sauter mean diameter profiles are presented to complement velocity field information. Gas phase mean properties were determined by assuming that droplets with diameter smaller than 6 μm are accurate gas flow tracers as mentioned earlier. Mean velocity of the droplets refer to the mean velocity average of the whole droplet ensemble. At axial position z = 10 mm, the Sauter mean diameter profiles show smaller droplets at the center region and increasingly large droplets radially. Droplets in the center region move upwards and at the spray edges spread radially outward into the hot coflow. With increasing axial distance from the atomizer droplets penetrate farther into the hot coflow and a substantial portion of the center is void of droplets. It is interesting to note that large droplets are present at radial distance larger than the maximal radial distance where visibly reaction occurs. The absence of droplets in the center region of the spray precludes an estimation of

the gas phase mean turbulent properties in that region.

5 Continuous phase mean and turbulent properties

Gas phase mean axial (U_z^g) and radial (U_r^g) velocity components are shown in Figure 4. By seeding the coflow, the absence of droplets in the center regions allows to determine gas phase velocity statistics along the center axis without incurring into velocity bias.
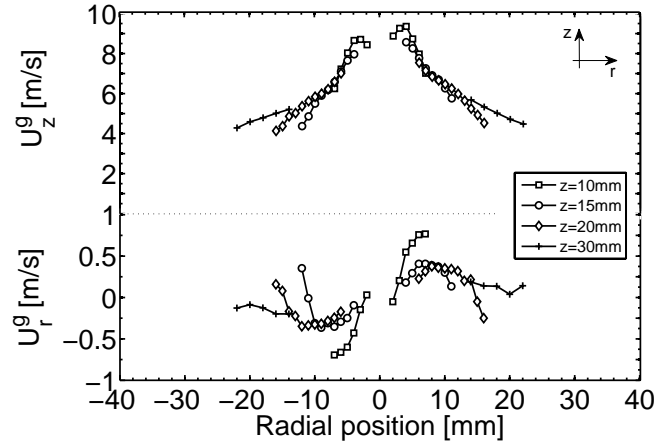
Figure 4: Gas phase mean axial (U_z^g) and radial (U_r^g) velocity profiles
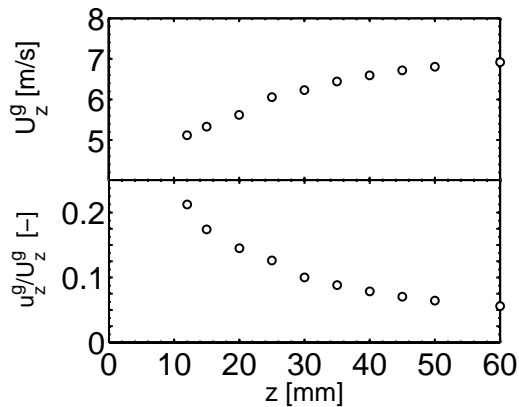
Figure 5: Gas phase axial mean velocity (U_z^g) and turbulent intensity (u_z^g/U_z^g) evolution along the spray axis

Gas mean axial velocity at z = 10 mm exhibits a local minimum near the center axis. The lower part of Figure 4 clearly shows that mean radial velocity variation in radial direction is quickly smeared out and the gas phase moves mainly vertically with large droplets moving radially outward and penetrating into the hot coflow. The negative mean radial values at large radial distance at the right side clearly indicate that the coflow is entrained into the spray. With increasing axial position, a gradual gas phase spread and increase of the mean axial velocity along the centreline is observed. Figure 5 shows the profiles of gas phase mean velocity and turbulence intensity along the centreline.

Radial profiles of the gas phase normal and shear Reynolds stress profiles are shown in Figure 6 for several axial stations. High normal and shear stresses are present in the dense region of the spray indicating that a strong mixing is present at the flame base. Near the
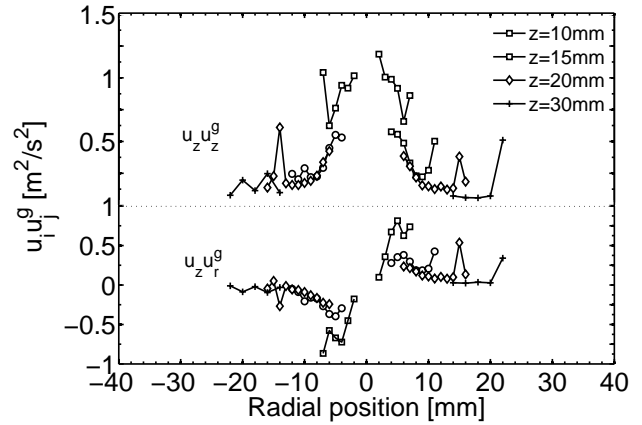
Figure 6: Gas phase normal ($u_z u_z^g$) and shear ($u_z u_r^g$) Reynolds stress profiles

nozzle the normal stress is clearly larger than the shear stress. Both normal and shear stress rapidly decrease with increasing distance from the nozzle.

6 Dispersed phase mean field

To evidence the peculiarities of the droplets behavior, droplet mean axial velocity of four size-classes were obtained at three axial positions. In Figure 7 mean gas phase velocities are presented along with the droplet velocities to give an overview of the velocity slip at the different axial stations .
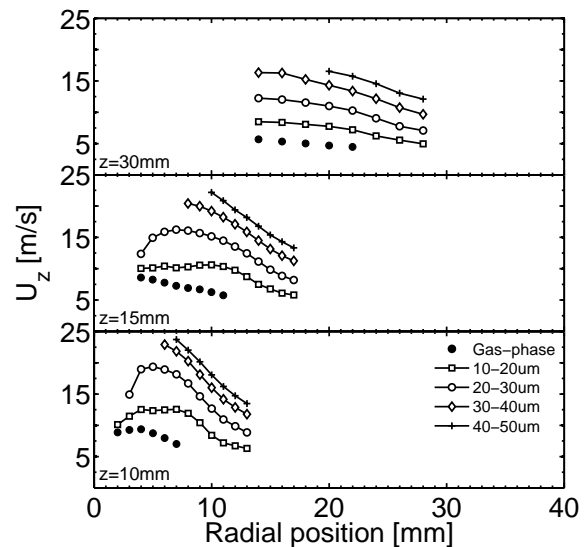
Figure 7: Mean gas axial velocity profiles and mean droplet axial velocity profiles per size class

Larger droplets have higher slip velocity than small droplets, with the difference being largest at z = 10 mm. At this axial position, the slip velocity between both gas and dispersed phase increases towards the spray outer edges. The droplets and ligaments originate from a liquid jet with a higher velocity than the adjacent coflow velocity. Large droplets have a longer relaxation time than those of small size, yielding high slip velocities. Farther downstream, up to z = 30mm, the slip velocity gradually decreases through the effects of drag on the dispersed phase.

Droplet density per size class is presented in Figure 8. Smaller droplets are mainly concentrated in the cen-
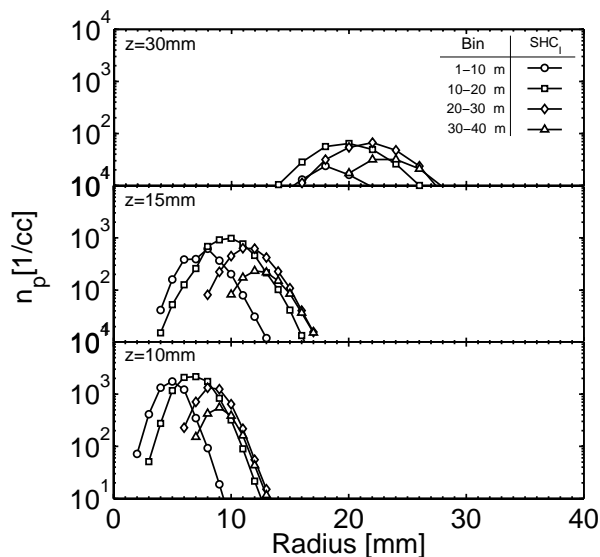
Figure 8: Radial profiles of droplet density (n_p) per droplet size class

ter region of the spray. With increasing axial position, droplet concentration decreases as a result of the rapid vaporization caused by the high coflow temperature.

7   Conclusions

The spray morphology of reacting sprays in hot diluted coflow with low oxygen concentration was measured by means of Phase Doppler Anemometry. Results show that, as a result of the liquid jet break-up, at the spray flame base small droplets are present in the spray center region moving with mean velocity in vertically upward direction (i.e. not spreading outwards). The overall droplet Sauter mean diameter becomes larger for radial positions further away from the center axis. Also the droplet mean radial velocity increases with radial distance form the center axis. It is observed that in the gas mean axial velocity profiles a velocity dip is present in the regions with low droplet concentration. Through momentum exchange, the liquid jet break-up leaves a fingerprint in the gas phase mean and turbulent properties at the spray flame base. The hot coflow imposes strong evaporative rates shortening significantly 'droplet lifetime' yielding a center region void of droplets and considerable amount of fuel vapour. The gas phase normal and shear stress are particularly high, promoting considerable mixing at the flame base.

At higher axial positions, the momentum exchange through drag and the droplet evaporation rates determine droplet penetration into the coflow. The coflow entrainment, along with the momentum exchange established in the regions with droplets, induces a gradual gas phase spreading and an increase of the mean axial velocity along the centerline.

The current experimental study has extended previous work on jet-in-hot-coflow for gaseous fuel[19-22] to liquid fuels. As in the previous work the entrainment of hot low oxygen coflow in the fuel jet is key phenomenon to understand the flame stabilisation. But in the case of a liquid fuel spray the release of gaseous fuel is distributed in space (as compared to injected through the nozzle in the case of a gaseous fuel). The release of vapour depends on droplet slip velocity and droplet size. The PDA measurements have provided the droplet joint velocity-diameter statistics, and provides an essential database for model

validation studies for jet-in-hot-coflow flames, in addition to the databases listed in Ref. [23]. Nevertheless, issues such as stabilization cannot be fully understood from only single-point measurements. Information on spatial gradients or more generally, spatial structures, is also needed. Aspects of minor species formation in the reaction zones and the effects of air entrainment in the stabilization mechanics of these flames can be provided by Two-color Particle Image Velocimetry (PIV) and hydroxyl Planar Laser-Induced Fluorescence (OH PLIF). Furthermore, the dense spray region close to the atomizer is not accessible for the standard laser diagnostic techniques. But in that region not only atomization occurs but also strong heat and mass transfer between the liquid and gaseous phases, especially in the case of a hot coflow. Therefore to have detailed boundary conditions at the entrance of the dilute spray region, also a measurement of fuel vapour concentration close to the burner would be needed. This information could be obtained via measurements or computations but further development of techniques is needed in both cases.

8   Acknowledgements

References

[1] A. Williams, "Combustion of droplets of liquid fuels: A review," *Combustion and Flame*, vol. 21, no. 1, pp. 1 – 31, 1973.

[2] J. Wu and G. M. Faeth, "Sphere wakes in still surroundings at intermediate reynolds numbers," *AIAA Journal*, vol. 31, pp. 1448–1455, 1993.

[3] J. Wu and G. M. Faeth, "Sphere wakes at moderate reynolds numbers in a turbulent environment," *Aiaa Journal*, vol. 32, pp. 535–541, 1994.

[4] G. M. Faeth and R. S. Lazar, "Fuel droplet burning rates in a combustion gas environment," *AIAA Journal*, vol. 9, pp. 2165–2171, Nov. 1971.

[5] J. Tsai and A. M. Sterling, "The combustion of linear droplet arrays," *Symposium (International) on Combustion*, vol. 23, no. 1, pp. 1405 – 1411, 1991. Twenty-Third Symposium (International) on Combustion.

[6] K. Miyasaka and C. K. Law, "Combustion of strongly-interacting linear droplet arrays," *Symposium (International) on Combustion*, vol. 18, no. 1, pp. 283 – 292, 1981. Eighteenth Symposium (International) on Combustion.

[7] H.H. Chiu *et al.*, "Internal group combustion of liquid droplets," *Nineteenth Symposium (International) on Combustion*, vol. Vol. 19, pp. Pag. 971–980, 1982.

[8] H.H. Chiu *et al.*, "Group combustion of liquid droplets," *Combustion Science and Technology*, vol. Vol. 17, pp. Pag. 127–142, 1977.

[9] S. Lee, "Group vaporization of liquid fuel sprays," *Journal of Mechanical Science and Technology*, vol. 4, pp. 62–70, 1990. 10.1007/BF02953392.

[10] P. Marmottant and E. Villermaux, "On spray formation," *Journal of Fluid Mechanics*, vol. 498, pp. 73–111, 2004.

[11] E. Villermaux, "Fragmentation," *Annual review of Fluid Mechanics*, vol. 39, pp. 419–446, 2007.

[12] A. Wood, W. Hwang, and J. Eaton, "Preferential concentration of particles in homogeneous and isotropic turbulence," *International Journal of Multiphase Flow*, vol. 31, no. 10-11, pp. 1220 – 1230, 2005.

[13] C. Poelma and G. Ooms, "Particle-Turbulence Interaction in a Homogeneous, Isotropic Turbulent Suspension," *Applied Mechanics Reviews*, vol. 59, no. 2, pp. 78–90, 2006.

[14] N. Peters, *Turbulent Combustion.* Cambrige University Press, 2000.

[15] J.A. Wünning and J.G. Wünning, "Flameless oxidation to reduce thermal NOx formation," *Progress in Energy and Combustion Science*, vol. Vol. 23, pp. Pag. 81–94, 1997.

[16] R. Weber *et al.*, "On the (MILD) combustion of gaseous, liquid and solid fuels in high temperature preheated air," *Proceedings of the Combustion Institute Combustion and Flame*, vol. Vol. 30, pp. Pag. 2623–2629, 2005.

[17] Y. Hardalupas and A. Taylor, "The identification of LDA seeding particles by the phase-doppler technique," *Experiments in Fluids*, vol. 6, no. 2, pp. 137–140, 2004.

[18] P. T. H. Saffman, M. Buchhave, "Simultaneous measurement of size, concentration and velocity of spherical particles by a laser doppler method.," in *2nd Intl. Symposium on Applications of Laser Anemometry to Fluid Mechanics*, 1984. Paper 8.1.

[19] E. Oldenhof, M. Tummers, E. van Veen, and D. Roekaerts, "Ignition kernel formation and lift-off behaviour of jet-in-hot-coflow flames," *Combustion and Flame*, vol. 157, pp. Pag. 1037–1234, 2010.

[20] E. Oldenhof, M. Tummers, E. van Veen, and D. Roekaerts, "Role of entrainment in the stabilisation of jet-in-hot-coflow flames," *Combustion and Flame*, vol. 158, no. 8, pp. 1553 – 1563, 2011.

[21] E. Oldenhof, M. J. Tummers, E. H. van Veen, and D. J. Roekaerts, "Transient response of the delft jet-in-hot coflow flames," *Combustion and Flame*, vol. 159, no. 2, pp. 697 – 706, 2012.

[22] E. Oldenhof, M. J. Tummers, E. H. van Veen, and D. J. Roekaerts, "Conditional flow field statistics of jet-in-hot-coflow flames," *Combustion and Flame*, vol. 160, no. 8, pp. 1428 – 1440, 2013.

[23] P. Jenny, D. Roekaerts, and N. Beishuizen, "Modeling of turbulent dilute spray combustion," *Progress in Energy and Combustion Science*, vol. 38, no. 6, pp. 846–887, 2012.

Large-Eddy Simulation of Diluted Turbulent Spray Combustion Based on FGM Methodology

A. Sadiki[1], M. Chrigui[1,2], F. Sacomeno[1], J. Janicka[1] and A. R. Masri[3]

[1] *Institute for Energy and Power plant Technology, Department of Mechanical Engineering,*
TU Darmstadt, Petersenstr.30, 64287 Darmstadt, Germany

[2] *Engineering School, Department of Mechanical Engineering, the University of Gabes, Tunisia*

[3] *School of Aerospace, Mechanical and Mechatronic Engineering,*
The University of Sydney, NSW 2006, Australia

1 Introduction

Today, almost every industry that applies advanced design engineering uses CFD to predict and optimize flow processes. To achieve this task, with respect to combustion for instance, a design tool that enables to directly take into account unsteady effects inherent to combustion systems is highly demanded [1-16]. Dealing with devices, such as automotive engines, gas turbine combustors, the fuel is supplied as a liquid with varying physical and chemical properties to form a combustible mixture of fuel vapor and air. These time- and space varying fuel properties (in the vapor and liquid phase) affect substantially the vaporization and kinetics-related processes, like ignition, flame propagation/stability and pollutants level. An accurate modeling of these phenomena requires taking into account turbulence, heat transfer, fuel spray evaporation and detailed chemistry effects. In this contribution, the capability of Large-Eddy Simulation (LES), known for its proven predictability of intrinsically unsteady phenomena in single phase combustion systems [1, 2, 14, 22], is evaluated in analyzing combustion processes of liquid spray jets.

Comprehensive reviews of LES combustion models in reacting single phase flows are provided in [1, 2, 22]. Extensive fundamental and applied researches were especially dedicated to address questions that govern the interacting phenomena in reactive multiphase flows. Recent reviews are reported in [24-27]. With respect to chemistry, reduction techniques are mainly favored. Thereby considerable efforts are being accomplished in developing the so-called flamelet based tabulated chemistry along with the Flamelet Generated Manifold (FGM) (see e.g. [13, 20]) or the Flamelet Prolongated ILDM (FPI) [21]. Nevertheless, applications of FGM based combustion modelling to the description of spray combustion coupled to LES are rare. For a recent RANS based contribution, please refer to [29]. Only recently Chrigui et al. [24, 25, 27] published their first achievements using LES and FGM to investigate spray jet flames.

The present paper aims at demonstrating LES capability to numerically investigate turbulent ethanol spray combustion. To describe the flow, mixing and combustion properties, an Eulerian-Lagrangian approach is adopted. Following [24-27] the methodology includes a two-way coupling of the interacting two phases in presence, while the carrier phase turbulence is captured by the LES and the partially premixed combustion by the FGM approach. The droplet evaporation is described by a non-equilibrium vaporization model.

The paper is structured as follows. First the droplet Lagrangian tracking is introduced, followed by an outline of the non-equilibrium evaporation model (Section 2). Then the modeling approach of LES completed by the FGM generation is highlighted in Section 3. In Section 4 the experimental configuration and the computational set up including the boundary conditions for both the carrier and the disperse phases are presented. Analysis, discus-sion and comparisons of the numerical results with the experimental data are provided in Section 5 while conclusions are summarized in Section 6.

2 Disperse phase Lagrangian description

According to the Lagrangian approach, the equations of the droplet position, velocity and temperature along the trajectory of each computational droplet in the carrier flow field are solved. Since the ratio between the specific mass of liquid fuel and that of the gas phase mixture has a value around 103, we follow Chrigui et al. [24-25] and consider only the drag, gravitation and buoyancy forces to act on the droplet.

To quantify the instantaneous fluid velocity and its effect on the droplet distribution within the LES framework, the SGS values of the fluid parcel velocity at the droplet location should be modeled. As it is known from recent studies by Pozorski et al. [4] the impact of SGS dispersion can vary depending on the particle inertia parameter. In this work the SGS dispersion of droplet is not accounted for. It is generally argued that the long-time droplet dispersion is governed by the resolved, larger-scale fluid eddies. We thus simply rely on the fact that at least 80% of the instantaneous carrier phase turbulence level is captured by the resolved scales.

Assuming a uniform droplet temperature as dragged droplets have diameters in the range of 30μm, the Uniform Temperature (UT) model by Abramzon et al. [10] in its non-equilibrium extension [11] is applied to describe the droplet evaporation process (see also [23]). Note that all the assumptions of this model are valid in the investigated configuration. In particular, break-up and coalescence are neglected to ensure that the evolution of the droplet diameter is only due to the evaporation processes.
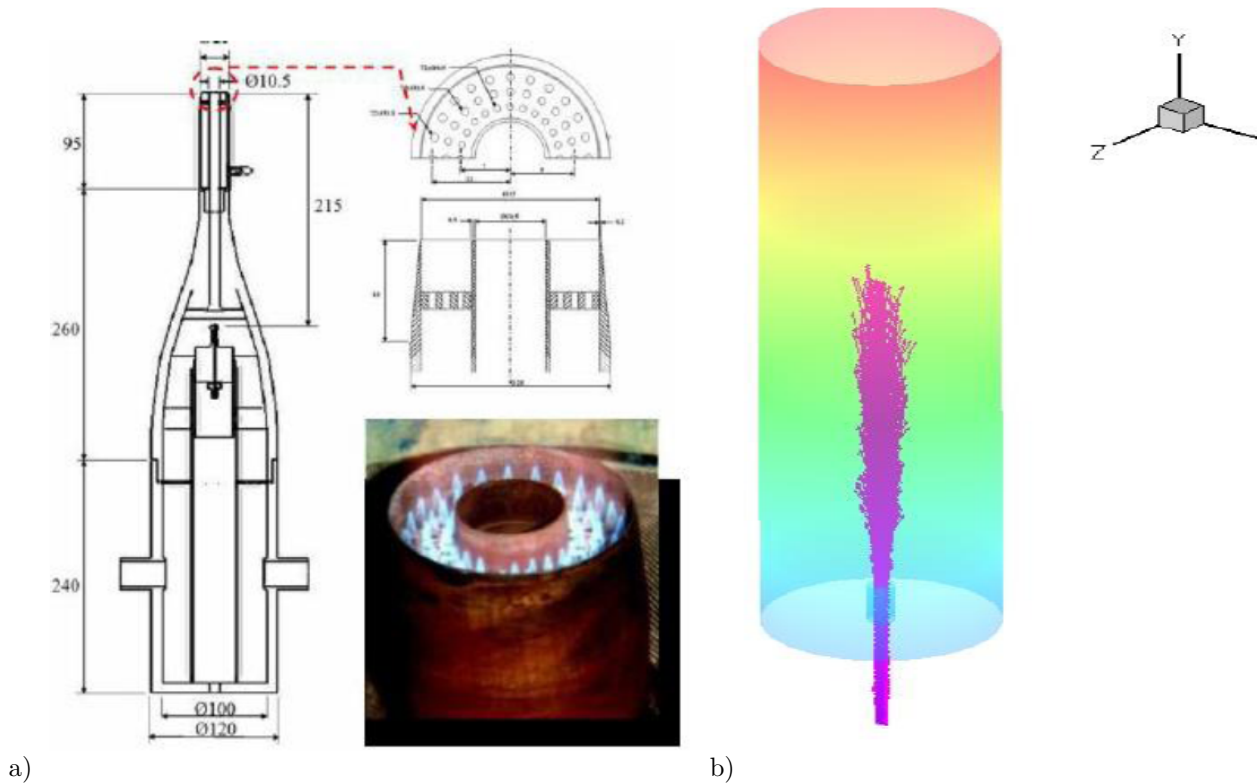
Figure 1: a) Schematic of the spray [24,25] burner set up; b) Computational domain [27]

3 LES description

In the line of the FGM approach, the filtered transport equations for control variables, namely the mixture fraction and one reaction progress variable (RPV), are solved together with the filtered transport equations for mass and momentum of the Newtonian fluid under investigation in a variable-density Low Mach number formulation.

These equations govern the evolution of the large, energy-carrying, scales of flow and scalar field. The effect of the small scales appears through the SGS stress tensor and the SGS scalar flux vector, respectively. The SGS stress tensor is modeled by a Smagorinsky model with a dynamic procedure according to Germano et al. [7]. In order to stabilize the model, the modification proposed by Sagaut [8] is applied. In addition a clipping approach will reset negative Germano coefficients to zero to avoid destabilizing values of the model coefficient. Though wall-adaptive SGS models have been proposed recently (see in [8]), no special walltreatment is included in the SGS model following Wegner et al. [9] who rely on the ability of the dynamic procedure to capture the correct asymptotic behavior of the turbulent flow when approaching the wall. Note that advanced SGS models have been proposed in the literature with the desirable property that they produce zero eddy-viscosity near solid-boundaries (see in [28]). To represent the SGS scalar flux in the mixture fraction and in the RPV equations a linear eddy diffusivity model is adopted with a constant turbulent Schmidt number of 0.7.

Source terms that characterize the direct interaction of mass, momentum, and mixture fraction between the droplets and the carrier gas are included featuring together with the large scale dispersion a two-way coupling between the phases in presence. For details, please refer to [24-27].

Concentrating on the RPV equation the classical filtered chemical reaction rate and additional terms that

Table 1: Flow boundary conditions applied

Ethanol Combustion	Flame test case EtF3	Flame test case EtF6
$\dot{m}_l[g/min]$	45	45
$U_{jet}[m/s]$	24	36
$\dot{m}_{air}[g/min]$	150	225
$Re_{jet}[-]$	19678	28076

may emerge to explicitly account for the effect of evaporation on combustion [5, 6] have to be modeled. Assuming that all droplets have evaporated before combustion, only the classical contribution needs further modeling within the FGM approach. Note that the RPV is defined by means of the mass fraction of CO_2 , H_2O and H_2 , respectively.

Using the two parameters, namely the mixture fraction and the RPV, a two-dimensional manifold is then generated by means of the CHEM1D code [12] by simply simulating a set of 1D diffusion flamelets with increasing scalar dissipation rate, and thereafter switching to unsteady flamelets when reaching the critical scalar dissipation rate (see in [20, 21, 24-27]). The ethanol chemistry is modeled by means of a detailed chemical reaction mechanism as developed and validated by Marinov [3]. It consists of 56 species and 351 reactions.

The filtered combustion variables required in the LES are then retrieved by integrating over the joint PDF of the mixture fraction and the defined RPV. Since the mixture fraction is no more a conservative quantity, it may influence the PDF distributions. Gutheil et al. [15] showed from a comparison of Monte-Carlo PDF with

standard beta-PDF that a beta-function describes the actual shape of the PDF differently. Nevertheless a presumed beta-PDF distribution is chosen here as crude approximation. This implies the mixture fraction depends on its first and second moments. As a firstorder approach, the PDF of the RPV is approximated by a delta-function, allowing the combustion variables to be function of the RPV mean values only. This assumption implies that the fluctuations of the RPV are sufficiently resolved or they could be omitted [24]. This is realistic for spray flames under study, since they tend to exhibit diffusion flame behavior in which the RPV fluctuations are not large compared to premixed cases. While generating the FGM table, the effect of droplet evaporation along with the interaction between evaporating droplets and combustion is not directly included. To do this, at least the vaporized mass quantity has to be included as parameter. This work is still in progress.

Because the proper contribution of the evaporation source term in the equation of the RPV has been neglected as complete evaporation has been assumed before combustion, the mixture fraction variance is obtained simply by adopting the algebraic gradient formulation in [14]. Thereby the model coefficient is set to 0.15.

4 Investigated configurations and numerical set up

The configuration used to study the ethanol spray combustion represents the setup experimentally investigated by Masri and Gounder [17] displayed in Figure 1a. Various operating conditions have been considered including effect of mass loading and fuel as well as the impact of Reynolds numbers on the spray combustion.
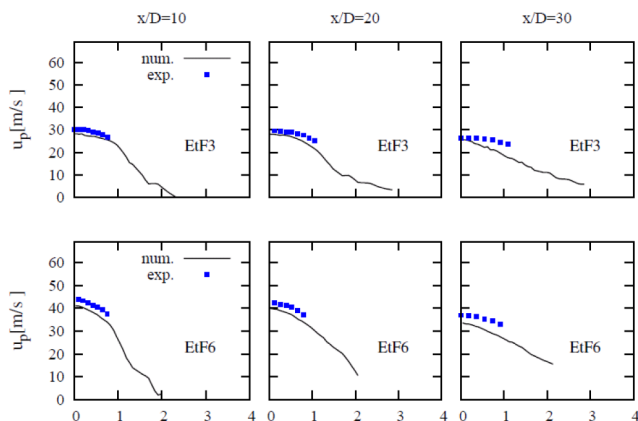
Figure 2: Radial profiles of the droplet mean axial velocity at different distances from the nozzle exit plane. The x-axis represents r/D

Using LES, Chrigui et al. [24-25] recently reported simulation results of some of these configurations. Especially the cases EtF3 and EtF8 have been investigated in [26, 27]. In this contribution the cases EtF6 is compared to the reference case EtF3 in terms of mass loading impact on the combustion properties. The spray is initialized 215 mm upstream of the nozzle exit plane and exhibits a poly-disperse behavior after traveling a pre-vaporization zone in which small classes evaporate before reaching the exit of the nozzle The resulting ethanol flames feature a partially premixed character. A detailed description of the experimental setup and measurement techniques used for the generation of the
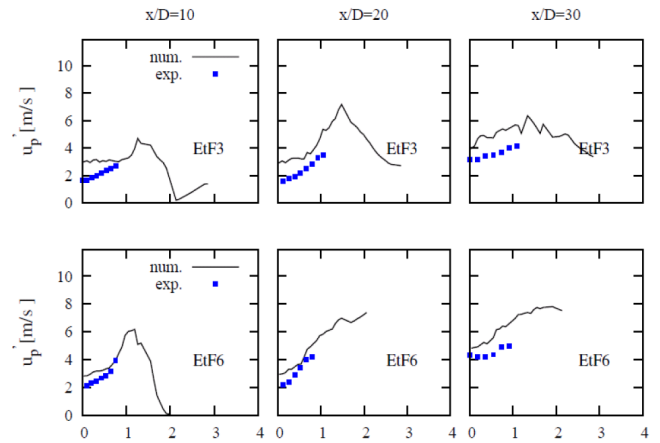
Figure 3: Radial profiles of the droplet axial velocity fluctuation at different distances from the nozzle exit plane. The x-axis represents r/D

comprehensive experimental data is provided by Masri and Gounder [17] (see also [24-27]).

Boundary conditions
Table 1 summarizes all the boundary conditions for the carrier phase. A decreasing mass loading of 30% to 15% could be calculated in the inner jet. The velocity components of the carrier phase are given as block profile at the inlets and the Reynolds numbers from Table 2 attest a highly turbulent two phase flow. As the carrier phase travels a distance 20D to reach the nozzle exit plane, the flow develops turbulent structures, even with block velocity profiles.

Following [24-27] the configuration under study is numerically represented by a computational domain consisting of 17 blocks that count 1.1×10^6 control volumes (cv), Figure 1b. Within one coupling time step the number of parcels injected is 2500 while the number of time steps achieved between both phases, that represent the fluid data and/or source term transfer, exceeds 320 000 couplings. The averaging of the spray flow properties is thus performed over more than 750×10^6 parcels. The disperse phase properties are statistically independent and not conditioned on the number of parcels tracked or coupling time steps. The TVD (total-variation-diminishing) boundary treatment is applied for the ve-
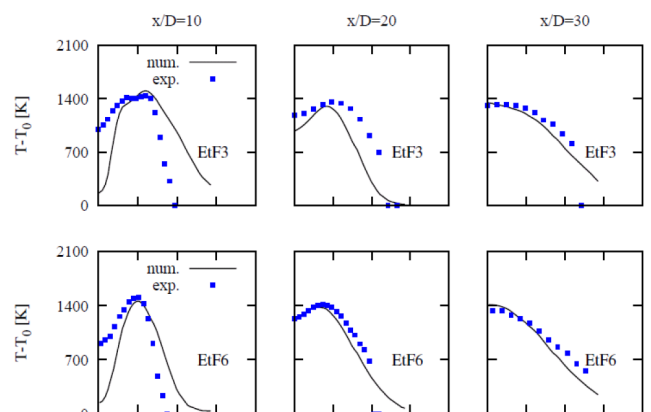
Figure 4: Radial profiles of the excess temperature at different distances from the nozzle exit plane. The x-axis represents r/D

locity exit boundary with a condition with 6 m/s. For the RPV the boundary condition is set to zero in the entire domain except at the pilot flame inlet, where it is set to the maximum absolute value that equals 0.0101. Note that the total number of the numerical tracked droplets exceeded 1 million parcels within one coupling-iteration.

The simulations are performed using 12 different classes of droplets. The probability density function of the droplet number for each class of droplets used as boundary conditions corresponds to the experimental data. It is remarkable that almost all classes possess the same injection axial velocity that equals 42 m/s, whereas the standard deviation corresponds to approx. 3 m/s yielding an axial turbulence intensity of 7.5%. Numerical implementation

The governing equations of the carrier gas phase are discretized in the 3D low-Mach number LES code FASTEST. For a detailed description of the finite volume based code, please refer to [18, 24-27]. The parcels are tracked using the LAG3D code in which the equation of motion, the temperature evolution and the evaporation rate are discretized using Euler first/second order schemes and solved explicitly [24-27].

5 Results and Discussions

Figures 2 and 3 show the axial droplet velocities and corresponding fluctuations of all the cases under investigation. Reasonable agreement for the mean droplet velocities is observed in the first cross-section. At x/D=20 and x/D=30, small discrepancies are observed in the averaged droplet velocity. Unfortunately, a comparison between simulated gas phase velocity (that may help to clarify these discrepancies) and experimental data of the carrier phase (that are not available) is not possible. Disagreement at the last cross-sections may originate from the presence of remaining big droplets which are not following the carrier phase. As the gas phase is captured using LES, mean velocities of droplets are well predicted.

The discrepancies between the experimental and numerical results of the velocity fluctuations may be due to the neglect of the effect of SGS on the dispersion of the spray. Indeed small particles, as it is the general case in evaporating droplets, tend to follow the carrier phase dynamics, which is captured by the resolved part and the SGS contribution. This SGS dispersion is unfortunately not included yet.
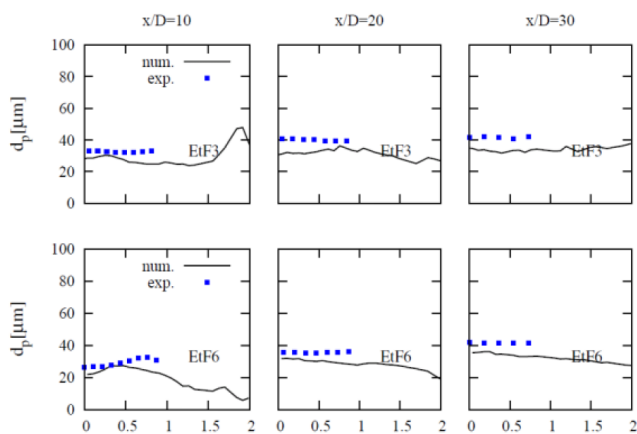
Figure 5: Radial profiles of the droplet mean diameter at different distances from the nozzle exit plane. The x-axis represents r/D

The temperature results in Figure 4 agree favorably well with the experimental data. Ethanol flames are broader than the acetone flames as compared in [27]. Figure 5 displays the droplet mean-diameters at different cross-sections. A good agreement between the experimental data and the numerical simulation for all test cases is observed.

Though the dispersed phase includes 12 different classes and demonstrates a poly-disperse flow, the spray mean-diameters show nearly constant uniform profiles. This effect may be caused by the quick vaporization of the small classes that includes small droplet diameters, i.e. below 20 ïÅŋm. Larger droplets, however, evaporate slower, they are dragged from the injection location to the nozzle exit within a highly turbulent flow, which increases the homogeneity of the class distribution in the pre-vaporization zone. Thus the spray mean diameter shows an approximately uniform profile in the radial direction.

6 Conclusion

Using an LES based Eulerian-Lagrangian approach the impact of mass loading on turbulent spray combustion was evaluated in terms of droplet velocities and fluctuations, exhaust gas temperature, and droplet diameters at different distances from the exit planes.
The axial droplet velocities predicted by simulations agree well with the experimental data. The discrepancies of the corresponding fluctuations can be attributed to the spray-wall interaction at the nozzle exit or/and to the deficiency of capturing the resolved instantaneous fluid velocity. This may evidence the necessity of a SGS dispersion model for evaporating droplets.
The rate of vaporization influences the formation of the fuel/air mixture. The resulting mixture fraction of ethanol/air indicates a premixed behavior. The evolving droplets along with the droplet mean diameters are predicted in acceptable agreement with experimental data.

With respect to spray combustion properties, the FGM concept allowed to capture well the flame height and lift-off. The temperature profiles demonstrated a fair agreement with the measurements. However there are needs for urgent improvements. For instance, concerning temperature predictions, heat losses due to radiation and heat sinks because of spray evaporation should be considered while generating the FGM table. The SGS dispersion model should also be included. All these tasks are work in progress.

Acknowledgements

References

[1] M. Sanjosé, J.M. Senoner, F. Jaegle, B. Cuenot, S. Moreau, T. Poinsot, Fuel injection model for Euler-Euler and Euler-Lagrange large-eddy simulations of

an evaporating spray inside an aeronautical combustor, International Journal of Multiphase Flow, Volume 37, Issue 5, June 2011, Pages 514-529

[2] J. Bellan, L.C. Selle, Large Eddy Simulation composition equations for single-phase and two-phase fully multicomponent flows Original, Proceedings of the Combustion Institute, Volume 32, Issue 2, 2009, Pages 2239-2246

[3] N. M. Marinov: A detailed chemical kinetic model for high temperature ethanol oxidation. Int. J. Chem. Kinet., 31: 183-220, 1999

[4] J. Pozorski, S.A. Apte: Filtered particle tracking in isotropic turbulence and stochastic modeling of subgrid-scale dispersion, Int. J.of Multiph. Flow, Vol. 35 (2) pp. 118-128, 2009

[5] C. Pera, J. Réveillon, L. Vervisch, P. Domingo, Modeling subgrid scale mixture fraction variance in LES of evaporating spray, Combustion and Flame, Volume 146, Issue 4, September 2006, Pages 635-648.

[6] M.R.G. Zoby, S. Navarro-Martinez, A. Kronenburg, A.J. Marquis, Evaporation rates of droplet arrays in turbulent reacting flows, Proceedings of the Combustion Institute, Volume 33, Issue 2, 2011, Pages 2117-2125.

[7] M. Germano, U. Piomelli , P. Moin, and W. H. Cabot, A dynamic sub-grid scale eddy viscosity model, 1991, Phys. Fluids A, 3: 1760-1765.

[8] P. Sagaut, Large Eddy Simulation for incompressible Flows, Springer, Berlin, 2001

[9] B. Wegner, A. Maltsev, C., Schneider, A., Sadiki, A., Dreizler, J., Janicka, Assessment of unsteady RANS in predicting swirl flow instability based on LES and Experiments. International Journal of Heat and Fluid Flow, 2004, 25:528-536.

[10] B. Abramzon and W. A. Sirignano, Droplet Vaporization Model for Spray Combustion Calculations, Int. J. Heat Mass Transfer, Vol. 32, 1989, pp. 1605-1618

[11] R. S. Miller, K. Harstad, and J. Bellan. Evaluation of equilibrium and non-equilibrium evaporation models for many gas-liquid flow simulations. Int. J. Multiphase Flow, 24:1026-1055, 1998

[12] CHEM1D. http://www.tue.nl/en/university/departments/mechanical-engineering/research/research-groups/combustion-technology/flamecodes/chem1d/

[13] U. Eguz, L.M.T. Somers, L.P.H. de Goey, Modeling of PCCI Combustion with the FGM approach, 13th International Conference on Numerical Combustion April 27-29, 2011, Corfu, Greece

[14] C. Pierce and P. Moin, Progress variable approach for large eddy simulation of turbulent non-premixed combustion, J. Fluid Mechanic, Vol. 504:73-97

[15] H.W. Ge and E. Gutheil, Probability density function (pdf) simulation of turbulent spray flows, Atomiz. Sprays 16 (2006), pp. 531-542.

[16] M. Mortensen, R. W. Bilger "Derivation of the conditional moment closure equations for spray combustion" Combustion and Flame, Volume 156, Issue 1, 2009, Pages 62-72

[17] A. R. Masri, J. D. Gounder, Turbulent Spray Flames of Acetone and Ethanol Approaching Extinction, Journal: Combustion Science and Technology, vol. 182, 2010, pp. 702-715

[18] T. Lehnhäuser and M. Schäfer. Improved linear interpolation practice for finitevolume schemes on complex grids. Int. J. Numer. Meth. Fluids, 38(7), 2002, pp 625-645,

[19] A. Sadiki, M. Chrigui, J. Janicka, M.R. Maneshkarimi, Modeling and Simulation of Effects of Turbulence on Vaporization, Mixing and Combustion of Liquid-Fuel Sprays, In: Flow Turb. Comb., 75 (1-4), (2005)

[20] A. W. Vreman, B. A. Albrecht, J. A. van Oijen, L. P. H. de Goey, R. J. M. Bastiaans: Premixed and non-premixed generated manifolds in large-eddy simulation of Sandia flame D and F. Combust Flame 153, 394-416, 2008

[21] B. Fiorina, O. Gicquel, L. Vervisch, S. Carpentier, N. Darabiha: Premixed turbulent combustion modelling using tabulated detailed chemistry and PDF, Proc. of the combustion institute, Vol. 30, pp. 867-874 (2005)

[22] J. Janicka, A. Sadiki: Large Eddy Simulation of turbulent combustion systems, Proc. Of the combustion institute, 30, pp. 537-547, 2005

[23] S.S. Sazhin.: Advanced models for fuel droplet heating and evaporation, Progress in Energy and Combustion Science 32, pp. 162-214, 2006

[24] M. Chrigui, A. R. Masri, Amsini Sadiki, Johannes Janicka,Large Eddy Simulation of a Polydisperse Ethanol Spray Flame, Flow Turbulence and Combustion, Volume 90, Issue 4, pp 813-832, June 2013

[25] M. Chrigui, J. Gounder, A. Sadiki, A. R. Masri, J. Janicka, Partially premixed reacting acetone spray using LES and FGM tabulated chemistry, Combustion and Flame, Volume 159, Issue 8, Pages 2718-2741, August 2012

[26] A. Sadiki, M. Chrigui, and A. Dreizler, Thermodynamically Consistent Modelling of Gas Turbine Combustion Sprays, Fluid Mechanics and Its Applications 102, Flow and Combustion in Advanced Gas Turbine Combustors DOI 10.1007/978-94-007-5320-4 3,

[27] A. Sadiki, M. Chrigui, F. Sacomano, A. R. Masri: Large Eddy Simulation of diluted turbulent spray combustion based on FGM methodology: Effect of fuel and mass loading, TCS3-Book-chapter, Springer Verlag (in print).

[28] H. Baya Toda, O. Cabrit, K. Truffin, G. Bruneaux, F. Nicoud: A Dynamic Procedure for Advanced Subgrid-scales Models and Wall-bounded Flows, TSFP7, Vol 3, (Ottawa) 2011

[29] S. Ayyapureddi, U. Egüz, C. Bekdemir, L. M. T. Somers, L. P. H. de Goey: Application of the FGM Method to Spray A Conditions of the ECN database, ICLASS 2012, Heidelberg, Germany.

A Model for Auto-Ignition and Heat Release in Turbulent Flows and its Application to Thermoacoustic Analysis

R. Kulkarni, M. Zellhuber and W. Polifke

Lehrstuhl für Thermodynamik, TU München, Boltzmannstr. 15, 85747 Garching, Germany.

Abstract

An LES model for (ternary) mixing, auto-ignition and heat release in turbulent flows is presented. The model formulation combines tabulated chemistry, parametrized with mixture fractions and a composite progress variable, with the Eulerian stochastic fields turbulence-chemistry interaction model. Results of extensive validation studies are summarized, which indicate that the model captures autoignition regimes and lift-off heights with good quantitative accuracy. In the context of combustion dynamics, it is then shown how the response of location and intensity of heat release to flow perturbations, which is an important factor for thermoacoustic stability, can be modeled.

1   Introduction

Sequential combustion successfully utilizes a two-stage combustion process to achieve high thermodynamic efficiency and low NOx emissions in stationary gas turbines. The burner design and the combustion regime in the second combustor differ significantly from standard configurations, as the flame is stabilized by auto-ignition in an oxidizer stream characterized by high temperatures and reduced oxygen content [1, 2]. Another characteristic of sequential combustors is that there are multiple streams of air, vitiated air, and fuel, respectively ("ternary mixing"). Chemical reactions rates are comparatively slow, such that the temporal and spatial scales of mixing and reaction are not segregated. Similar conditions are found in other low-emission combustion concepts that utilize some form of exhaust gas recirculation, such as the MILD (Moderate or Intensely Low Oxygen Dilution) regime [3].

For the further development of sequential or MILD combustion technology, there is a pressing need to develop accurate, yet computationally efficient models for (ternary) mixing, auto-ignition and heat release in turbulent flows. The present paper introduces the approach of Kulkarni et al. [4, 5], which combines the Eulerian stochastic fields model with tabulated chemistry for auto-ignition and heat release. The lookup-tables are parametrized with mixture fraction(s) and progress variable. Results of validation studies are summarized briefly, extension and applications of the model to the study of flame dynamics – in particular the response of the flame to acoustic perturbations – are outlined. The latter investigations are relevant for analysis and control of thermoacoustic instabilities, which have become an important aspect in gas turbine development since the widespread introduction of lean premix combustor technology.

2   Combustion model description

The model of Kulkarni et al. [4, 5] for auto-ignition and heat release in turbulent flows combines the *stochastic fields* turbulence-chemistry interaction model [6, 7, 8] with tabulated chemistry based on mixture fractions and a composite progress variable [9, 2]. Details are described in the next two subsections.

2.1   Chemistry tabulation

Various methods are available to reduce the chemistry implicitly or explicitly in order to limit the computational demands of reactive LES. In implicit methods of tabulation, the chemistry is tabulated as a function of few key parameters that describe mixing (mixture fraction Z or mixture fractions Z_1, Z_2 for binary mixing) and the progress of reactions (progress variable Y_c). The present work uses a tabulation method based on homogeneous reactors with detailed chemistry. To properly tabulate the slow pre-ignition chemistry, a combination of an intermediate species and a product is used to define a "composite progress variable". For methane, the normalized sum of mass fractions of CH_2O, CO and CO_2 is used as the progress variable, whereas HO_2 and H_2O are used for hydrogen. The importance of including an intermediate species was shown by Kulkarni et al. [5]. In that work, a progress variable based on CH_2O, CO and CO_2 performed better than formulations using only CO and CO_2 or solely CO_2. The homogeneous reactors at various mixture fractions march in time and during their evolution, the rate of change of the progress variable is tabulated as a function of the progress variable. All the other thermo-chemical quantities of interest are mapped to the two quantities transported in LES.

2.2   Stochastic fields turbulence-chemistry interaction model

As the chemistry is not fully resolved in LES, the non-linear chemical source term for the reactive scalar, i.e. the progress variable in the present work, needs to be modelled. Two approaches for the closure of this term are common, viz. the presumed and the transported filtered density function (FDF) method. A composition transported FDF method based on an Eulerian formulation [6, 7, 8] is considered here, also known as the "Eu-

lerian Monte Carlo" or "stochastic fields" method. The major advantage of the transported FDF methods is the readily closed chemical source term. The model is based on a system of stochastic differential equations equivalent to the joint FDF evolution equations. N stochastic fields are considered, which represent the possible sub grid composition. The 'stochastic fields' are continuous (differentiable) in space and white (non-differentiable) in time. The fields can be used to represent the density-weighted sub-grid FDF of any scalar (here written for Z) by:

$$P_{sgs}(Z; x, t) = \frac{1}{N} \sum_{n=1}^{N} \delta \left[Z - Z^n(x, t) \right] \qquad (1)$$

The evaluation of the first order moment (mean) can be done by

$$\widetilde{Z} = \frac{1}{N} \sum_{n=1}^{N} Z^n \qquad (2)$$

Instead of solving the stochastic partial differential equations (PDEs) for all the chemical species, they are solved for the mixture fraction and the progress variable only:

$$\bar{\rho} dZ^n = -\bar{\rho} \widetilde{u}_i \frac{\partial Z^n}{\partial x_i} + \frac{\partial}{\partial x_i} \left[(D_l + D_t)) \frac{\partial Z^n}{\partial x_i} \right] dt \\ + (2\bar{\rho}(D_l + D_t))^{1/2} \frac{\partial Z^n}{\partial x_i} dW_i^n - \frac{\bar{\rho}}{2\tau_{sgs}} \left(Z^n - \widetilde{Z} \right) dt \qquad (3)$$

$$\bar{\rho} dY_c^n = -\bar{\rho} \widetilde{u}_i \frac{\partial Y_c^n}{\partial x_i} + \frac{\partial}{\partial x_i} \left[(D_l + D_t)) \frac{\partial Y_c^n}{\partial x_i} \right] dt \\ + (2\bar{\rho}(D_l + D_t))^{1/2} \frac{\partial Y_c^n}{\partial x_i} dW_i^n - \frac{\bar{\rho}}{2\tau_{sgs}} \left(Y_c^n - \widetilde{Y}_c \right) dt \\ + \bar{\rho} \dot{\omega}_c^n (Z^n, Y_c^n) dt \qquad (4)$$

The third term on the right hand side is the stochastic term, which depends on the effective diffusivity, the scalar gradient, and the Wiener term. The latter is approximated by time-step increments $dt^{1/2}\eta_i$, where η_i is a dichotomic random number. The fourth term is the micro-mixing model, which in this work is the IEM (Interaction by Exchange with the Mean). The sub-grid time scale is given by $\tau_{sgs} = \bar{\rho}\Delta^2/(\mu + \mu_{sgs})$. The last term in 4 is the chemical source term for the progress variable. This term is absent in the mixture fraction PDE as the mixture fraction is a conserved scalar. The source term of the progress variable is a function of the mixture fraction and the progress variable of that particular field. The source terms for the species solved in LES can be calculated from

$$\widetilde{\dot{\omega}_\alpha} = \frac{1}{N} \sum_{n=1}^{N} \dot{\omega}_\alpha^n (Z^n, Y_c^n) \qquad (5)$$

3 Model validation

The model presented in the previous section has been validated extensively, making use of experimental data on hydrogen autoignition from Cambridge [10, 11], DNS data for a similar configuration from ETH Zürich [12, 13] and finally the Delft flame [3], which is a methane lifted flame that emulates MILD combustion.
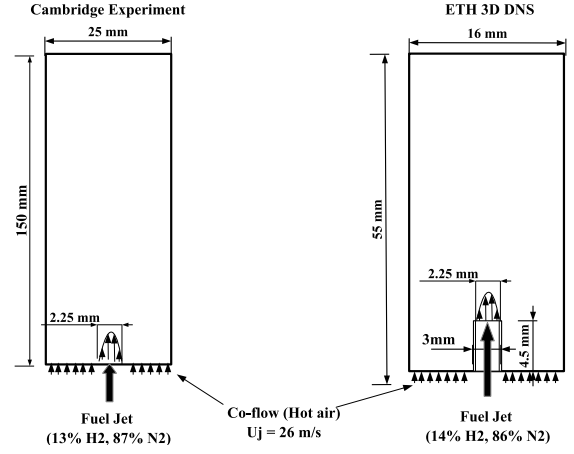
Figure 1: Schematic of numerical setup used for the Cambridge experiment [10, 11] and the ETH 3D DNS [12, 13].

Table 1: Simulated Cases

| Case | Temperature | | Observed flame behavior |
	Co-flow [K]	Fuel [K]	
0	950	750	Random Spots
1	955	750	Random Spots
2	960	750	Random Spots
3	980	750	Flashback
DNS	955	850	Random Spots

3.1 Hydrogen autoignition

The hydrogen autoignition experiment in a Confined Turbulent Hot Co-flow (CTHC) apparatus was performed by Markides et al. [10, 11] at Cambridge University. The second test case, inspired by the Cambridge experiments, is a 3D DNS performed by Kerkemeier et al. [12, 13] at ETH Zürich. The computational domains of the two test cases as used for the present LES study are shown in 1.

In both test cases, a diluted hydrogen jet (13% and 14% by mass for the experiment and the DNS, respectively) is injected into a co-flow of hot air. The nozzle diameter is 2.25 mm. The co-flow in the experiments was confined in a quartz tube with a diameter of 25 mm and a length of 250 mm. However, a length of 150 mm is considered in this work for the LES. The DNS domain had a diameter of 16 mm and a length of 55 mm. The fuel temperature in the experiment was controlled electrically to 750 K, whereas in the DNS it was set to 850K. The co-flow and the fuel jet had a bulk mean velocity of 26 m/s. The turbulence intensity (TI) and length scale (L_t) for the experiments measured at the injector plane were 14 % and 3 mm, respectively. In the DNS, TI of 14 % and l_t of 4.5 mm is imposed at the co-flow inlet. The boundary conditions for all the test cases are summarized in 1.

3.2 LES setup for hydrogen case

The Li [14] mechanism is used in LES, as for the DNS. The open source code CANTERA [15] is used to tabulate the chemistry, with 100 points in the mixture fraction space and 75 in the progress variable space. The mixture fraction with the lowest auto-ignition delay time is
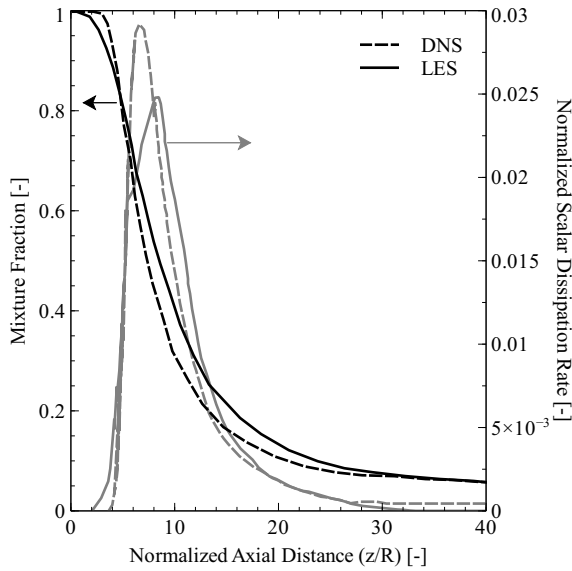
Figure 2: Axial distribution of the mean mixture fraction and scalar dissipation rate.

called the most reactive mixture fraction. More points are clustered around the most reactive mixture fraction. Velocity inlet boundary conditions were used for fuel and co-flow. For the turbulent inlet, the "vortex generator" boundary condition [16, 17] is used. A time stepping of 1e-6 s is used for all the simulations, which corresponds to a Courant number < 1.0.

3.3 Hydrogen validation results

3.3.1 Mixing

The performance of a combustion model depends largely on a reliable mixing prediction. To validate the mixing field, the DNS and LES time averaged resolved mixture fraction mean and the scalar dissipation rate are plotted in 2.

LES predicts a faster rate of mixture fraction decay close to the jet core ($z < 5$). The scalar dissipation rate describes the rate of mixing. Its magnitude (resolved) in LES starts to increase earlier than in DNS. The reason for the discrepancy is that the LES curve includes only the resolved scalar dissipation rate. The peaks of the scalar dissipation rate in LES and DNS are at a normalized axial position of 5.8. Overall, there is a good agreement between DNS and LES mixing.

3.3.2 Autoignition length

3 on the left shows the time averaged OH mass fraction distribution on the central cross-section. The solid line shows the ignition criteria. The graph on the right hand side of Fig. 3 shows the axial distribution of OH mass fraction along with the ignition criteria. To define the ignition length, an OH mass fraction criterion (1e-4) was used in the ETH DNS study [12]. The mean autoignition length predicted by DNS is 25.6 R, where R is the jet radius. The LES predicted autoignition length is 25.1 R. The difference of 0.5 times the jet radius, which is equivalent to 0.56 mm, is of the order of the LES grid size in axial direction (approx. 0.3-0.4 mm). In the Cambridge hydrogen autoignition experiments, the autoignition length and the flame behavior was found to depend strongly on the co-flow temperature. Higher temperatures resulted into lower ignition lengths with higher probability of autoignition. In the experiment, average
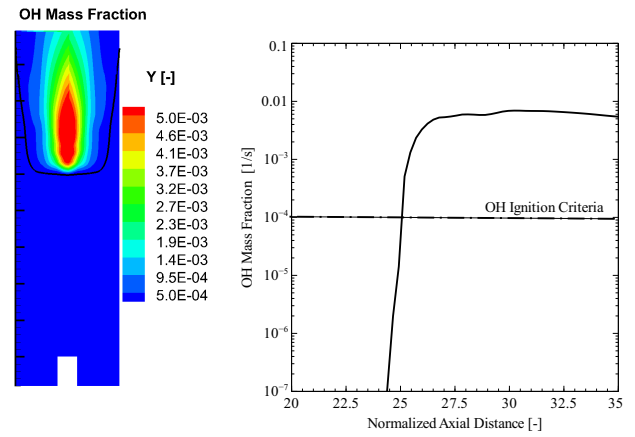
Figure 3: Left: LES mean OH mass fraction contour on the central cross-section. Line: OH autoignition criteria ($Y_{OH} = 1.e-4$). Right: LES axial distribution of OH mass fraction.
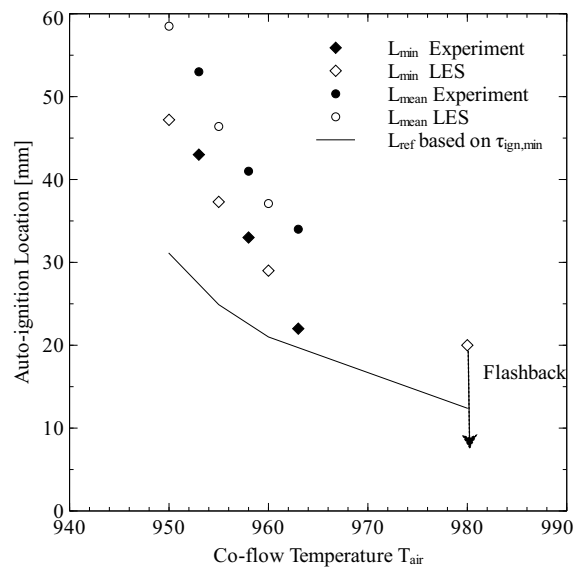
Figure 4: Minimum and mean autoignition locations.

OH chemiluminescence images were used to determine the mean and minimum auto-ignition length. A value of 3% of the maximum time averaged OH signal was considered to be the minimum auto-ignition location and the peak of the averaged OH distribution was considered to be the mean autoignition location. 4 shows the minimum and mean autoignition location from the experimental measurements and LES. For cases 0, 1, and 2, the random ignition spot regime is observed in LES and in experiments. For case 3, flashback is observed after ignition and an attached flame is observed in steady state. 4 validates the capability of the combustion model to capture the non-linear dependence of autoignition chemistry on temperature.

3.4 Methane lifted flame experiment [3]

The next test case is the Delft Jet in Hot Co-flow (DJHC) flame performed by Oldenhof et al. [3, 18] at the Delft University. 5 shows the sketch of the flame. The experimental setup consists of a primary burner and a partially premixed secondary burner. A jet of fuel enters into a co-flow of hot air with low oxygen content. The diameter of the injector is 4.5 mm. The co-flow is generated by an annular secondary burner of 82.8 mm diameter upstream
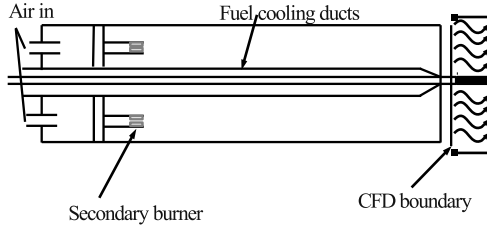
Figure 5: Test case sketch

of the primary burner. It consists of a ring of premixed flames with air injected on both sides of the ring. The fuel tube is cooled using air stream. Due to the cooling air and the air injected along the secondary burner, the co-flow at the inlet of the primary burner consists of a nonuniform profile of temperature and species.

The temperature and mass fraction of oxygen in the co-flow at the inlet of the primary burner are shown in 6. 2 shows the boundary conditions for the fuel jet and the co-flow. Favre averaged velocities and Reynolds stresses were measured using Laser Doppler Anemometry (LDA). The temperature was measured using Coherent Anti-Stokes Raman Spectroscopy (CARS). The radial profile of oxygen concentration was measured using probe measurements [3, 18].

| Case | Re_j | $T_{co,max}$ | $T_{co,min}$ | $X_{co,min}$ |
Case	[-]	[K]	[K]	[-]
DJHC-I	4100	1540	695	0.055
DJHC-I	8800	1540	695	0.055
DJHC-V	4600	1460	695	0.066

Table 2: Simulated Cases
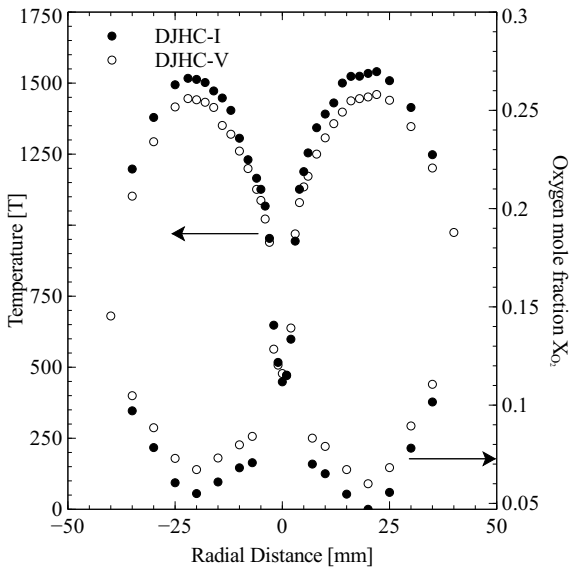
Figure 6: Temperature and oxygen mole fractions at the boundary conditions for DJHC-I and DJHC-V.

3.5 LES setup for methane case

To consider the non-uniform boundary condition, an additional conserved scalar (mixture fraction) is used in LES. The mixture fraction Z_1 is used for the fuel stream and Z_2 for the air stream. The maximum temperature and the minimum oxygen concentration in the co-flow were considered as boundary conditions for the hot gas. At the boundary conditions, the mixture fraction Z_2 is calculated as a function of the temperature. Following

equation describes the method of calculating the second mixture fraction at the co-flow inlet boundary:

$$Z_2 = \frac{T_{co,max} - T}{T_{co,max} - T_{air}} \quad (6)$$

The assumption behind this equation is that the oxygen concentration and temperature are correlated, which is true closer to the axis. This is not necessarily true for the outer part of the co-flow due to wall heat losses. These effects are neglected in the present work as those regions are not of interest. Tabulation is done for various combinations of the mixture fractions. The initial conditions (reactant mass fractions and enthalpy) for the homogeneous reactors are calculated using:

$$\phi_i^{t=0} = Z_1 * \phi_{i,Z_1} + Z_2 * \phi_{i,Z_2} + (1 - Z_1 - Z_2) * \phi_{i,Z_3} \quad (7)$$

In LES, stochastic fields equations for the mixture fractions Z_1 and Z_2 and the progress variable are solved. 3 is valid for both the mixture fractions. The source term for the progress variable in 4 is a function of the mixture fractions and the progress variable $\bar{\rho}\dot{\omega}_c^n(Z_1^n, Z_2^n, Y_c^n)$. The filtered quantities of interest, e.g. the filtered chemical source term of a species, are calculated using:

$$\widetilde{\dot{\omega}_\alpha} = \bar{\rho}\frac{1}{N}\sum_{n=1}^{N}\dot{\omega}_\alpha^n(Z_1^n, Z_2^n, Y_c^n) \quad (8)$$

The GRI30 mechanism is used for the tabulation with $CH_2O + CO + CO_2$ as a progress variable.

3.6 Methane validation results

3.6.1 Velocity and mixing field

7 shows the radial velocity distribution at various axial locations for DJHC-I at Re number of 4100. A satisfactory velocity distribution is obtained in the LES. 8 shows the Z_2 mixture fraction contour for the cases studied in this work. A line showing the stoichiometric mixture fraction $Z_{1,st} = 0.02$ is also depicted. The distribution of Z_2 on the iso-line of $Z_{1,st}$ is important, as the reactions are fastest at mixture fraction close to this value for a given Z_2. A lower value of Z_2 will mean a higher amount of hot gas at that location. The hot gas accelerates the chemistry due to the higher temperature. The distribution of Z_2 for DJHC-I 4100 and DJHC-V 4500 are quite similar due to similar jet Re numbers. For DJHC-I with Re=8800, lower amount of Z_2 is observed in comparison to the other two cases. This is due to the faster entrainment of the hot gases into the jet. This was also observed in the RANS simulation of De et al. [19], which is discussed at length in [18].

3.6.2 Lift-off height

De et al. [19] related the lift-off height to the probability of the presence of flame pockets. A flame pocket is defined where the OH mass fraction attained a value of 1e-3. $Pb_1(z)$ is the probability of finding a flame pocket anywhere on a radial line stretching outward from the burner axis as a function of the axial height. In this method, a location with OH signal at any radial distance was accounted. As suggested by Oldenhof et al. [18], a $Pb_1 = 0.5$ is defined as the lift-off height. 3 reports the experimentally observed lift-off heights with LES. For similar Reynolds number, the autoignition length increases with reduced temperature. This effect is expected due to the reduced reaction rates or increased

Figure 7: Radial velocity distribution for DJHC-I Re=4100 at various downstream locations

Figure 8: Time averaged air mixture fraction distribution at the central cross section. Line: Most reactive fuel mixture fraction.

Table 3: Mean Lift-off heights

Case	Experiment[18] [mm]	LES [mm]
DJHC-I $Re_j = 4100$	80	85
DJHC-I $Re_j = 8800$	78	78
DJHC-V $Re_j = 4600$	100	95

with simplified setups which have a similar topology as the real configuration of interest. Hence, the lab-scale setups used for the validation are not suitable for the investigation of flame dynamics. Therefore, in [20, 21, 22], a perfect premix generic geometry was investigated using LES with the modelling ansatz introduced above. The setup consists of a backward-facing step, with an homogeneous mixture of methane and vitiated air applied at the inlet, at a temperature of 1271 K and an average pressure of 18 bar. Despite the simplification of the perfect premixing, this setup proved to deliver a good insight into the dynamics flame behaviour.

Applying a combustion model to thermoacoustic problems always raises the question whether all relevant flame dynamics are captured. Therefore, one has to formulate hypotheses regarding potential thermoacoustic feedback mechanisms and evaluate whether these can be described by the model. In the case of the premix combustor, the following mechanisms were identified in the high-frequency regime: (1) variations of density, (2) periodic displacement of the flame, (3) flame surface variations linked to coherent flame wrinkling, and (4) modulations of chemical reaction rates due to acoustic pressure and temperature variations. Under technical premix conditions, mixing fluctuations might also contribute to flame dynamics, they can be described using the mixture fraction ansatz. The mechanisms (1)-(3) are properly captured by the combustion model, provided a fully compressible formulation of the LES transport equations. The fourth mechanism, however, requires some additional modelling, unless the chemistry tables are extended by an additional dimension. In order to avoid an increase in tabulation dimension and interpolation effort, an approximate description based on a pressure sensitivity factor φ_p is suggested. It was introduced in [23] and found to give satisfactory quantification of the impact of combined acoustic pressure and temperature variations on auto-ignition reaction rates. The factor φ_p shows only small dependencies on reaction progress and mixture fraction and can therefore be used in straightforward manner in CFD simulations, see [22, 23].

As a next step, one has to specify the main objective of the thermoacoustic investigation. If one is interested in quantifying flame transfer functions over wide frequency ranges, one ought to perform broadband frequency excitation of flames and retrieve the relevant data using system identification techniques, see e.g. [24, 25]. Alternatively, one can also apply single-frequency excitation of specific modes, as done in [20, 21, 22]. This approach generally allows to gain a more profound physical understanding, provided that appropriate post-processing tools are employed. Harmonic analysis tools represent the straightforward choice for single-frequency excitation, but POD and DMD can also be options. The application of these tools allows to observe the different feedback mechanisms [20] and to quantify thermoacoustic energy sources, using e.g. the Rayleigh index.

Finally, the CFD-based investigation of flame dynamics is ideally accompanied by a theoretical model that describes the various contributions to flame dynamics.

ignition delays with reduced temperatures. Both, in the experiments and LES (table 3), an increase in the lift-off height with jet velocity (DJHC-I) is observed. This is contrary to the expectation, as increased jet velocity should increase the lift-off height. This contradictory observation in DJHC flame is due to the faster mixing of the hot part of the co-flow with the jet, which promotes reactions and reduces the auto-ignition length. These results not only show the capability of the model to capture the computationally challenging MILD combustion, but also the impact of turbulence on mixing and autoignition. The topic is discussed in detail for the Cambridge setup in [4].

4 Thermoacoustic analysis

The previous validation results underline the wide applicability of the method for steady-state flow conditions, showing accurate predictions of auto-ignition behaviour for different setups and fuels. These investigations were performed on lab-scale burners, which allow a detailed insight into the fundamentals of turbulent auto-ignition phenomena. Nevertheless, they are quite different in comparison to industrial sequential combustors, since they do not feature a sudden area change and consequently a forced recirculation of combustion products.

For thermoacoustic analysis, it is important to deal

This was for instance made in [21], where the CFD results were used for a validation of the analytical model. Going even further, one can formulate, as in [22], general flame transfer function expressions that can be used for a-priori estimation of combustor stability using network models or finite-element calculations.

5 Conclusions

An LES turbulent combustion model based on tabulated chemistry and stochastic fields approach is introduced and validated against two experiments and a DNS autoignition test case. The model captures autoignition lengths and regimes accurately. The model is aimed at predicting the heat release rate distribution in sequential gas turbine combustors, but is also applicable for MILD combustion. In addition, it is described how the combustion model can be used for thermoacoustic analysis. This asks first for an in-depth understanding of the model's capabilities, as well as for the availability of appropriate excitation procedures and post-processing tools, in order to be able to obtain practical data that can be used for thermoacoustic stability prediction.

Acknowledgment

References

[1] F. Joos, P. Brunner, B. Schulte-Werning, K. Syed, and A. Eroglu, "Development of the sequential combustion system for the ABB GT24/GT26 gas turbine family," in *Proc. ASME Turbo Expo, 1996-GT-315*, 1996.

[2] M. Brandt, W. Polifke, B. Ivancic, P. Flohr, and B. Paikert, "Auto-ignition in a gas turbine burner at elevated temperature," in *Int'l Gas Turbine and Aeroengine Congress & Exposition*, no. ASME 2003-GT-38224, (Atlanta, GA, U.S.A.), June 2003.

[3] E. Oldenhof, M. Tummers, E. van Veen, and D. Roekaerts, "Ignition kernel formation and lift-off behaviour of jet-in-hot-coflow flames," *Combust. and Flame*, vol. 157, pp. 1167–1178, 2011.

[4] R. Kulkarni, M. Zellhuber, and W. Polifke, "LES based investigation of autoignition in turbulent co-flow configurations," *Combustion Theory and Modelling*, vol. 17, no. 2, pp. 224–259, 2013.

[5] R. Kulkarni and W. Polifke, "LES of Delft-Jet-In-Hot-Coflow (DJHC) with tabulated chemistry and stochastic fields combustion model," *Fuel Process. Technol*, vol. 107, pp. 138–146, 2013.

[6] L. Valino, "A field Monte Carlo formulation for calculating the probability density function of a single scalar in a turbulent flow," *Flow Turbul. Combust.*, vol. 60, no. 2, pp. 157–172, 1998.

[7] W. Jones, S. Navarro-Martinez, and O. Röh, "Large eddy simulation of hydrogen auto-ignition with a probability density function method," *Proceedings of the Combustion Institute*, vol. 31, no. 2, pp. 1765–1771, 2007.

[8] W. Jones and S. Navarro-Martinez, "Large eddy simulation of autoignition with a subgrid probability density function method," *Combustion and Flame*, vol. 150, pp. 170–187, 2007.

[9] D. Bradley, L. K. Kwa, A. K. C. Lau, and M. Missaghi, "Laminar flamelet modelling of recirculating premixed methane and propane-air combustion," *Comb. & Flame*, vol. 71, pp. 109–122, 1988.

[10] C. Markides, *Autoignition in Turbulent Flows*. PhD thesis, University of Cambridge, 2005.

[11] C. Markides and E. Mastorakos, "An experimental study of hydrogen autoignition in a turbulent co-flow of heated air," *Proc Combust Inst*, vol. 30, no. 1, pp. 883–891, 2005.

[12] S. Kerkemeier, *Direct Numerical Simulation of Combustion on Peta-Scale Formats: Application to Non-premixed Hydrogen Autoignition.* PhD thesis, ETH Zürich, 2010.

[13] S. Kerkemeier, C. Frouzakis, K. Boulouchos, and E. Mastorakos, "Numerical simulation of autoignition of a diluted hydrogen plumein co-flowing turbulent hot air," in *AIAA Aerospace Sciences Meeting Including the New Horizons Forum and Aerospace Exposition*, pp. 1–12, 2010.

[14] J. Li, Z. Zhao, A. Kazokov, and F. Dryer, "An updated comprehensive kinetic model of hydrogen combustion," *Int. J. Chem. Kinet.*, vol. 36, pp. 566–575, 2004.

[15] D. Goodwin, "Cantera: Object-oriented software for reacting flows, california institute of technology," tech. rep., web site: http://blue.caltech.edu/cantera/index.html, 2002.

[16] "ANSYS FLUENT academic research, release 6.3 (2006)," tech. rep., 2012.

[17] F. Mathey, D. Cokljat, J. P. Bertoglio, , and E. Sergent, "Assessment of the vortex method for large eddy simulation inlet conditions," *Progr. Comput. Fluid. Dyn.*, vol. 6 (1/2/3), pp. 58–67, 2006.

[18] E. Oldenhof, M. Tummers, E. vanVeen, and D. Roekaerts, "Role of entrainment in the stabilisation of jet-in-hot-coflow flames," *Combust. Flame*, vol. 158, pp. 1553–1563, 2011.

[19] A. De, E. Oldenhof, P. Sathiah, and D. Roekaerts, "Numerical simulation of Delft-Jet-in-Hot-Coflow (DJHC) flames using the eddy dissipation concept model for turbulence-chemistry interaction," *Flow, Turb. Comb.*, vol. 1386-6184, pp. 1–31, 2011.

[20] M. Zellhuber, C. Meraner, R. Kulkarni, B. Schuermans, and W. Polifke, " LES of flame response to transverse acoustic excitation in a model reheat combustor," *J. Eng. Gas Turb. Pow., accepted for publication*, 2013.

[21] M. Zellhuber, J. Schwing, B. Schuermans, T. Sattelmayer, and P. W., "Experimental and numerical investigation of thermoacoustic sources related to high-frequency instabilities," *Int. J. Spray Comb. Dyn., under review*, 2013.

[22] M. Zellhuber and W. Polifke, "Large-eddy-simulation of high-frequency flame dynamics in perfect premix combustors with elevated inlet temperatures," in *Ercoftac workshop on Direct and Large-Eddy Simulation, DLES-9*, 2013.

[23] M. Zellhuber, B. Schuermans, and W. Polifke, "Impact of acoustic pressure on auto-ignition and heat release," *Comb. Theo. Mod., accepted for publication*, 2013.

[24] A. Huber and W. Polifke, "Dynamics of practical premix flames, part I: Model structure and identification," *Int. J. Spray Comb. Dyn.*, vol. 1, no. 2, pp. 199–229, 2009.

[25] L. Tay Wo Chong, T. Komarek, R. Kaess, S. Föller, and W. Polifke, "Identification of flame transfer functions from LES of a premixed swirl burner," in *Proc. ASME Turbo Expo, GT2010-22769*, 2010.

Large Eddy Simulation of a Stratified Turbulent Bluff-body Burner

S. Nambully, L. Vervisch, P. Domingo and V. Moureau

CORIA - CNRS, Normandie Université, INSA de Rouen, Technopole du Madrillet
76800 Saint-Etienne-du-Rouvray, France

Abstract

The Cambridge turbulent bluff-body flame burner of S. Hochgreb's group, featuring mixture stratified in equivalence ratio is simulated using Large Eddy Simulation. Results are used to analyze the flame structure versus the level of stratification. Comparison of statistically averaged velocities against measurements is also discussed.

1 Introduction

Large Eddy Simulation of the two stratified non-swirling configurations of the Cambridge burner studied by Sweeney and co-workers [1, 2] is presented. The sub-grid combustion closure relies on a physical space filtering operation, with a filter size determined locally depending on the resolved and sub-grid scale flame properties.

A decomposition of the flame response into premixed, diffusion and partially premixed flamelets is performed, to conclude that the premixed mode dominates close to the burner, with some partially premixed burning regime further downstream. Overall, the length scales associated to stratification were found to be much larger than that of the reaction zone and flame, resulting in a quasi-homogeneous propagation, predominantly in a back supported stratified combustion regime.

2 Flow configuration and numerics

The Cambridge swirl burner (CSWB) [1] was designed specifically to study stratified combustion subjected to swirling and non swirling flows. This work focusses only on the non-swirling operations of the burner. The burner consists of a closed central ceramic bluff body and is surrounded by two annular jets operated at 8.31 m/s (Re = 5960) and 18.7 m/s (Re = 11540) respectively. There is a large laminar outer coflow at 0.4 m/s to prevent external air entrainment. Details on the geometry of the burner and the measurement techniques may be found in [2]. The two configurations CSWB5 and CSWB9 are summarized in Figure 1.

Two meshes have been used, the cylindrical computational domain spanning 38 cm in diameter and 46 cm in height is decomposed over an unstructured mesh composed of 50 million tetrahedra, with a resolution varying between 300 µm and 400 µm in the flame zone. For CSWB5, a refined mesh simulation involving about 400M

Table 1: Annular jets equivalence ratio and mixture fraction

Case	ϕ_{inner}	ϕ_{outer}	Z_{inner}	Z_{outer}
CSWB5	1.000	0.500	0.0550	0.0291
CSWB9	1.125	0.375	0.0610	0.0210
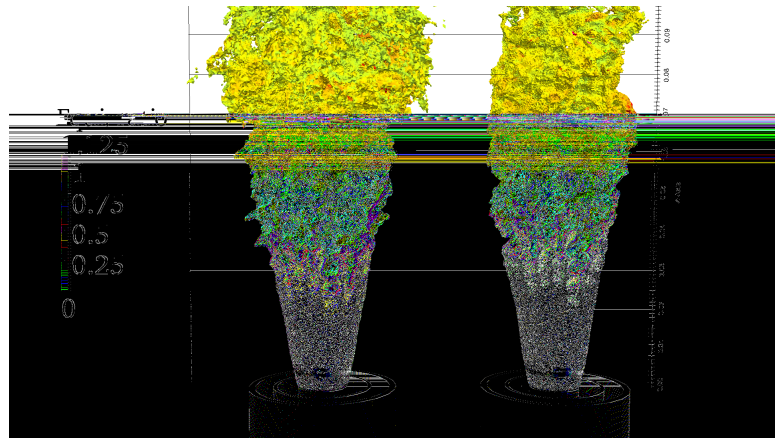
Figure 1: Instantaneous progress variable source term conditioned on the progress variable ($0.01 < \widetilde{c} < 0.99$) colored by equivalence ratio. Left: CSWB5, Right: CSWB9. Every major division of the axis corresponds to 10 mm

cells was also performed, to study the impact of grid resolution on the results, the resolution is then between 150 µm and 200 µm in the reaction zone. The mixture fraction boundary conditions for each case are given in Figure 1 with the coflow mixture fraction set as zero in pure air. Simulations are performed with YALES2, an in-house low-Mach number finite volume solver for unstructured grids with dynamic eddy viscosity modeling [3, 4]. The FLF-PDF turbulent combustion closure is used [5], in which flame filtering in physical space is performed according to the level of sub-grid scale scalar unresolved fluctuations.

3 Turbulent stratified flame properties

In Figure 1, an initial premixed zone up to 30 mm is identified. Between 30 mm and 40 mm, the flame intersects the mixing layer. Further downstream (> 40 mm), stratified combustion appears. Since the inner jet is not as
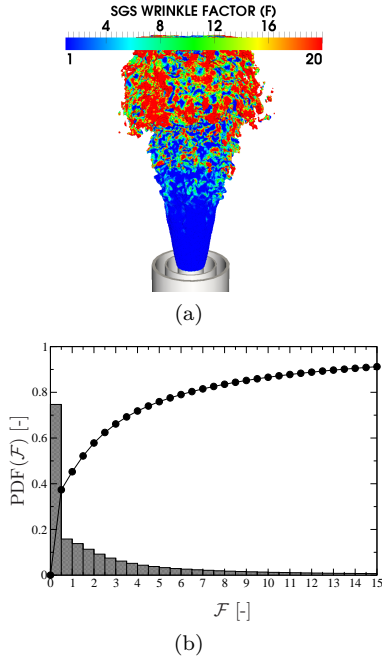
Figure 2: CSWB5 (a): Instantaneous source term colored by $\mathcal{F} = (2k_{SGS}/3)^{1/2}/S_L$. (b): PDF of $\mathcal{F}$ computed over the mesh
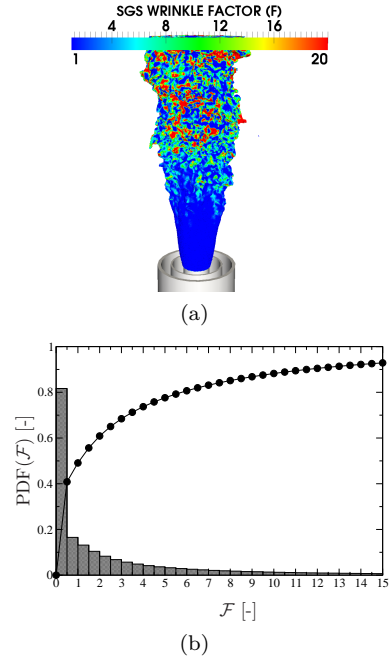
Figure 3: CSWB9 (a): Instantaneous source term colored by $\mathcal{F} = (2k_{SGS}/3)^{1/2}/S_L$. (b): PDF of $\mathcal{F}$ computed over the mesh

turbulent as the outer jet, as depicted by their Reynolds numbers given above, the LES mesh resolves the flame wrinkling where the flame is premixed. Accordingly, in this part of the flame, $\mathcal{F} = (2k_{SGS}/3)^{1/2}/S_L < 1$ and the combustion regime predominantly lies in the wrinkled flamelet regime[1]. This was observed for both the cases. When the shear layer of the inner and outerjets intersects the flame, the presence of smaller structures increases the wrinkling and leads to $\mathcal{F}$ going greater than unity. Figures 2(a) and 3(a) show the instantaneous source term colored by $\mathcal{F}$ depicting the behavior discussed above. Also shown are the cumulative distributions of the probability density function of $\mathcal{F}$ versus $\mathcal{F}$ in Figs. 2(b) and Figure 3(b), confirming that both LES combustion regimes exist in these flames and also that many mesh cells require modeling via a closure accounting for an estimation of sub-grid flame wrinkling.

In order to quantify the extent of stratification in the two cases, it is useful to look at two quantities; the probability distribution of equivalence ratio, and, the probability distribution of the gradient of equivalence ratio across the flame at different heights from the burner exit. Figure 4 shows the distribution of equivalence ratios ϕ for CSWB5 and CSWB9 at heights ranging from 20 mm - 70 mm conditioned in the flame zone ($0.01 < \widetilde{c} < 0.99$, $\widetilde{c}$ is the LES filtered reaction progress variable equal to zero in fresh gases and unity in burnt ones). It is evident that below 30 mm combustion is predominantly of the premixed type with occasional stratification occurring at a frequency controlled by the intersection of mixing layer vortices for both the cases. Frequency spectrum of a probe placed on the shear layer of the inner jet and the outer jet is shown in 5, which reveals a frequency of around 2300 Hz.

For a given height, the curves in Figure 4 are flat-

ter for CSWB9, showing a higher probability for several equivalence ratios to exist at a given height than observed in CSWB5. This is expected since the stratification ratio of CSWB9 is higher than CSWB5 (Figure 1). In spite of the minor differences in both cases, evidently the flame undergoes combustion at lean mixtures and also experiences stratification especially at heights above 30 mm. The span of the equivalence ratio could be considered as a representative degree of stratification. But as seen in literature [6], a complementary parameter that can be looked at is the gradient of equivalence ratio across the flame. A comparison of the probability distribution of the resolved gradients of equivalence ratio at heights ranging from 40 mm - 70 mm for the CSWB5 and CSWB9 cases are shown in Figure 6. Since, up to 30 mm, the flame is in the premixed regime the gradients are zero and not shown here. The plots show that at distances 40 mm and 50 mm from the burner exit, the resolved LES gradient of equivalence ratio is higher for the CSWB9 than CSWB5 case. It should be recalled that these locations fall in the zone where mixing and reaction zones intersect and maximum stratification is found. The plots show an expected trend again, since the global stratification ratio for CSWB9 is higher and consequently a higher gradient is expected. However, going downstream at locations 70 mm and 80 mm, the gradients become comparable in both cases. This is due to the higher turbulence levels leading to higher mixing and the gradients being dissipated.

Similar to the thermal flame thickness, a mixing layer thickness can be defined from the resolved quantities on the LES mesh as

$$\delta_\phi = \left(\frac{\phi^{max} - \phi^{min}}{|\nabla\phi|^{max}} \right). \tag{1}$$

Then for the CSWB5 case at 40 mm, considering the fact that $\phi^{max} = 1.0$, $\phi^{min} = 0.5$ and the most probable value for $|\nabla\phi| \approx 200$ m^{-1} (from Figure 6) an estimate of δ_ϕ can be obtained as 2.5 mm. This is an order of

---

[1]k_{SGS} is the SGS turbulent kinetic energy and S_L the flame speed. When $\mathcal{F} \leq 1$, the sub-grid velocity fluctuations are less than the flame speed implying that the wrinkling is resolved on the LES mesh. When $\mathcal{F} > 1$, sub-grid flame wrinkling requires to be modeled.

CSWB5

CSWB5 - Refined

CSWB9
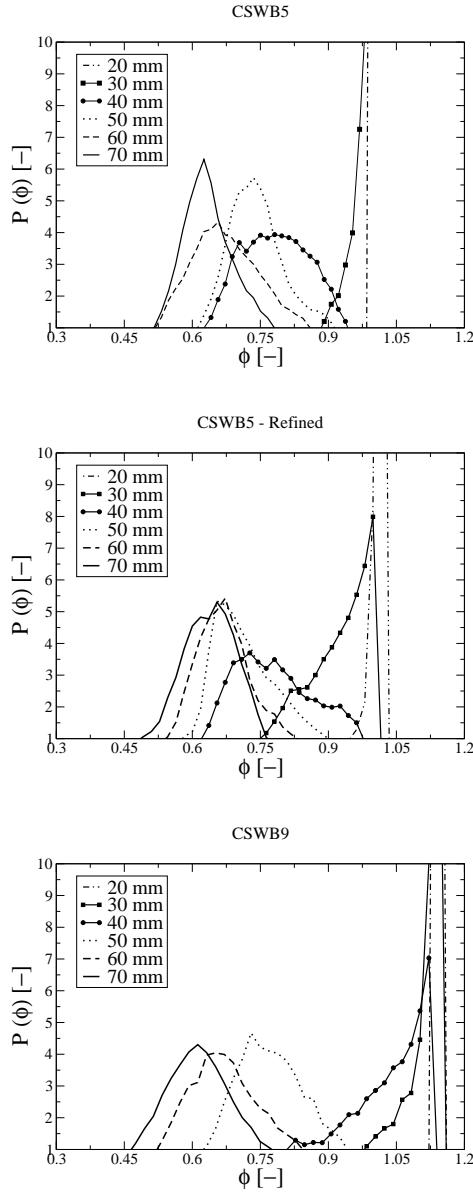
Figure 4: Probability distribution of equivalence ratio at different heights from the burner exit conditioned on the progress variable($0.01 < \widetilde{c} < 0.99$)
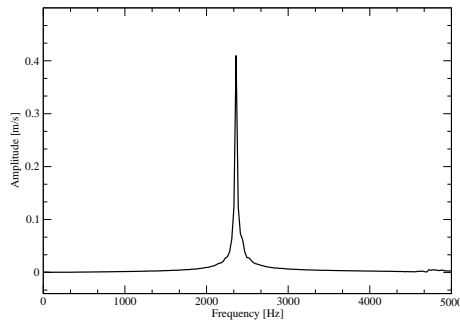
Figure 5: Frequency spectra of the axial velocity of a probe place in the shear layer of the inner and outer jet
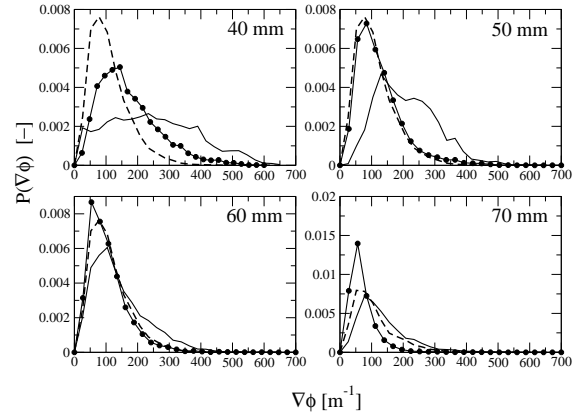
Figure 6: Probability distribution of instantaneous gradient of equivalence ratio as a function of equivalence ratio gradient at different heights for CSWB5 and CSWB9 conditioned on progress variable ($0.01 < \widetilde{c} < 0.99$). Lines with circles: CSWB5 coarse mesh, Dashed line: CSWB5 refined mesh. Line: CSWB9 coarse mesh

magnitude higher than the typical reaction layer thickness of the laminar flame for the stoichiometric mixture which is around 0.1 mm. Similarly for the CSWB9 case at 40 mm, taking $\phi^{max} = 1.125$, $\phi^{min} = 0.375$ and $|\nabla \phi|^{max} \approx 300$ m^{-1} we obtain $\delta_\phi \approx 2.5$ mm, which again is much larger than the reaction zone thickness. Due to the much larger scales of stratification compared to the flame thickness, it might explain the validity of the premixed flamelet hypothesis to simulate this configuration, owing to a quasi-homeogeneous propagation of the flame locally. Nevertheless, this intermediate conclusion can be refined by looking at the decomposition of the species diffusive budget according to its diffusion, premixed and partially premixed combustion contributions.

4 Premixed, diffusion and partially premixed regimes

To delineate between the possible flame structures and combustion regimes, hybrid flamelet equations were discussed in the literature [7, 8, 9]. These equations employ three scalar dissipation rates, namely $\chi_Z = D_Z |\nabla Z|^2$, the mixture fraction dissipation rate, $\chi_{Y_c} = D_c |\nabla Y_c|^2$, the progress of reaction dissipation rate and $\chi_{Z,Y_c} = D_{Zc} \nabla Z \cdot \nabla Y_c$, the cross scalar dissipation rate. Various levels of approximation exist in these hybrid flamelets, in which the evolution of every species mass fraction Y_i is here expressed versus Y_c a non-normalized progress of reaction [10]. The steady unity Lewis and Schmidt numbers case is considered to study the flame topology on the basis of the gradients orientation only. Within this context the balance equation for any species mass fraction Y_i reads [7, 9]:

$$\frac{\partial Y_i}{\partial \tau^*} + \frac{\partial Y_i}{\partial Y_c} = R^{DF} \frac{\partial^2 Y_i}{\partial Z^2} + R^{PF} \frac{\partial^2 Y_i}{\partial Y_c^2} + R^{PPF} \frac{\partial^2 Y_i}{\partial Y_c \partial Z} + \frac{\dot{\omega}_i}{\dot{\omega}_{Y_c}} \tag{2}$$

where the R^i coefficients scale as the inverse of Damkohler numbers: $R^{DF} = \chi_Z/\dot{\omega}_{Y_c}$, $R^{PF} = \chi_c/\dot{\omega}_{Y_c}$, $R^{PPF} = \chi_{Z,c}/\dot{\omega}_{Y_c}$.
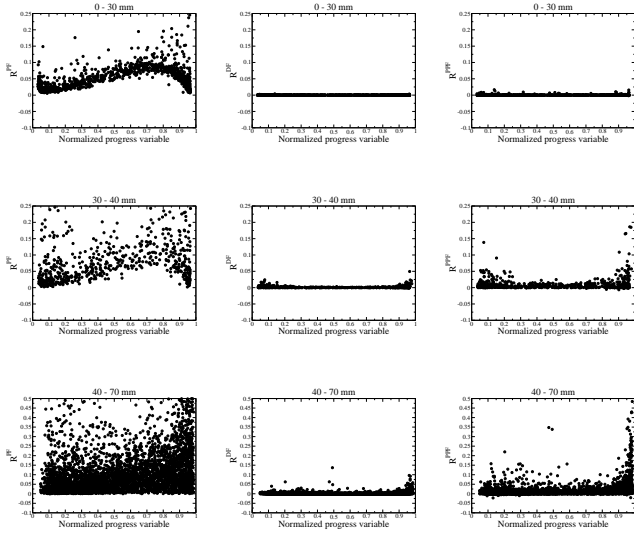
Figure 7: CSWB5 combustion modes. Left: $R^{PF} = \chi_c/\dot{\omega}_{Y_c}$ premixed flamelets. Middle: $R^{DF} = \chi_Z/\dot{\omega}_{Y_c}$ diffusion flamelets. Right: $R^{PPF} = \chi_{Z,c}/\dot{\omega}_{Y_c}$ partially premixed flamelets

Figure 8: CSWB9 combustion modes. Left: $R^{PF} = \chi_c/\dot{\omega}_{Y_c}$ premixed flamelets. Middle: $R^{DF} = \chi_Z/\dot{\omega}_{Y_c}$ diffusion flamelets. Right: $R^{PPF} = \chi_{Z,c}/\dot{\omega}_{Y_c}$ partially premixed flamelets

When $R^{DF} > R^{PPF} > R^{PF}$ diffusion combustion is expected to control the behavior of the reaction zone, for $R^{PF} > R^{PPF} > R^{DF}$ the flame is premixed controlled, other situations were R^{PPF} dominates would correspond to partially premixed cases.

Because of the very weak level of mixture fraction SGS fluctuations, the reaction zones are almost at a fixed equivalence ratio within the sub-grid and these ratios may be studied based on the LES resolved quantities, which are plotted at various locations along the axis of the stratified burner for the two cases in Figure 7 and 8 (not all mesh points are shown). Up to 30 mm only premixed flamelets are observed with equivalence ratios associated with the inner jet value. Therefore R^{PF} is governed largely by the shape of the progress variable source term with some contribution from the local strain proportional to the scalar dissipation rate. From 30 mm - 40 mm where the mixing layer is believed to intersect the flame, some partially premixed flamelets start to appear even though premixed mode is still the dominant one. Finally, between 40 - 70 mm, varying equivalence ratios are encountered by the flame and hence for R^{PF}, points are observed everywhere with no specific trend of evolution which was observed at locations close to the burner (0 - 30 mm), where equivalence ratio was almost fixed. In addition, in this zone of the flame, the number of points exhibiting non-negligible values for R^{PPF} increases. This is more pronounced in the highly stratified case CSWB9. In both cases, the diffusion flame regime is observed to be negligible. This leads us to the conclusion that downstream of this burner, the reaction zones are in fact composed of almost independent collection of premixed flames at various equivalence ratios.

Focussing on the weak partially premixed burning mode observed, R^{PPF} used in Figure 2 is indirectly controlled by the alignment of the flame and mixing vectors which are now discussed.

Stratified flames could be defined as back supported or front supported depending on the alignment of the flame propagation direction with the mixture fraction gradient. In a back supported flame, the direction of propagation is from a rich mixture to a leaner zone and *vice versa*
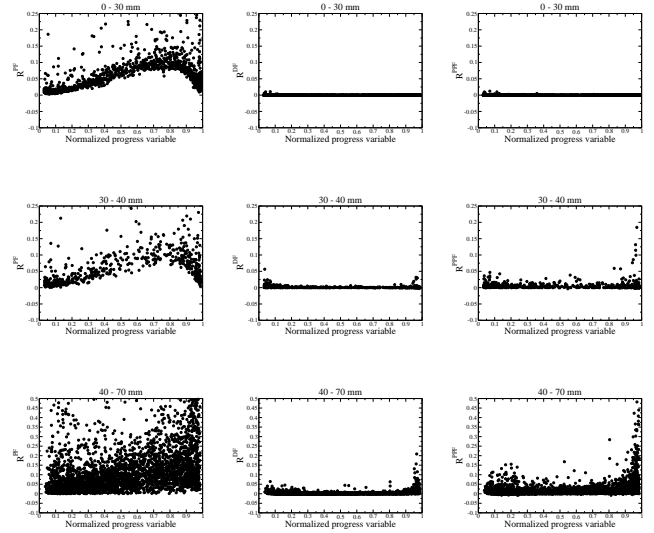
for the front supported flames. Mathematically, we can define the orientation of the flame propagation and the mixture fraction gradient vector to identify these modes as

$$\theta = cos^{-1}\left(\frac{\nabla \widetilde{c} \cdot \nabla \widetilde{Z}}{|\nabla \widetilde{c}||\nabla \widetilde{Z}|}\right) \quad (3)$$

such that $\theta = 0°$ denotes pure back supported flames and $\theta = 180°$ denotes complete front supported combustion. Figure 9 shows the normalized number distribution of the angle, $P(\theta)$ versus θ from an instantaneous data and the time averaged data, both are shown to measure the impact of the resolved LES fluctuations on flame topology.

For the instantaneous case, the more probabilistic value of the angle observed for both CSWB5 and CSWB9 is around 20°, which means that the combustion is predominantly back supported. In these low turbulent flames, this can be inferred also from the mean values; the instantaneous and time averaged data yield almost the same probability trends indeed, with small deviations observed, except in the most turbulent zones at 30 mm and 40 mm where the flame intersects the mixing layer. There, the mean values lead to a slightly wider θ distribution erroneously indicating front supported combustion. At downstream locations, the mean flame starts to align itself to the mixture fraction gradient.

5 Comparison with experiments

The comparison of the axial velocity statistics of LES with the LDA measurements are shown in Figure 10 and 11. As reported in the literature [11], bluff-body flows are known to show asymmetric behavior, also the time averaged fields are not fully axisymmetric especially at locations downstream of 30 mm. Therefore three dimensional time averaged statistics are presented with data obtained either by azimuthal averaging or from a specific plane. The LES data has an overall good agreement with the LDA measurements. It can be seen that the predicted axial velocity in the central recirculation zone
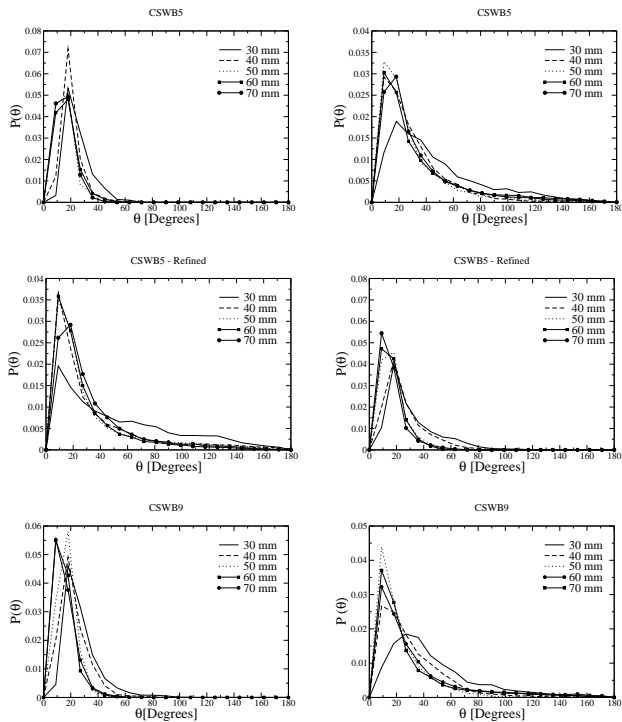
Figure 9: Probability distribution plot of θ as a function of θ conditioned over progress variable $(0.01 < \widetilde{c} < 0.99)$. Left: From instantaneous data. Right: From time averaged data
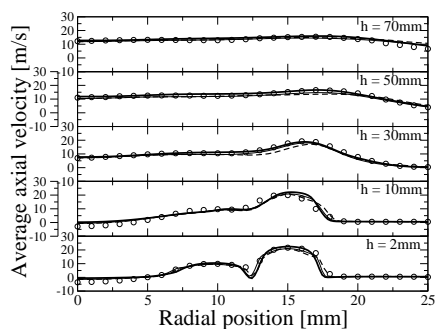
(a)
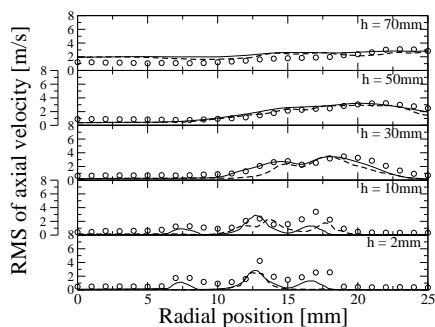
(b)

Figure 10: Axial velocity statistics for CSWB5. Symbols: LDA, LES: – Azimuthally averaging coarse mesh, - - - Single plane coarse mesh, — Azimuthally averaged refined mesh

is however slightly higher than the measurements. A possible explanation for this is the heat transfer to the ceramic bluff body. Since the model does not account for the presence of heat losses, the predicted temperature near the bluff body is higher than the measured temperatures (not shown for brevity). The calculated density is therefore lower, and hence the velocities tend to be higher than in the experiment since air entrainment in the recirculation zone is favor by lower density (less inertia of the gases).

The axial velocity fluctuations in the flame zone (radial locations between 6.35 mm and 10 mm) are under predicted by the coarse mesh (Figure 10b line). The proper level of fluctuations cannot be recovered by adding the SGS contribution, because in this zone due to re-laminarisation effects the sub-grid viscosity is almost zero. Therefore, it is believed that the large filter size of the coarse mesh is responsible for damping of the fluctuations. In the refined mesh simulations (Figure 10b bold-line), the filter size decreases resolving smaller length scales and the right level of fluctuations are recovered emphasizing the need for performing LES on more than a single mesh resolution.

6 Summary

Large Eddy Simulation (LES) of the two stratified non-swirling configurations of the Cambridge swirl burner was performed. This burner exhibits significant re-laminarisation effects in the recirculation zone where the fluctuations present in the cold flow are found to be suppressed in the reacting cases. The LES velocity statistics were found to agree with the LDA measurements.

The analysis of the LES combustion regimes shows that the reaction zones develop under a quite large spectrum of flame topologies from wrinkled flamelets up to thin reaction zones. Motivating the need for a sub-grid scale combustion closure able to dynamically follow the change in regime according to the properties found at a given instant of time in a LES mesh cell.

The study of the reaction zone topology from the equivalence ratio distribution and progress of reaction, shows that due to the much larger scales of stratification compared to the flame thickness, the flame propagates in a quasi-homeogeneous mixture. Moreover, a decomposition of the flame response into premixed, diffusion and partially premixed flamelets is discussed, to conclude that the premixed mode indeed dominates in this burner, with however some partially premixed occurrence further downstream. Finally, the analysis of the orientation of equivalence ratio gradient versus the progress variable one leads to the conclusion that the flame is mostly back supported, *i.e.* the direction of propagation is from a rich mixture to a leaner zone.

Acknowledgements
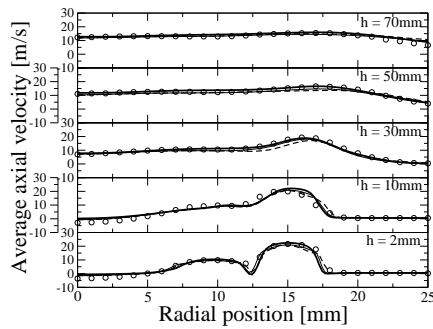
(a)
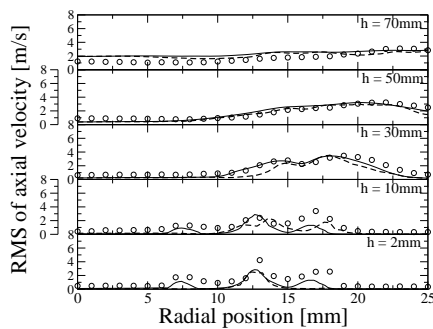
(b)

Figure 11: Axial velocity statistics for CSWB9. Symbols: LDA. Lines: LES. — azimuthal averaging, - - - single plane

References

[1] M. S. Sweeney, S. Hochgreb, M. J. Dunn, and R. S. Barlow, "The structure of turbulent stratified and premixed methane/air flames i: Non-swirling flows," *Combust. Flame*, vol. 159, no. 9, pp. 2896 – 2911, 2012.

[2] M. S. Sweeney, S. Hochgreb, M. J. Dunn, and R. S. Barlow, "A comparative analysis of flame surface density metrics inpremixed and stratified flames," *Proceedings of the Combustion Institute*, vol. 33, no. 1, pp. 1419–1427, 2011.

[3] V. Moureau, P. Domingo, and L. Vervisch, "From large-eddy simulation to direct numerical simulation of a lean premixed swirl flame: Filtered laminar flame-pdf modeling," *Combust. Flame*, vol. 158, no. 7, pp. 1340 – 1357, 2011.

[4] V. Moureau, P. Domingo, and L. Vervisch, "Design of a massively parallel cfd code for complex geometries," *C.R. Mecanique*, vol. 339, no. 2-3, pp. 141–148, 2011.

[5] S. K. Nambully, *Accounting for differential diffusion effects in LES of turbulent combustion using a filtered laminar flame PDF approach. Application to stratified burners.* PhD thesis, National Institute of Applied Sciences Rouen, 2013.

[6] G. Kuenne, A. Ketelheun, and J. Janicka, "Les modeling of premixed combustion using a thickened flame approach coupled with fgm tabulated chemistry," *Combust. Flame*, vol. 158, pp. 1750–1767, 9 2011.

[7] P. Domingo, L. Vervisch, and D. Veynante, "Large-eddy simulation of a lifted methane jet flame in a vitiated coflow," *Combust. Flame*, vol. 152, pp. 415–432, 2 2008.

[8] E. Knudsen and H. Pitsch, "A general flamelet transformation useful for distinguishing between premixed and non-premixed modes of combustion," *Combustion and flame*, vol. 156, no. 3, pp. 678–696, 2009.

[9] P.-D. Nguyen, L. Vervisch, V. Subramanian, and P. Domingo, "Multidimensional flamelet-generated manifolds for partially premixed combustion," *Combust. Flame*, vol. 157, pp. 43–61, 1 2010.

[10] G. Lodier, L. Vervisch, V. Moureau, and P. Domingo, "Composition-space premixed flamelet solution with differential diffusion for in situ flamelet-generated manifolds," *Combust. Flame*, vol. 158, pp. 2009–2016, 10 2011.

[11] C. D. Taglia, L. Blum, J. Gass, Y. Ventikos, and D. Poulikakos, "Numerical and experimental investigation of an annular jet flow with large blockage," *Journal of Fluids Engineering*, vol. 126, no. 3, pp. 375–384, 2004.

DETAILED CHARACTERIZATION OF FLAME-WALL INTERACTIONS USING LASER SPECTROSCOPY

M. Mann, C. Jainski, A. Dreizler and B. Böhm

Fachgebiet Energie- und Kraftwerkstechnik, Technische Universität Darmstadt, Petersenstr. 32, 64287 Darmstadt, Germany
Corresponding author: bboehm@ekt.tu-darmstadt.de

Abstract

In enclosed combustors processes occurring at the wall are a mayor cause for emissions such as carbon monoxide (CO) and unburned hydrocarbons. The understanding of flame-wall interactions is therefore of great interest. Experiments were performed in an impinging jet burner in premixed methane/air flames. The complexity of the setup was increased step by step, starting from laminar stationary flames stabilized at a wall to transient flames which are ignited at the nozzle exit and propagate successively towards the wall. Parameter variations were performed including laminar and turbulent flows as well as equivalence ratios of 0.83-1.2. Measurements were performed in the vicinity of the wall using laser spectroscopy. In the gas phase CO concentration was measured simultaneously with temperature using two-photon laser-induced fluorescence (LIF) and coherent anti-Stokes Raman spectroscopy (CARS).

1 Introduction

Flame-wall interactions play a crucial role in enclosed combustion systems. A majority of pollutant emissions such as unburned hydrocarbons (UHC) and CO originate from the vicinity of walls [1]. With increasing power densities for improved fuel efficiencies the influence of walls within combustion systems will further increase. This "downsizing" strategy leads for example to highly boosted engines [2] where the surface to volume ratio increases further and emphasize the importance of understanding the processes close to walls.

Enclosed combustors are characterized by a high gas phase temperature, where the chemically bounded energy of the fuel is converted into thermal energy surrounded by walls at comparably low temperatures. This temperature gradient leads to heat losses over the wall reducing the combustors efficiency. The lower temperatures close to the wall slow down chemical reactions and finally quench the flame. The reaction is interrupted and intermediate species as CO or UHC cannot fully oxidize. This leads to higher emissions as well as a further reduction of combustion efficiency. These processes at the wall, here specified as "flame-wall interactions" are characterized by small time and length scales. They are highly transient and occur in very thin layers at the wall, typically in sub-millimeter scales in realistic combustion devices. Experiments as well as simulations are challenging due to these small scales.

In the context of flame-wall interactions measurements of the flame quenching distance were carried out for side-

wall (the flame propagates along a wall) and head-on quenching (the flame propagates onto a wall) configurations using probing or luminescence techniques (see for example [3]). Flame quenching was found to be linked to high peak levels of heat flux caused by very small distances between flame and wall in the quenching layer. An overview on experiments performed in stationary flames burning against walls where the heat flux is constant is presented by [4].

Laser based measurement techniques are well established in combustion research [5]. Compared to traditional techniques laser light is non-intrusive and able to capture highly transient processes with an outstanding spatial resolution. In the context of flame-wall interactions only few experiments are reported. A mayor problem is spuriously scattered light off the wall which interferes with the desired signal. The use of coherent and spectrally shifted spectroscopic laser based methods reduces problems of scattered light for measuring locations close to solid surfaces. Only few studies were reported on flame-wall interactions using spectroscopic methods. The temperature boundary layer within an IC engine was investigated by Lucht et al. [6] using coherent anti-Stokes Raman spectroscopy (CARS). More recently Fuyuto et al. [7] captured mean temperatures and intermediate species concentrations in a side-wall quenching configuration using LIF techniques as close as 200 μm to the surface.

Temperature and CO are meaningful quantities to characterize flame-wall interactions as the first affects all chemical reaction rates and the latter is beside being a pollutant an indicator of the completeness of the combustion process. CARS thermometry was used in this work to measure temperature because it is expected to provide the most accurate and precise measurements at flame temperature and it is a calibration free method. Two-photon laser induced fluorescence (LIF) was used to capture CO concentration due to its sensitivity regarding lowest CO concentrations. Additionally the large spectral shift between excitation and the fluorescence signal helps rejecting stray light from the walls. Flame-wall interactions are also a great challenge for numerical simulations. The widely used wall models are often not able to characterize the complex interaction of fluid mechanics and chemistry in the near wall region.

Different strategies are used to handle the wall-boundary conditions in simulations. [8] for example includes enthalpy losses at the walls and applies a special treatment of chemical reaction rates in order to model the processes of flame-wall interaction. Direct numerical simulations can help to understand the underlying phenomena in generic configurations [9, 10] but are lim-

ited to simple configurations due to extensive required computational power.

The present work aims for a better understanding of the underlying physical processes of flame-wall interactions and for providing data for model development and the validation of numerical simulations. In previous work results of a stationary flame-wall interaction were presented [11] including temperature, CO and heat flux measurements of a laminar flame. Additionally a detailed characterization of the burners turbulent in-nozzle flow using turbulence grids was performed by [12] for validation purposes. In this work CO concentration was measured simultaneously with temperature using two-photon laser-induced fluorescence (LIF) and coherent anti-Stokes Raman spectroscopy (CARS), respectively. The complexity of the flame-wall interaction was increased stepwise from a laminar to a turbulent stationary flame and was extended by a transient flame which represents a head-on quenching scenario.

2   Experimental setup

2.1   Burner setup

The measurements were performed in an impinging jet burner. Figure 1 shows a cross-section of the burner. The burner consists of a vertically aligned Morel nozzle with a contraction ratio of 9:1. The nozzle, 30 mm in diameter, is placed 32 mm below a curved wall. For the turbulent flows only a perforated plate with hexagonally arranged holes, 4 mm in diameter, was inserted 50 mm upstream of the nozzles exit [12]. The blockage ratio of the perforated plate was 45 %. The premixed methane/air jet was surrounded by a nitrogen coflow that shielded the flame from ambient air. The coflow velocity was set to 20 % of the nozzle's bulk velocity. The horizontally aligned wall is 120 mm in diameter, made of stainless steel and is water-cooled. For improved optical accessibility, the wall surface has a convex curvature, corresponding to a segment of a 600 mm diameter sphere. This allows bringing focused laser beams closer to the wall and reduces vignetting effects for the detection system. Thus laser based measurements as close as 50 μm to the wall were possible.
Premixed methane/air flames with equivalence ratios of 0.83, 1 and 1.2 were investigated. The Reynolds number based on the nozzle exit diameter was set to 2500 and 5000, respectively. The base case in this work is characterized by an equivalence ratio of $\phi = 1$ and Re $= 5000$ without the turbulence grid (TG). To increase turbulence levels a TG was inserted for Re $= 5000$. Stationary burning as well as transient flames were established. For the transient flames the mixture was ignited on the centerline 5 mm above the nozzle by a focused Nd:YAG laser beam.

2.2   CARS thermometry

Nanosecond ro-vibrational coherent anti-Stokes Raman spectroscopy (CARS) of N_2 was used for instantaneous gas-phase temperature measurements. A frequency-doubled 10 Hz Nd-YAG laser (Quanta Ray PIV 400-10) delivered light at 532 nm for the pump and probe beam and to pump a modeless dye laser. A mixture of Rhodamine 610 and Rhodamine 640 was used to generate the broadband Stokes beam at around 607 nm. The pulse energy of the probe and the pump beam were set to 16 mJ and the Stokes beam to 10 mJ. A planar BOXCARS
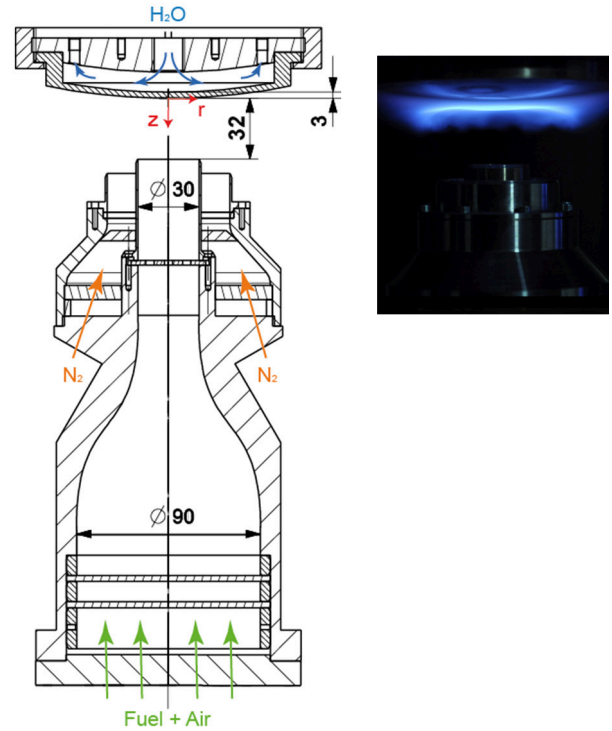
Figure 1: Sketch of the impinging jet burner. All quantities are given in mm. The photograph of flame luminosity illustrates the stationary burning flame

phase matching parallel to the surface was realized using a pair of 300 mm lenses. The corresponding phase matching angles are 2° (pump and probe beam) and 2.3° (stokes beam) in respect of the beam-wise direction. The resulting probe volume is 65 μm in diameter and 1.5 mm in length.

The blue shifted CARS signal was directed into a spectrometer (SPEX Industries SPEX 1707) equipped with a 2400 lines/mm grating and recorded by a CCD camera (Princeton Instruments Pixis 400). The CCD was operated at 20 Hz in order to provide background images in-between the laser shots. The background corrected spectra are normalized by the non-resonant signal of pure methane and fitted with the CARSFT algorithm [13] to a theoretical spectrum. To increase the dynamic range optimized sets of neutral density filters were used in front of the spectrometer depending on the local temperature range in the probe volume.

2.3   CO LIF spectroscopy

Two-photon LIF was used to capture the instantaneous CO concentration. A frequency doubled Nd:YAG laser (Quanta-Ray GCR-4) was used to pump a dye laser (Sirah Precision Scan) operating with Pyridine 1 solved in ethanol. The laser output (690 nm) was frequency tripled to 230.1 nm to excite the Hopfield-Birge bands $B^1 \sum^+ (v' = 0) \leftarrow\leftarrow X^1 \sum^+ (v'' = 0)$ by the absorption of two photons. Pulse energy was in the order of 1.5-2.2 mJ. A spherical 300 mm lens was used to focus the laser beam to 200 μm in the probe volume.

The resulting fluorescence of the Angström-Bands $B^1 \sum^+ (v' = 0) \rightarrow A^1 \prod (v'' = 1)$ was then recorded by an intensified CCD camera (Princeton Instruments PI-MAX 2) operated at 20 Hz. It was equipped with a combination of a 100/f2 macroscopic lens (Carl Zeiss Makro Planar T* 100/2) and an achromatic lens (f = 160). To
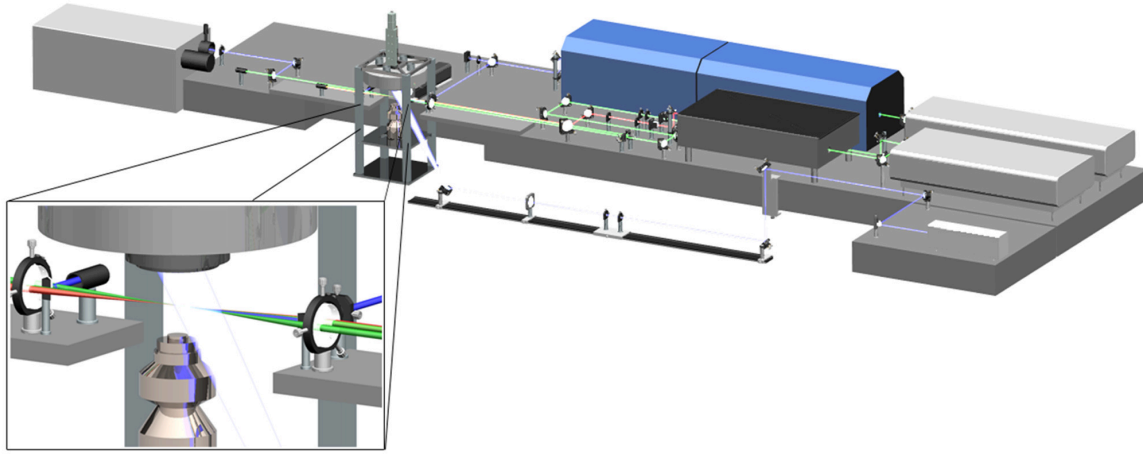
Figure 2: Combined CARS and CO-LIF setup. The inserted zoom shows the probe volume formed by the individual laser beams in respect to the burner

reduce crosstalk of the C_2 Swan bands a bandpass filter was used centered at 485 ± 5 nm. Additionally the camera gate time was reduced to 50 ns to reduce the influence of flame luminosity. LIF signals were transformed to CO concentrations by a calibration procedure. To take into account the temperature dependencies of the LIF signal a heated jet with a CO-N_2 mixture was used for temperatures up to 1000 K and a laminar flat flame with well-known CO concentrations up to 2200 K. The temperature was taken from the simultaneous CARS measurements. Near wall measurements as close as 100 μm to the wall were possible without significant interference from the wall by filtering wall hits of the laser beam. The LIF signal is additionally affected by vignetting effects of the wall. A geometric look-up table was generated with correction factors as a function of the measurement location. Figure 2 shows the experimental setup for CARS and CO-LIF. A time delay of 140 ns between both systems is chosen to avoid a crosstalk between both signals. The probe volumes of both, CO-LIF and CARS, were carefully overlapped by the use of a 100 μm pinhole and coherent signal generated by a thin glass plate.

3 Results and Discussion

3.1 Stationary flame

Figure 3 shows profiles of averaged temperature and CO along the centerline together for the stationary flame. As shown in [11] gas phase temperatures can be extrapolated to the surface temperatures, which are in the region of 320-360 K. Each single point is an average of 400 instantaneous shots. For the base case no turbulence grid was used. The Reynolds number was set to 5000 and the mixture was stoichiometric. The flame stabilizes at a distance of ≈ 5 mm from the wall. This is observed in the steep temperature rise accompanied by a sudden increase of CO, which is generated in the flame forming a maximum at $z = 4.8$ mm. CO is continuously consumed in the hot flame region and reaches nearly zero at the wall. With decreasing CO level temperature continues to increase further until it reaches maximum temperature of 2100 K at a distance of 3 mm from the wall. Further to the wall a steep temperature decrease is observed with a temperature of ≈ 550 K at $z = 0.1$ mm. The shape of the temperature profiles at the wall does not change for the lean (0.83) and rich flame (1.2) up to a distance of $\approx$
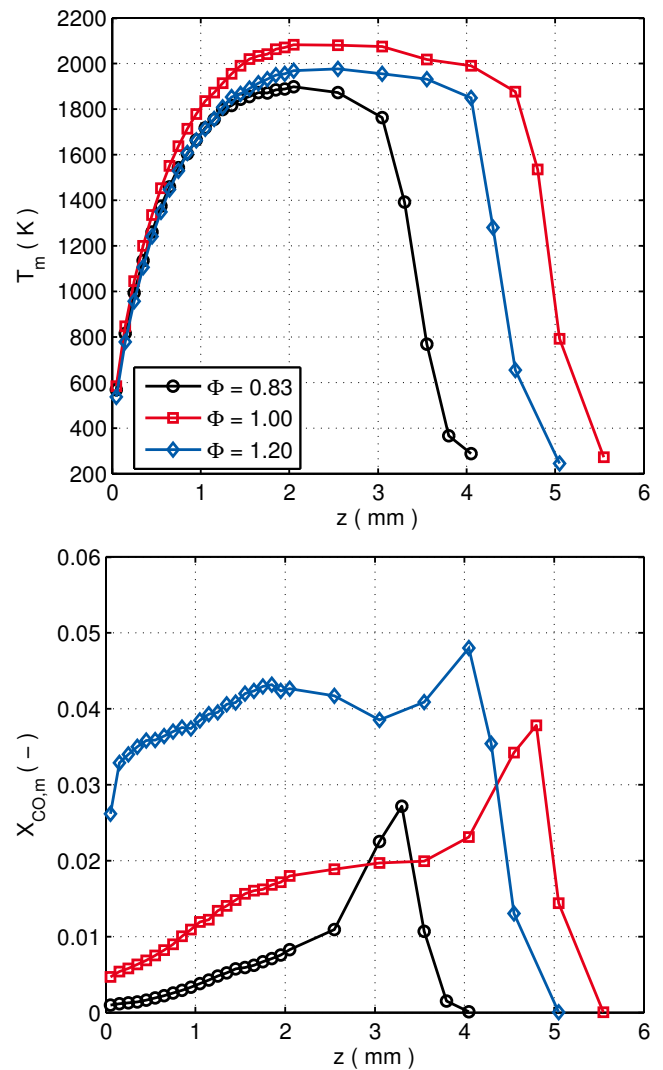
Figure 3: Mean temperature (left) and CO (right) for the stationary flame at Re = 5000 and no TG
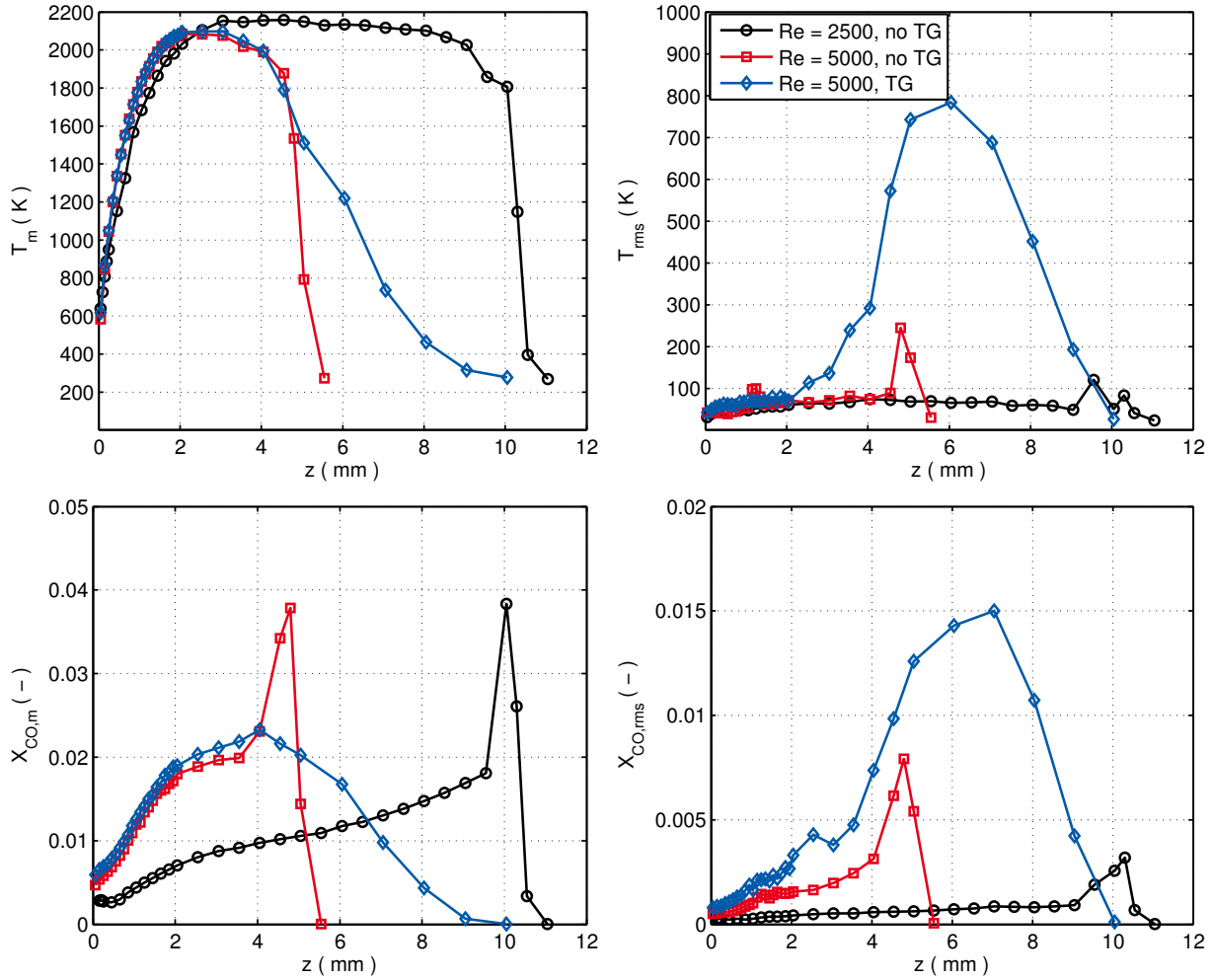
Figure 4: Axial profiles of mean and fluctuations of temperature (left) and CO (right) for the stationary flame for $\phi=1$

2 mm whereas the level of maximum temperature varies. The location of flame stabilization in contrast shifts significantly for the lean flame to z = 3.5 mm and less for the rich flame to z = 4.5 mm. This is in good agreement with the flame speed behavior having its maximum close to stoichiometry on the fuel rich side. The peak CO level within the flame region increases with C/O ratio. This flame generated CO is subsequently consumed in the post-flame region of the lean and the stoichiometric flame but remains at high levels (0.04 mole fraction) for the rich flame due to the deficiency of oxygen.

Figure 4 shows temperature and CO profiles of the stoichiometric flame at a Reynolds number of 5000 with and without (base case) the TG and at 2500 without the TG. For the lower Reynolds number the flow velocity is reduced by a factor of 2. As a consequence the flame stabilizes further away from the wall from 5 mm for Re = 5000 to 10.5 mm for Re = 2500. With the turbulence grid (Re = 5000) the initial turbulence level at the nozzle exit is $\approx$ 10 %. Due to stochastic vortex-flame interactions the flame is distorted and the flame's location fluctuates. As a consequence the average temperature and CO profiles are much broader and the distinct CO peak is washed out. This is also highlighted by the rms values which have a narrow distribution for the base case (Re = 5000, no TG) confirming a quite stationary and laminar flame with peak rms values of 250 K and 0.0075 for CO compared to 800 K and 0.015 for Re = 5000 with the turbulence grid. Further to the wall the influence of turbulence decays rapidly due to increased viscosity within the hot gas regions. In the thermal boundary

layer, with an approximate thickness of 2 mm, no difference is observed for the average temperature. The CO levels are higher for the Re = 5000 cases which might be a consequence of shorter residence times due to the thinner high temperature region.

Figure 5 shows the instantaneous and simultaneously taken temperature and CO mole fraction measurements represented by a scatter plot. Data of the base case are shown together with the result of a 1D simulation of a stagnation-stabilized flame performed with Cantera [14] using the GRI mechanism 3.0. The individual data points can be clustered into three distinct branches: The first shows an almost linear increase of CO with temperature which correlates with the main reaction zone of the flame (this corresponds to the maximum temperature and CO gradients in Figure 3). Maximum CO concentrations are found at $\approx$ 1700 K. The second branch represents the post flame region where temperature continues to increase until maxima are reached close to adiabatic flame temperature. The CO concentration decreases rapidly as it continues to oxidize to form CO_2. The third branch is characterized by the influence of the wall. The enthalpy loss from the fluid to the wall reduces the gas phase temperature. CO oxidation slows down and a constant CO concentration of 0.007 remains below $\approx$ 600 K.

3.2 Transient flame

Figure 6 shows a sequence of a transient flame visualized by chemiluminescence. The flame is ignited by a focused
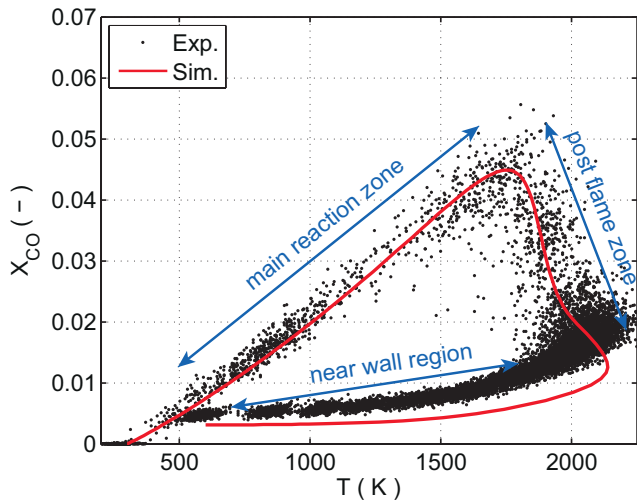
Figure 5: CO mole fraction versus temperature for Re=5000, no TG and $\phi = 1$ (base case) together with a 1D calculation obtained from Cantera

laser on the centerline 5 mm downstream of the nozzle exit. The flame propagates with the flow towards the wall. In the vicinity of the wall the flame extinguishes at less than 0.5 mm which corresponds to the typical quenching distance of such a flame. The flame then travels back upstream until the corresponding stationary flame is established (see Figure 3). This represents a typical head-on quenching event were the flame directly interacts with the wall as it would occur in IC engines for example. This is different to the stationary flames where a region of exhaust gas acts as a buffer between the flame and the wall.

Figure 7 shows averaged temporal temperature and corresponding rms values obtained from six axial positions along the centerline. Each point is an average of 200 individual events. The time axis is set to zero when the flame starts to quench at the wall. This is defined when the maximum temperature arises at the closest measurement point at the wall ($z = 0.1$ mm). For the base case with $\phi = 1$ the flame reaches the measurement point at $z = 1.7$ mm around 4 ms before start of quenching. As the flame continues to propagate towards the wall the temperature rises up to 2150 K which is close to the adiabatic flame temperature of 2220 K. For the closer measurement points the impact of the wall can be clearly seen by the reduced peak temperatures which are shifted to earlier times before quenching. At $z = 0.1$ mm peak temperature is already reduced by a factor of two. This temperature drop observed after quenching is supported by other studies [15, 16] and is a consequence of maximum heat fluxes to the wall. The thickness and shape of the thermal layer changes significantly from the stationary to the transient case (see Figure 3). At the wall where the flame quenches, peak temperatures are a factor of two higher for the transient compared to the stationary case. Within the thermal layer the temperature fluctuations are quite similar for all observed locations with peak levels of 200-250 K.

4 Conclusions

In this work simultaneous temperature and CO measurements were performed within an impinging jet burner using CARS and CO-LIF, respectively. Two different flame-wall interaction scenarios were investigated: A sta-
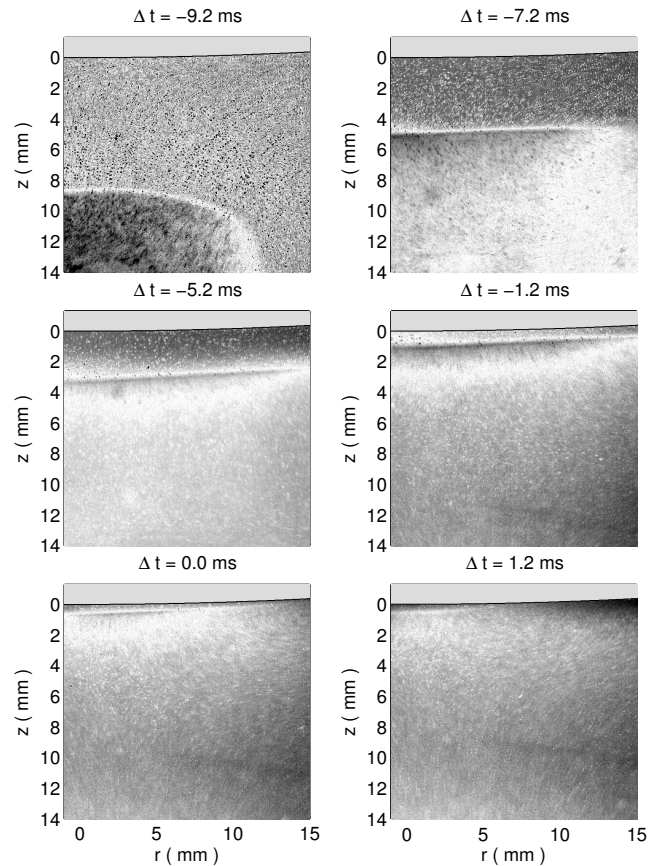
Figure 6: Sequence of chemiluminescence images showing the transient flame (Re=5000, $\phi = 1$, no TG) propagating towards the wall

tionary flame stabilized close to a wall and a transient flame propagating towards a wall. The laser based spectroscopic measurements were performed as close as 100 μm to the wall resolving the quenching processes at the wall. The enthalpy loss to the wall decreased the peak temperature of the flame front close to the surface. For the stationary flame its location was found to depend on the equivalence ratio as well as turbulence level whereas the temperature profiles in the boundary layer collapsed into a single curve. CO concentrations in the boundary layer in contrast depended on the equivalence ratio and Reynolds number. For the stationary flame a burned gas buffer is located between the flame and the wall. This is different for the transient flame which propagates to the wall and interacts therefore directly with the wall. First results were shown which will be used for further analysis as for example the determination of flame quenching distances and heat fluxes occurring at the instant of flame quenching.

Acknowledgements

References

[1] A.C. Alkidas, Progress in Energy and Combustion Science 25 (1999) 253-273.

[2] R. Golloch, Downsizing bei Verbrennungsmotoren, Springer-Verlag, Berlin Heidelberg, 2005.

[3] M. Bellenoue, T. Kageyama, S.A. Labuda, J. Sotton, Experimental Thermal and Fluid Science 27 (2002) 323-331.

[4] S. Chander, A. Ray, Energy Conversion and Management 46 (2005) 2803-2837.

[5] K. Kohse-Höinghaus, J.B. Jeffries, Applied Combustion Diagnostics, Taylor & Francis, New York, 2002.

[6] R.P. Lucht, M. Maris, SAE Technical Paper (1987).

[7] T. Fuyuto, H. Kronemayer, B. Lewerich, J. Brübach, T. Fujikawa, K. Akihama, T. Dreier, C. Schulz, Exp Fluids 49 (2010) 783-795.

[8] M. Chauvy, B Delhom, J. Reveillon, F. Demoulin, Flow Turbulence Combust 84 (2010) 369-396.

[9] G. Bruneaux, T. Poinsot, J.H. Ferziger, Journal of Fluid Mechanics 349 (1997) 191-219.

[10] A. Gruber, R. Sankaran, E.R. Hawkes, J.H. Chen, J. Fluid Mech. 658 (2010) 5-32.

[11] A. Singh, M. Mann, T. Kissel, J. Brübach, A. Dreizler, Flow Turbulence Combust 90 (2013) 723-739.

[12] B. Böhm, O. Stein, A. Kempf, A. Dreizler, Flow Turbulence Combust 85 (2010) 73-93.

[13] G. Clark, R.L. Farrow, Sandia National Laboratories, Livermore, CA 94550 (1990).

[14] D.G. Goodwin, Cantera: `http://code.google.com/p/cantera/`.

[15] J.H. Lu, O.A. Ezekoye, R. Greif, R.F. Sawyer, Proc. Comb. Inst. 23 (1991) 441-446.

[16] C. Hasse, M. Bollig, N. Peters, H.A. Dwyer, Combustion and Flame 122 (2000) 117-129.
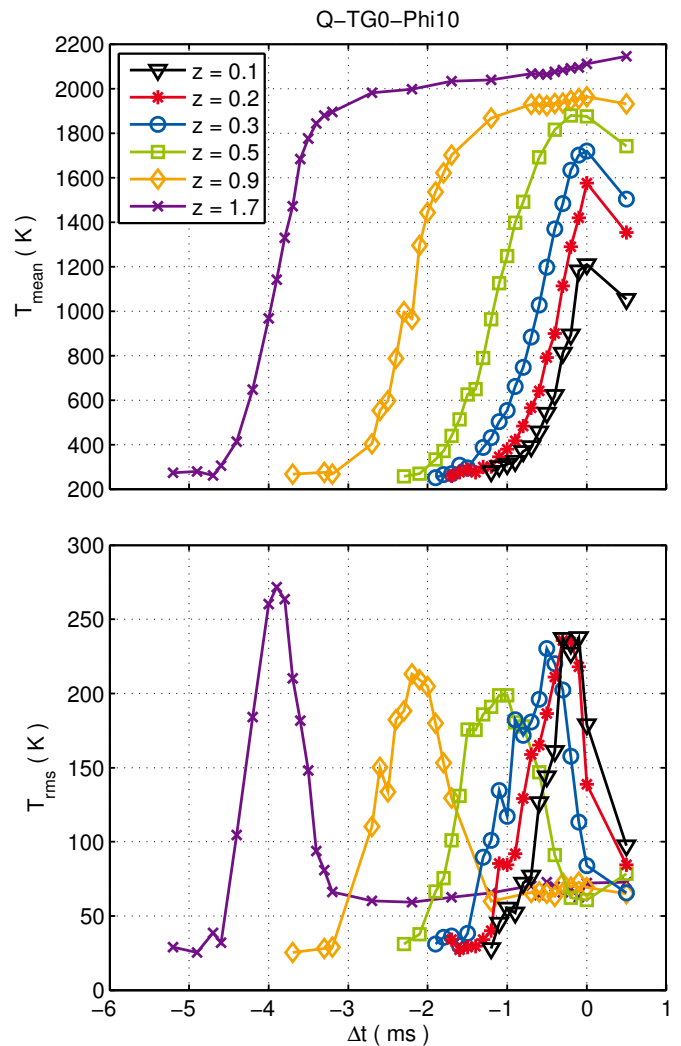
Figure 7: Temporal evolution of mean temperature and fluctuations at the centerline for the transient flame (Re=5000, ϕ= 1, no TG)

Influence of Injector Diameter (0.2-1.2 mm Range) On Diesel Spray Combustion: Measurements and CFD Simulations

M. Bolla[1], Y. M. Wright[1], B. von Rotz[2] and K. Boulouchos[1]

[1] *Swiss Federal Institute of Technology, Zurich, Switzerland*
[2] *Wärtsilä Switzerland Ltd., Switzerland*

Abstract

In this study, the influence of injector diameter on the combustion of Diesel sprays in an optically accessible combustion chamber of marine engine dimensions and conditions has been investigated experimentally as well as numerically. Five different orifice diameters ranging between 0.2 and 1.2 mm have been considered at two different ambient temperatures: a "cold" case with 800 K and a warm case with 900 K, resulting in a total of ten different test conditions.

In the experiment, the reactive spray flames were characterised by means of high-speed OH* chemiluminescence imaging. The measurements revealed a weak impact of the injector diameter on ignition delay (ID) time and flame lift-off length (LOL) whereas the influence of ambient temperature was found to be more pronounced, consistent with former studies in the literature for smaller orifice diameters.

Computational fluid dynamics (CFD) simulations were performed using the Conditional Moment Closure (CMC) combustion model and the numerical results have been validated with experimental data by means of ignition delay time, flame lift-off length and spatial evolution of flame region. The simulation was capable to reproduce ID very well while the calculated LOL were underestimated. The early flame development after ignition was reasonably well captured. Following this validation, the influence of the orifice diameter on the ignition behaviour and quasi-steady spray characteristics has been further explored numerically. Overall, CMC was found to offer a promising framework also for the simulation of sprays from nozzle orifices in the millimeter range, relevant for large two-stroke marine Diesel engines.

1   Introduction

Due to their unrivalled efficiency and reliability, two-stroke marine Diesel engines largely dominate propulsion of seaborne merchant freight transport. The immense power requirements for these prime movers lead to combustion chamber volumes of the order of cubic metres. The associated strokes of several metres lead to engine speeds well below 100 RPM; as a consequence, the intermittent combustion process duration is of the order of tens of milliseconds. These scales bring about additional complications to the existing challenges concerning the numerical description of spray combustion which include turbulence modeling; atomization and secondary break-up processes of high pressure liquid fuel jets; evaporation and mixture formation followed by autoignition and combustion of the complex hydrocarbons fuels, characterized by typically hundreds of species and thousands of reactions [1].

Given the scales of these combustion systems and the high Reynolds numbers it becomes evident that full resolution of the entire turbulence spectrum is way beyond the scope of contemporary computers. Consequently, turbulence models are widely employed for engineering purposes for such systems. The adoption thereof leads to well-known closure problems, especially in the case of reacting flows where models are needed due to the strong non-linearity of the chemi-cal source terms. In addition, the interaction of the oxidation kinetics with the turbulent flow field must be considered since the time and length scales of these processes may overlap [2]. Many different concepts to address these challenges have hence been developed which range from characteristic time scale approaches [3], coherent flame model extensions [4], methods using transported probability density functions (PDF) [5] as well as concepts employing presumed PDFs, e.g. flamelet models [6]. The Conditional Moment Closure (CMC) model [7] used in this investigations is also among the latter category and has seen successful application to various auto-igniting turbulent flow configurations as reviewed in [8]. Concerning spray combustion at engine relevant conditions, CMC has been validated for a number of generic test rigs [9,10,11,12,13,14,15] as well as in Diesel engines [16,17,18] however at considerably smaller dimensions and time scales than in marine engines.

Concerning two-phase flow modelling, Lagrangian tracking of droplet parcels is most often employed which is fully two-way coupled to an Eulerian treatment of the gas phase. The models in use today have been developed by means of experimental data from systems with considerably smaller dimensions. While sensitivity of the predictions to grid resolution is widely acknowledged [19,20,21]; these models have nonetheless seen successful application also to marine engine sprays given careful consideration of their resolution requirements as shown at non-reacting conditions in [22]. First reactive calculations using CMC for Diesel sprays in the
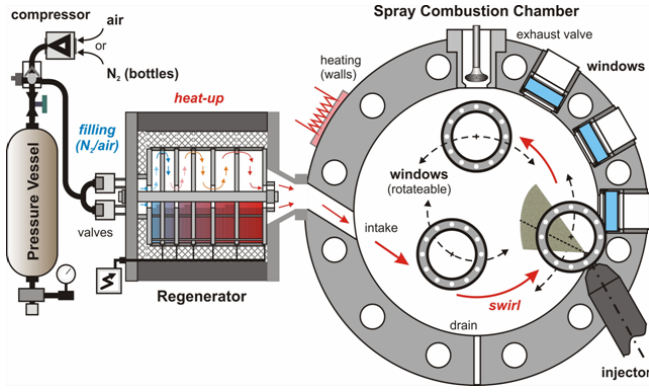
Figure 1: Schematic sketch of working principle of the marine spray combustion chamber (adopted from [29])

marine engine reference experiment have been reported in [23], demonstrating that the methodology is capable of accurate predictions of ignition delay and location and flame lift-off lengths trends for a broad range of temperatures, using validation data from [24]. These investigations were performed for a single nominal nozzle diameter of 0.875 mm, representative of a typical marine fuel injector. At these dimensions, the influence of the nozzle orifice diameter is largely unexplored, while experimental findings for diameters typical to passenger car and heavy-duty injectors up to 0.363 mm have been reported in [25]. This study hence seeks to complement previous findings by extending this range to marine engine fuel injector diameters up to 1.2 mm.

2 Experimental setup

The experimental data used for model validation purposes later on stems from a large two-stroke marine Diesel engine reference experiment installed at Wärtsilä Switzerland for which documentation is given in [26,27,28]. The Spray Combustion Chamber (SCC) is an optically accessible disk shaped chamber of 500 mm diameter and 150 mm height. Fuel is injected from the periphery into swirling hot air or nitrogen at high pressure reproducing conditions typical of large two-stroke Diesel engines. Figure 1 provides a schematic sketch of the SCC working principle: air fed by a pressure vessels flows through an electrically heated regenerator and enters the disk-shaped combustion chamber via the tilted intake that generates the swirling motion. The velocity thereof has been characterized by Laser Doppler Velocimetry (LDV) as reported in [30]: the swirl velocity magnitude at start of injection (SOI) at a radial distance of 200 mm from the chamber centre is typically 20 m/s.

The spray has been characterized under non-reactive conditions and non- and evaporating conditions by means of shadow imaging as reported in [28]. The flame region was detected by high speed OH* chemiluminescence imaging for which further documentation can be found in [24]. In the present study ten different test cases have been considered which are summarized in Table 1. The variations include five different nozzle orifice diameters at two gas temperatures, namely a "cold" case with 800 K and a hotter case at 900 K. Gas temperature and pressure were varied simultaneously to keep the gas density constant in order to minimize two-phase related

momentum transfer effects. This ensures similar spray morphology evolutions at the two temperature levels, although small differences in the evaporation due to the different temperatures are inevitable. The injector is of the co-axial type and has one single orifice; a constant injection duration of roughly 25 ms has been used for all diameters. Depending on the nozzle orifice diameter, the fuel pressure pipe diameter (connecting the common rail to the fuel injector) and the injection pressure (between 650 and 1200 bar) have been varied simultaneously in order to achieve similar pressure drop across the injector tip (pressure is measured at the injector body upstream of the needle and in the combustion chamber). It results a constant fuel injection velocity at the exit of the nozzle (approx. 350 m/s) and a quadratic increase of the mass flow rate with an increase in orifice diameter. All measurements have been carried out with light Diesel fuel oil, for which fuel properties are described in [28], although the test rig can also readily be operated with heavy fuel oil (HFO).

3 Numerical setup

Numerical simulations have been carried using the widely adopted commercial CFD solver Star-CD [31] coupled with a Conditional Moment Closure combustion model discussed below. The computational domain is illustrated in Figure 2 where the red arrow represents the injector location and the nominal spray axis. The entire CFD mesh consists of 1.25 million cells. In the combustion chamber a hexahedral mesh is employed and the region relevant for the spray has been locally refined as illustrated by the green block. The first 300 mm axially and 50 mm radially from their injector, has a perfectly hexahedral grid of 2 mm edge length. Furthermore, the first 150 mm axially and 25 mm radially have been refined to 1 mm cell size. A grid sensitivity study has been carried out in [22] for non-reactive simulations where the spray penetration length and cone angle have been validated for a broad range of conditions, including variations in ambient density and temperature. Flow field initialization (temperature, pressure, velocity, turbulent kinetic energy and turbulence dissipation rate) at start of injection (SOI) are obtained from previous simulations [30,32].

The numerical methodology follows former work presented in [23] for the current experimental facility. Reynolds-averaged Navier-Stokes (RANS) model equations are solved. Turbulence is closed using the $k - \epsilon$ RNG model with default model constants and the standard wall-function formulation is used at solid

Table 1: List of test cases considered

Case	Nozzle diameter d_0 [mm]	Gas temperature [K]	Gas pressure [bar]	Gas density [kg/m^3]
1	0.2	800	80	33
2	0.2	900	90	33
3	0.3	800	80	33
4	0.3	900	90	33
5	0.6	800	80	33
6	0.6	900	90	33
7	0.875	800	80	33
8	0.875	900	90	33
9	1.2	800	80	33
10	1.2	900	90	33
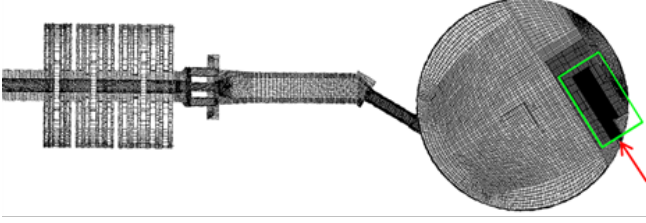
Figure 2: Numerical domain of the Marine Spray Combustion Chamber consisting of inlet (left), regenerator and flange (middle) and combustion chamber (circle). The arrow indicates the location and direction of fuel injector. The green region represents the refined region of interest

walls, where a constant temperature boundary condition ($T_{wall} = 453K$) has been applied.

Spray modeling is by means of a Lagrangian-Eulerian approach, where the primary and secondary break-up are treated following [33] and [34], respectively. n-Dodecane has been used to represent the liquid thermo-physical fuel properties of the Diesel fuel used in the experiment. As no time resolved mass flow rates for the fuel injection were available, the simulation injection rate profile has been estimated from the pres-sure difference across the injector based on pressure measurements in the injector body upstream of the needle seat and in the combustion chamber.

The CFD solver has been coupled with an elliptic first order CMC combustion model which belongs to the presumed PDF methods. As is common practice in non-premixed combustion, the gas-phase mixture fraction is used as the conditioning quantity. The derivation of the governing equations has been discussed in detail e.g. in [7] and not repeated here. Equations are solved conditionally on mixture fraction for chemical species and temperature. Assuming high Reynolds number and unity Lewis number, the following set of equation for conditional temperature Eq. (1) and species mass fraction Eq. (2) are obtained, where Q_T and Q_α are the conditional expectations of the temperature

$$\frac{\partial Q_T}{\partial t} + \langle u_i|\eta\rangle \frac{\partial Q_T}{\partial x_i} = \langle N|\eta\rangle \frac{\partial^2 Q_T}{\partial \eta^2}$$

$$+\langle N|\eta\rangle \left[\frac{1}{\langle c_p|\eta\rangle} \left(\frac{\partial \langle c_p|\eta\rangle}{\partial \eta} + \sum_{\alpha=1}^{N} \langle c_{p,\alpha}|\eta\rangle \frac{\partial Q_\alpha}{\partial \eta} \right) \right] \frac{\partial Q_T}{\partial \eta}$$

$$-\frac{1}{\bar{\rho}\tilde{P}(\eta)} \frac{\partial}{\partial x_i}[\langle u_i''T''|\eta\rangle]\bar{\rho}\tilde{P}(\eta)]$$

$$+\frac{1}{\langle c_p|\eta\rangle} \left\langle \frac{1}{\rho}\frac{\partial P}{\partial t}|\eta \right\rangle + \frac{\langle w_H|\eta\rangle}{\langle \rho|\eta\rangle\langle c_p|\eta\rangle}$$
(1)

and the $\alpha - th$ species mass fraction:

$$\frac{\partial Q_\alpha}{\partial t} + \langle u_i|\eta\rangle \frac{\partial Q_\alpha}{\partial x_i} = \langle N|\eta\rangle \frac{\partial^2 Q_\alpha}{\partial \eta^2}$$

$$-\frac{1}{\bar{\rho}\tilde{P}(\eta)} \frac{\partial}{\partial x_i}[\langle \rho u_i''Y_\alpha''|\eta\rangle]\tilde{P}(\eta)] + \langle w_\alpha|\eta\rangle$$
(2)

The unclosed terms in the CMC equations are modeled using common practice: a linear correlation has been adopted for the conditional velocities $\langle u_i|\eta\rangle$, the gradient flux hypothesis is assumed for the conditional turbulent
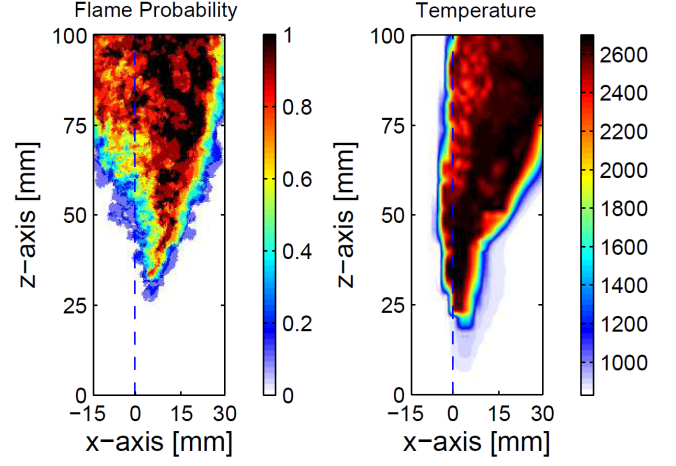
Figure 3: Definition of flame region: experimental flame probability (left) and simulated line-of-sight maximal temperature (right)

fluxes and the AMC model [35] is used to model the conditional scalar dissipation rate $\langle N|\eta\rangle$.

First order closure is used for the conditional chemical source terms of species $\langle w_\alpha|\eta\rangle$ and temperature $\langle w_T|\eta\rangle$. A reduced chemical mechanism taken from [36] has been used with 22 solved species (from a total of 44) and 18 reaction steps. The choice of this chemistry is motivated by a) the good agreement for auto-igniting sprays in smaller test rigs reported in [11,15], b) a sensitivity study presented in [14] comparing this mechanism to two other n-heptane chemistries, and c) the compactness and computational efficiency in view of the long process duration/integration times which cannot be addressed by parallelization.

Conditional expectations of species mass fractions and temperature have been initialized according to an adiabatic frozen mixture distribution, where a linear distribution of species concentration and enthalpy along the mixture fraction domain is assumed. The oxidizer consists of technical air and the fuel is undi-luted.

The governing equations are discretized with a second-order central differencing scheme for the diffusion terms and an upwind scheme for convective terms. The mixture fraction domain is discretized into 101 nodes clustered around stoichiometry. As outlined in [7] and shown in [17], the resolution requirements in physical space for the conditional quantities are considerably lower, compared to their unconditional counterparts. As a consequence, a two-dimensional CMC grid was employed; collapsing one dimension by means of a PDF weighted averaging in the axial direction of the disk shape representing the cylinder at TDC. The CMC grid is aligned with the spray axis and employs 42 by 43 cells, clustered in the spray vicinity, resulting in a spatial resolution of 4 mm and 1 mm in the axial and radial direction respectively. The flows field time step was kept constant at 5.0×10^{-6} s and for the CMC equations a full operator splitting between transport in physical and mixture fraction space and chemistry is employed as described in [10,16] with 10 sub-steps. Further details concerning the imple-mentation, the interfacing of CFD and CMC codes as well as the numerical procedure, the reader is directed to [10,11,16].

The uncondtional species mass fractions in the CFD code are computed by convoluting the conditional averages (obtained by the CMC code) with the mixture fraction PDF. Therefore, in the CFD code no transport equations for species are required. However, in order to reconstruct the mixture fraction PDF (presumed to be the beta function), transport equations for the mixture fraction mean and its variance are solved following common practices, e.g. [10,16].

4 Validation criteria

In the experiment, ID and LOL were defined as the time and distance from the injector tip where a minimal OH* chemiluminescence intensity of ten percent of maximal signal intensity was detected as described by [24]. In the simulation, both ID and LOL were defined by an arbitrary maximal temperature of 1600 K as employed in [23]. The calculated ignition delays and lift-off lengths exhibited a weak dependence on the threshold temperature as all cases considered have 21 percent oxygen and the rate of maximal temperature rise as well as the temperature gradient in axial direction at the lift-off location is very steep.

Figure 3 provides an example of the post-processing techniques employed by comparing the experimental flame probability (left) to the computed peak temperature determined along the line of sight parallel to the cylinder axis (right).

The experimental flame region has been determined as the spatial extent where a 50 percent probability (5 injection events out of 10) of finding a minimal OH* chemiluminescence intensity of 10 percent compared to the maximal intensity is satisfied. In the simulation a threshold value of 1600 K has been chosen for the maximal temperature along line-of-sight. The computed "liquid" region (indicated by a blue iso-line in Figure 6 and Figure 7) is defined where the maximal liquid volume fraction in a CFD cell (void fraction) along the experimental optical path has a minimal value of one percent. The term "liquid" hence denotes the area where droplets are present within the spray.

5 Results and discussion

This Section is organized as follows: first ignition de-lay times and flame LOL predictions are compared to the experimental data. Subsequently, the early stage flame development is analyzed and the influence of the orifice diameter is evaluated by means of ignition behavior and quasi-steady flame structure.

Figure 4 shows ID (upper) and flame LOL (lower) for all orifice diameters. In red are results at 900 K and in blue at 800 K ambient temperature. For the experiment, mean values and standard deviations have been calculated from the 10 injection events, whereas the simulation provides a mean value only as a RANS technique was employed. In terms of ignition delays, the measurements show a clear separation between the two ambient temperatures, where the ignition delays at 800 K are roughly twice the values at 900 K. The standard deviation of the ignition delay showed a larger variability for the lower ambient temperature indicating a larger sensitivity of the ignition delay with respect to temperature at 800 K. The direct influence of the orifice
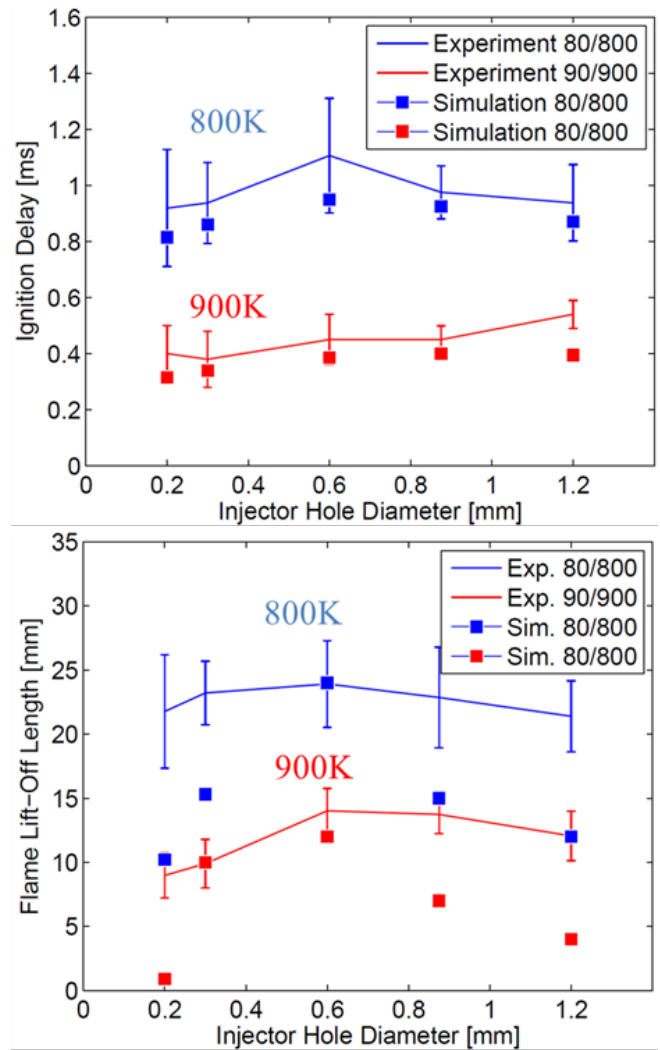
Figure 4: Comparison of experimental (solid lines) and simulated (squares) ignition delay (upper) and flame lift-off length (lower)

diameter was observed to be less pronounced with a slight increase in ID for larger nozzles at 900 K while at 800 K, ID peaks for the intermediate diameter. Both trends could be qualitatively captured by the simulation.

For the LOL there is no clear trend. According to [25] a power law of LOL $\approx d^{0.34}$ was proposed for nozzles in the range of 50 to 363 microns. Looking at the 900 K line there is an initial increase in LOL between 0.2 and 0.6 mm and a slight decrease in LOL for larger nozzles. For the colder cases the LOL is roughly twice the values of the warm case and an analogous dependency on d0 was found although less pronounced. Also for LOL the standard deviation for colder conditions is considerably higher.

The simulation was found to predict slightly lower ID than the experiment, however within the measurement variability, with the exception of the largest nozzle at the higher temperature. The weak influence on the nozzle size was well captured. On the other hand, the simulation considerably underestimated the LOL for most operating conditions. The model was capable to qualitatively reproduce changes in LOL by changing the temperature and exaggerates the reduction of the LOL for larger orifice diameters.
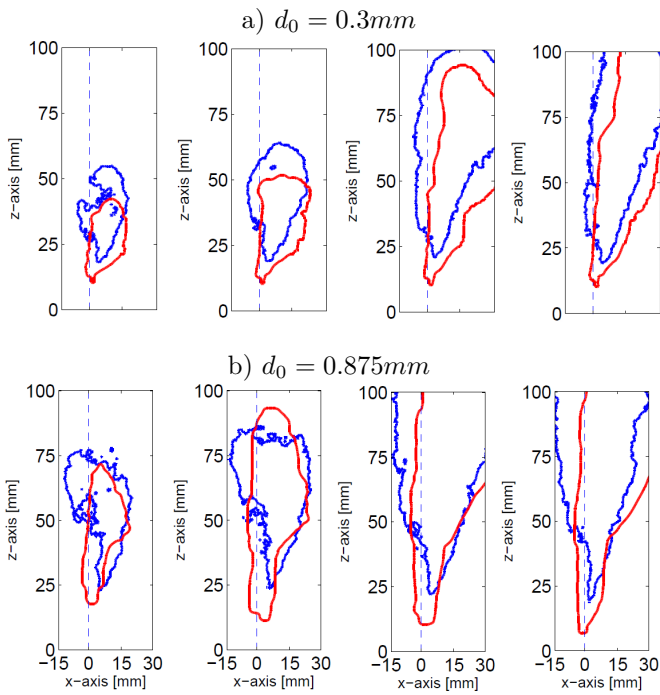
Figure 5: Temporal evolution of flame region for 0.3 mm (upper) and 0.875 mm (lower) orifice diameter at 900 K. Blue lines experiment, red lines simulation; dashed vertical line denotes spray axis
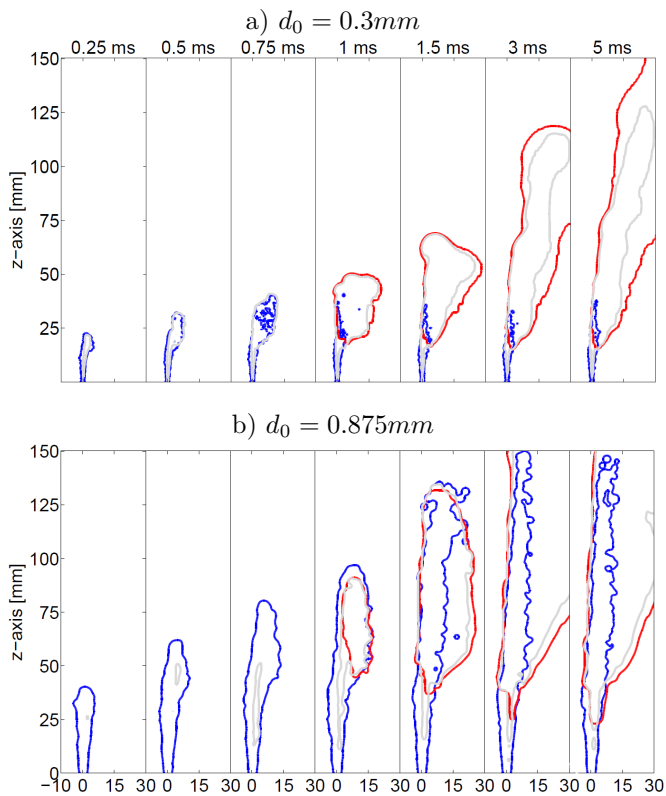
Figure 6: Temporal evolution of computed liquid region (blue) and flame region (red) for 0.3 mm (upper) and 0.875 mm (lower) orifice diameters

In the following the influence of the orifice diameter is studied on the flame region development for two different injector sizes (0.3 and 0.875 mm) at 900 K as displayed in Figure 5 at four different time instants. The experimental flame contours are drawn in blue and the simulation results in red. As a first note, the lateral deviation of the flame by the swirl motion is clearly visible and therefore also the ignition location is shifted in the direction of the swirl where the evaporated fuel is entrained and at later stages a quasi-steady lifted spray flame is established. With the larger injector the ID as well as the LOL are not considerably influenced. On the other hand, the spray penetration is larger and the lateral spray deviation is reduced due to the increased spray momentum generated by the larger fuel mass flow rate. The projected flame area is increased essentially because of the considerably larger amount of fuel injected (factor of 8).

The simulation is in qualitative agreement with experimental data although for both cases the LOL is underestimated (cf. Figure 4). The computed spray tip penetrations in the first millisecond for the smaller injector case (upper) is slightly lower than the experiment and the lateral deviation is slightly higher; the overall spray spread is however well described. For the larger injector configuration (bottom) the tip penetration is well reproduced but the lateral deviation of the spray is also overestimated. A possible explanation for this trend is the prediction of a smaller liquid droplet size compared to the experiment and therefore a more pronounced deviation of the spray is observed. At present, no validation data concerning droplet sizes is available; however measurements with Phase Doppler Anemometry (PDA) are currently underway which will provide drop size/velocity data for validation in the near future.

Figure 6 displays the simulated ignition behavior for the same two test cases considered in Figure 5. Results are shown in form of temporal evolution of liquid region (blue) and flame region (red). In addition, the stoichiometric iso-contour is drawn in gray, as visible for the 0.3 mm case (upper). The influence of the orifice diameter is evident considering the liquid region development. For the smaller nozzle a quasi-steady liquid length is reached after 1 ms which extends to approximately 30 mm from the injector tip. On the other hand, for the larger injector it takes 3 ms and the quasi-steady liquid length is around 150 mm. As a result, for larger injectors the interaction between the liquid droplet and the flame is increased. Even for the 0.3 mm case there is a slight liquid-flame overlap. Former studies in the literature revealed the liquid-flame overlap to be at around 0.15-0.2 mm depending on fuel pressure as well as ambient temperature, pressure and composition [25].

Ignition takes place between the same time instants (0.75 and 1 ms). Both ignition spots are on the lee side of the spray. However, for the smaller injector, fuel at the ignition spot has completely vaporized whereas for the larger injector ignition takes place in the presence of a considerable amount of liquid fuel as the ignition spot is embedded within the liquid region. These findings suggest that in such situations the influence of evaporating fuel droplets on the flame may be particularly important and call for further studies in this matter.
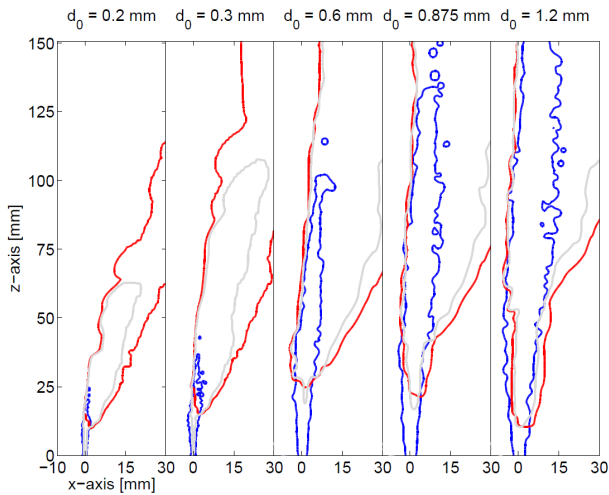
Figure 7: Computed liquid region (blue) and flame region (red) for different orifice diameters at 10 ms after SOI. Grey line stoichiometric iso-contours

The structure of the computed fully-developed spray at 10 ms after SOI for five different orifice diameters is illustrated in Figure 7. The liquid region is indicated by the blue contour while the red line denotes the flame region.

As above, the grey line represents the stoichiometric iso-contour. The liquid length increases, as expected, monotonically with the nozzle diameter. The lateral spray deviation caused by the swirling environment is higher for the smaller injector because of the smaller droplets and lower spray momentum due to the reduced fuel mass injected.

Looking at the stoichiometric region, there is a linear increase of the fuel rich axial extent with increasing orifice diameter due to scalar mixing. This is clearly visible for the cases 0.2 and 0.3 mm.
Soot is expected to be oxidized downstream of this region. For the larger injectors, the region of fuel rich conditions extends up to 300-400 mm rendering these large injectors highly prone to extensive levels of soot formation.

The structure of the flame for the larger injector is shown more in detail in Figure 8 by means of a cut-plane on the injector axis showing from left to right: mean mixture fraction, temperature, mass fractions of OH and O_2 and volumetric chemical heat release rate (the latter is drawn in logarithmic scale). Note that the axial extent of the images is 250 mm, i.e. larger than in the former visualizations. The strong evaporation region at around 130-150 mm corresponds to the high levels of mixture fraction. Downstream from the LOL a typical diffusion flame is established with high temperature and OH mass fractions are found along the stoichiometric iso-contour.

Due to the strong swirling motion, the flame burns more vigorously in the swirl direction side of the spray as recognizable from the temperature distribution. The oxygen is completely consumed in the fuel rich region apart from the region of strong fuel evaporation. This behaviour is characteristic for large injectors with a considerable liquid-flame overlap. The fuel rich region at low temperatures with oxygen remaining is surrounded by a high heat release rate indicating an energetic balance between evaporation and chemical activity. In the strong evaporation region the oxygen is not completely consumed because the heat released by the chemical reaction is counteracted by the heat of evaporation of the fuel. Further downstream (160-180 mm) rich combustion takes place and the oxygen is rapidly consumed.

6 Conclusions

This study summarizes a joint experimental and numerical study of the influence of nozzle diameter on ignition delay, lift-off length and flame evolution of Diesel sprays at engine relevant conditions. The nozzle diameters investigated span from 0.2 to 1.2 mm, where the larger values are representative of two-stroke marine engine fuel injectors and hence extends the range reported in the open literature for smaller injectors.

Investigations have been carried out at two temperature levels (800 and 900 K) for a total of five different diameters resulting in ten sets of data. The diagnostics applied include high-speed shadow imaging to describe the spray morphology as well as high-speed OH* chemiluminescence imaging providing information on the flame front evolution. The experimental data confirms previous findings for smaller injector diameters in that the injector diameter exhibits only a weak influence on the ignition delays and flame lift-off length. The variation in ambient temperature however lead to significant differences in both quantities and the variability of the predictions (10 injections have been carried out for each measurement point) is considerably higher for the lower temperature, as expected.

A Conditional Moment Closure combustion model has subsequently been used to model the acquired data. The predicted ignition delays are in good agreement with the experimental data and fall within the measurement variability with the exception of one measurement point. The lift-off lengths are under-predicted at both temperature levels and the impact of the orifice diameter is clearly overestimated. The location of ignition and the ensuing early flame spread is in fair agreement with the imaging data as is demonstrated for a selection of two diameters. The numerical platform was subsequently employed towards gaining insight with respect to the influence of orifice diameter on ignition behaviour and quasi-steady spray characteristic. Overall it can be concluded, that CMC shows high potential for the prediction of auto-igniting Diesel sprays at marine engine conditions. However, for larger orifice diameters, the presence of droplets in the combustion zone requires further investigation in future work.

Acknowledgements
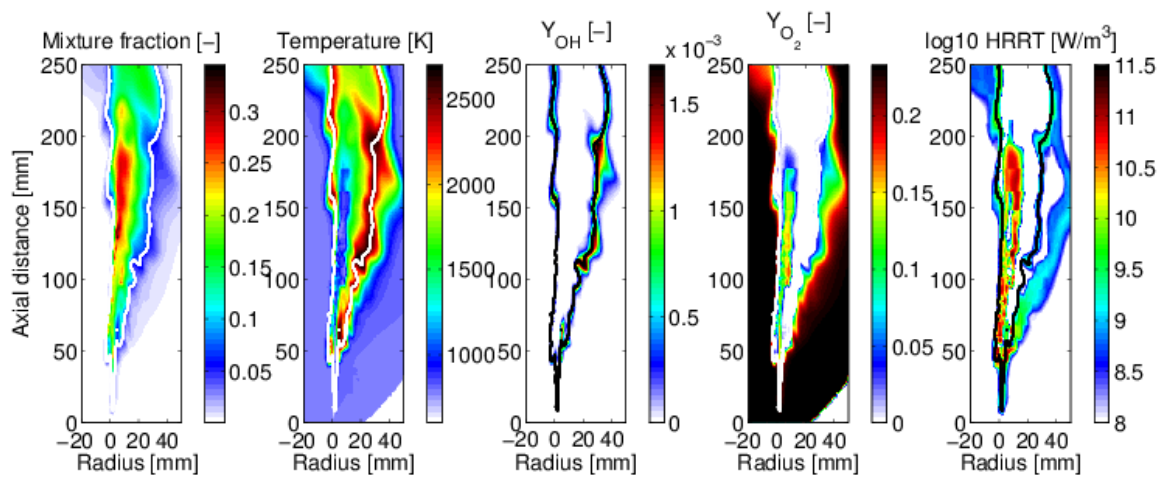
Figure 8: Isocontours of mixture fraction, temperature, OH, O_2 species mass fractions and heat release rate in logarithmic scale for the Case 7 (0.875 mm and 800 K). Isolines of the stoichiometric mixture fraction ξ_{st} are superimposed in white or black

Nomenclature

CFD:	Computational Fluid Dynamics
CMC:	Conditional Moment Closure
HFO:	Heavy Fuel Oil
HRRT:	Heat Release RaTe
ID:	Ignition Delay
LOL:	Lift-Off Length
LDV:	LASER Doppler Velocimetry
PDA:	Phase Doppler Anemometry
PDF:	Probability Density Function
RANS:	Reynolds Averaged Navier Stokes
RPM:	Revolutions Per Minute
SCC:	Spray Combustion Chamber
SOI:	Start Of Injection
d_0:	Nozzle orifice diameters

References

[1] Pitz, W.J. and Mueller, C.J., Prog. Energy Combust. Sci. 37:330 (2011)

[2] Maas, U., and Pope, S.B., Comb. Flame 88:239 (1992)

[3] Kong, S.-C., Han, Z. and Reitz, R.D., SAE technical paper no. 950278 (1995)

[4] Tap, F. A., Hilbert, R., Thévenin, D. and Veynante, D., Comb. Theory and Modelling 8:165 (2004)

[5] Kung, E.H. and Haworth, D.C., SAE Int. J. Engines 1:591 (2009)

[6] Barths, H., Hasse, C., Bikas, G. and Peters, N., Proc. Combust. Inst. 28: 1161 (2000)

[7] Klimenko, A. Y. and Bilger, R. W., Prog. Energy Combust. Sci. 25: 595-687 (1999)

[8] Mastorakos, E., Prog. Energy Combust. Sci. 35: 57-97 (2009)

[9] Kim, W. T. and Huh, K. Y., Proc. Combust. Inst. 29:569 (2002)

[10] Wright, Y.M., De Paola, G., Boulouchos, K. and Mastorakos, E., Comb. Flame 143:402 (2005)

[11] Wright, Y.M., Margari, O.-N., Boulouchos, K., De Paola, G. and Mastorakos, E., Flow, Turbulence and Combustion 84:49 (2010)

[12] Borghesi, G., Mastorakos, E., Devaud, C.B. and Bilger, R.W., Comb. Theor. Mod. 15:725 (2011)

[13] Bottone, F., Kronenburg, A., Marquis, A. and Gosman, A.D., Flow Turbul. Combust. 88:233-252 (2012)

[14] Bolla, M., Gudmundsson, T., Wright, Y.M. and Boulouchos, K., SAE Int. J. Engines 6 (2), 1249-1261 (2013)

[15] Bolla, M., Wright, Y.M., Boulouchos, K., Borghesi, G. and Mastorakos, E., Combustion Science and Technology 185 (5), 766-793 (2013)

[16] De Paola, G., Mastorakos, E., Wright, Y.M. and Boulouchos, K., Comb. Sci. Tech. 180:883 (2008)

[17] Wright, Y.M., De Paola, G., Mastorakos, E. and Boulouchos, K., Int. Journal of Engines 2 (1):714 (2009)

[18] Farrace, D., Bolla, M., Wright, Y.M. and Boulouchos, K., accepted for publication in SAE technical paper no. 2013-24-0016 (2013)

[19] Barroso, G., Schneider, B., and Boulouchos, K., SAE technical paper no. 2003-01-3230 (2003)

[20] Pizza, G., Wright, Y.M., Weisser, G. and Boulouchos, K., Int. J. Vehicle Design 45:80 (2007)

[21] Aneja, R., and Abraham, J., Comb. Sci. Tech. 138:233 (1998)

[22] Bolla, M., Cattin, M.A., Wright, Y.M., Boulouchos, K. and Schulz, R., ASME ICES2012-81016, Torino, Italy (2012)

[23] Bolla, M., Wright, Y.M. and Boulouchos, K., Proceedings of COMODIA, Fukuoka, Japan (2012)

[24] Schmid, A., von Rotz, B., Bombach, R., Weisser, G., Herrmann, K. and Boulouchos, K., Proceedings of COMODIA, Fukuoka, Japan (2012)

[25] Siebers, D.L. and Higgins, B., SAE technical paper no. 2001-01-0530 (2001)

[26] Herrmann, K., Kyrtatos, A., Schulz, R., Weisser, G., von Rotz, B., Schneider, B. and Boulouchos, K., ICLASS, Vail, Colorado, USA (2009)

[27] Herrmann, K., von Rotz, B., Schulz, R., Weisser,G., Boulouchos, K. and Schneider, B., ILASS, Brno, Czech Republic (2010)co c

[28] von Rotz, B., Herrmann, K., Weisser, G., Cattin, M., Bolla, M. and Boulouchos, K., ILASS, Estoril, Portugal (2011)

[29] Herrmann, K., von Rotz, B., Schulz, R., Weisser, G., Schneider, B. and Boulouchos, K., Proceedings of the International Symposium on Marine Engineering, ISME-111, Kobe, Japan (2011)

[30] Herrmann, K., Schulz, R. and Weisser, G., CIMAC, paper no. 98, Vienna, Austria (2007)

[31] CD-Adapco, Methodology, Star-CD v4.16 (2013)

[32] Schulz, R. et. al, CIMAC, paper no. 247, Bergen, Norway (2010)

[33] Huh, K. Y. and Gosman, A. D., ICMF (1991)

[34] Reitz, R.D. and Diwakar, R., SAE technical paper no. 870598 (1987)

[35] O'Brien, E. E. and Jiang, T. L., Phys. Fluids 3:3121 (1991)

[36] Liu, S., Hewson, J. C., Chen, J. H. and Pitsch, H., Comb. Flame 137:320 (2004)

Turbulent Combustion Under Supercritical Conditions

L. Selle[1,2]

[1] *Université de Toulouse; INPT, UPS; IMFT (Institut de Mécanique des Fluides de Toulouse)*
Allée Camille Soula, F-31400 Toulouse, France
[2] *CNRS; IMFT; F-31400 Toulouse, France*

Abstract

The recent advances in the numerical simulation of turbulent combustion for liquid rocket engines are presented. Modeling aspects and the specificities of supercritical thermodynamic conditions are discussed. The objective is to give a rapid overview of the most recent results on the simulation of supercritical laminar flames, mixing, turbulent combustion and combustion instabilities.

1   Introduction

The tremendous power-density ratio of liquid-fuel rocket engines (LRE) is achieved partly thanks to the very high pressure in the combustion chamber. For the vast majority of these engines, at nominal operating conditions, the pressure is larger than the critical pressure, P_c, of the individual reactants (*cf.* 1). For example, the Vulcain engine –first-stage LRE of the european launcher Ariane 5– operates at 117 bar and uses oxygen and hydrogen as reactants. One of the main features of fluids above their

Table 1: Selected species properties at critical point: critical pressure, P_c, temperature, T_c, density, ρ_c, and acentric factor, ω_c. (Data from http://webbook.nist.gov/chemistry/fluid/).

Fluid	H_2	O_2	H_2O	CH_4
P_c [bar]	12.964	50.430	220.640	45.992
T_c [K]	33.145	154.581	647.096	190.564
ρ_c [kg.m^{-3}]	31.263	436.10	322.00	162.66
ω_c	-0.219	0.0222	0.3443	0.01142

critical pressure is that the phase-change phenomenon no longer occurs, *i.e.* the density undergoes continuous variations when temperature changes. However, the density variations versus temperature can be very steep, resulting in large density gradients. This peculiar behaviour is at the root of the specificities of supercritical-fluid flows and the cause for many practical and theoretical difficulties.

The original design of LRE, some 70 years ago, was achieved by a costly trial-and-error process. As pointed out by Hawthorne [1], 'No one *designs* an injector plate with its multitude of small holes, they *develop* it.' In the early days, the lack of non-intrusive measurement techniques would limit the detailed understanding of flow patterns and combustion dynamics under such extreme thermodynamic conditions. Moreover, the rush

to build rockets –whether during World War II or the Cold War– would provide virtually unlimited funds for testing. Much progress has been made over the past twenty years with the systematic study of supercritical flows in reduced-scale experiments. Direct visualisation and modern optical diagnostics such as Raman scattering to measure point-wise density [2] or temperature [3] and laser-induced fluorescence for flame dynamics [4] allowed to significantly improve the level of understanding for these flows.

Nevertheless, experiments at high pressure are still very expensive and the presence of density gradients is a major hurdle for optical diagnostics. For these reasons, there is a growing interest to supplement theoretical and experimental works with numerical simulations of LRE. Additionally, for topics such as the prediction of combustion instabilities, there are sometimes few alternatives to numerical simulation. Indeed, some unstable modes seem to require a close to full-scale setup to be excited but they often lead to a rapid destruction of the engine and the associated safety and cost issues.

Aside from LRE, other applications could benefit in the near future from the advances in the numerical simulation of supercritical fluids. Because of the increase in operating pressure in gas turbines, aeronautical turbines and piston engines, real-gas effects are likely to occur at the injection of liquid fuel.

The intent of this paper is to provide a brief overview of the ongoing research in the numerical simulation of supercritical flows for rocket engines. It is not an exhaustive review as its main focus is on the french teams tackling this problem. The organization of the paper is as follows:

- In Section 2, the modeling of thermodynamics and transport phenomena under supercritical conditions is presented.

- Section 3 is an overview of laminar simulations in the counterflow diffusion flame configuration.

- The simulation of non-reacting turbulent flows representative of injection in LRE is discussed in Sec. 4.

- Finally the state of the art on turbulent reacting flows in LRE is briefly illustrated in Sec. 5

2   Modelling challenges

Because of large densities, the ideal-gas approximation is no longer valid under supercritical conditions, so that the starting point for modeling is the equation of state (EOS). While very detailed and accurate formulations

have been proposed, such as the Benedict-Webb-Rubin EOS [5], they are impractical for numerical simulations of unsteady reacting flows because of their computational cost. The alternative –to compromise between accuracy and computational cost– is to use a cubic EOS, which may be written in a generic form as

$$P(v,T) = \frac{RT}{v-b} - \frac{a(T)}{(v+\delta_1 b)(v+\delta_2 b)} \quad (1)$$

where P is the pressure, T the temperature, v the molar volume and R the perfect-gas constant. The coefficients a and b account respectively for long-range and short-range interactions between molecules. They are usually modeled with the *corresponding states principle*, which assumes the existence of a set of reduced variables with respect to which all species follow a universal behavior. The parameters (δ_1, δ_2) may be set to recover the most classical cubic EOS: the Peng-Robinson (PR) EOS [6] corresponds to $(1+\sqrt{2}, 1-\sqrt{2})$, the Soave-Redlich-Kwong (SRK) EOS [7] is found with $(1,0)$ while using $(0,0)$ yields the Van der Waals EOS. Interesting historical perspectives and practical information about cubic EOS may be found in [8].

Then, high-pressure effects must be accounted for in the thermodynamic description of the fluid. Typically, the thermodynamic coefficients that usually depend on temperature and composition (heat capacities, speed of sound, *etc.*) now also vary with pressure. A standard practice at low pressure is to tabulate or use polynomial fits for the temperature dependance. It is possible to extend this procedure to the pressure, however, consistency with the EOS must be checked. A good alternative is to keep the tabulation for low-temperature reference and use departure functions based on the EOS to compute the influence of pressure [9, 10, 11]. For example, considering a pure species, the Gibbs function, G reads:

$$G(P,T) = G_0 + Pv - RT + \int_v^{v_0} P(v',T)\, dv' \quad (2)$$

where v_0 is the molar volume at a reference (low) pressure and G_0 the value of the Gibbs function at this reference. The enthalpy, h, is then defined as

$$h = G - T\left(\frac{\partial G}{\partial T}\right)_p \quad (3)$$

and the constant-pressure heat capacity, C_p is

$$C_p = \left(\frac{\partial h}{\partial T}\right)_p \quad (4)$$

It is clear that with the EOS (*cf.* 1) and a low-pressure reference G_0, one may compute all the thermodynamic properties of the fluid.

Modeling transport phenomena at high pressure is a much more arduous task and still a major source of uncertainty for numerical simulations. Theories based on non-equilibrium thermodynamics have been proposed [12, 13] that account for Soret and Dufour diffusion fluxes and can reproduce non-miscibility phenomena in dense fluids. These detailed models however suffer from the lack of experimental data to calibrate the individual diffusion coefficients. Because of the additional uncertainties inherent to turbulence modeling, they are also seldom used for the simulation of practical configurations.

The latter point is of major importance for the design of LRE. Indeed, it has been shown from experiments [14] and numerical simulations [15] that the structure of turbulence in affected by the presence of large density gradients. Therefore, turbulence modeling under supercritical conditions should in principle account for this specificity [16, 17].

It appears from the above –non exhaustive– list that modeling supercritical fluid flows for the simulation of LRE is a daunting task. For this reason, the various research groups who tackle this problem do not always resort to the same set of hypothesis. For large Reynolds number flows, it is common practice to simplify transport modeling.

Finally, two crucial points for the simulation of LRE were intentionally left out: turbulent combustion and numerics. These are major issues that would require lengthy discussions outside of the scope of the present paper.

3 Laminar flames

The first and mandatory step towards the simulation of turbulent reacting flows is the computation of laminar flames. The reduced complexity of the flow field allows for a thorough investigation of chemical kinetics and interactions with thermodynamics and transport. Excluding engines that use hypergolic propellants, the standard injection in LRE uses coaxial jets of fuel and oxidizer. Because of the very high reactivity at large pressure, it is thought that combustion mainly occur in the diffusion regime, that is fuel and oxidizer do not mix prior to burning. Consequently, the ideal configuration of a steady-state stretched diffusion flame is deemed representative (*cf.* 1). The flame sits close to the stagnation
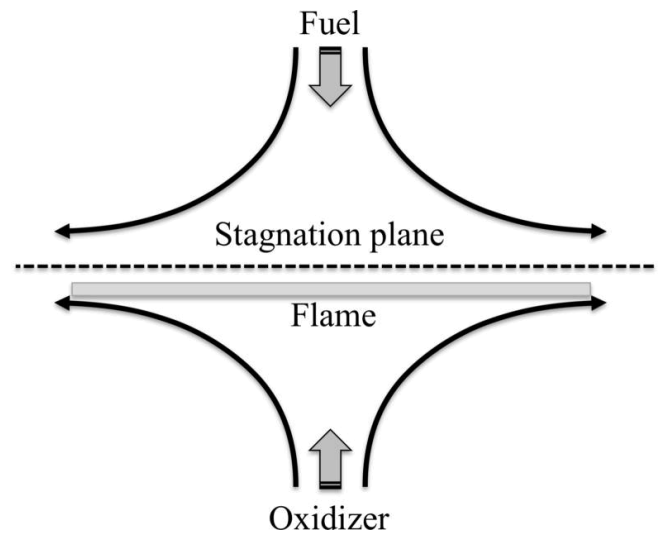
Figure 1: Typical configuration for a stretched laminar diffusion flame.

plane resulting from two opposed jets while the stretch rate is controlled by their relative velocity. This configuration is essentially one-dimensional, with the relevant coordinate being the position along the axis of symmetry.

Various groups including EM2C at Ecole Centrale Paris [18, 19, 20, 21], CMAP at Ecole Polytechnique and ONERA [22, 13, 23] have used this configuration for fundamental studies. The influence of pressure and strain rates on basic flame properties such as flame thickness and extinction limits were assessed. For example, a useful result for engine design is that the flame thickness evolves like the inverse square root of the product

between pressure and strain rate [18, 19]. At super-critical pressures there is no discontinuous phase change but across the continuation of the phase-equilibrium line, species undergo large density variations. The configuration of 1 is also useful to study this pseudo-evaporation process and define Spalding-like correlations [20].

The detailed transport models used in these computations allow the assessment of the influence of each specific contribution to the global flame properties. Peculiar phenomena such as mixture non-idealities resulting in phase separation have also been predicted [23].

These detailed simulations show that cross-diffusion terms (Soret and Dufour) have an impact on flame structures, especially when the species have very different molecular weights, such as oxygen and hydrogen. Nevertheless, this impact is often modest so that neglecting these term is not the most drastic approximation when performing Large-Eddy Simulations (LES) of high-Reynolds reacting flows. This result has been found in other studies [24, 25].

4 Non-reacting turbulent flows

The injection of the reactants in the combustion chamber of a LRE usually involves jets. Therefore, understanding the mechanisms controlling their dynamics and mixing is of major importance. The simulation of non-reacting jets is relevant prior to ignition but it is particularly useful for validation purposes. Indeed, without the added complexity of chemical reactions, experiments are easier and cheaper to conduct. Detailed measurements are available in the literature [26].

LES of supercritical jets is fairly recent [27] and turned out to predict qualitative features consistent with experiments and sometimes quantitative results. For example, a collaboration between CERFACS and IMFT was able to reproduce the experiments of Mayer *et al.* [28] for two operating points [29, 30] with the AVBP solver.[1] In particular, the simulations predict the differences induced by an increase in injection temperature by 8 K, corresponding to the transition from transcritical to supercritical injection. Similar work is being done at CORIA (*cf.* 2)
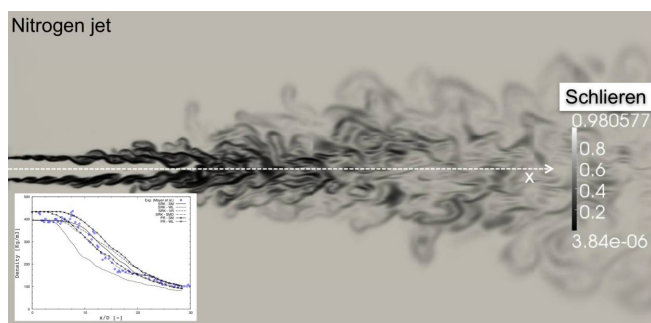
Figure 2: Reconstructed Schlieren view of a nitrogen jet corresponding to 'case 3' by Mayer *et al.* [28]. Image courtesy of G. Ribert from CORIA.

with the SiTComB solver,[2] as well as the application to cooling channels [31].

The above work addresses simple-jet configuration but the team at EM2C also studied turbulent mixing in coaxial jets with LES [32]. By varying the ratio, J, of momentum flux between the inner and outer streams, they showed how the structure of the initial jet development

---

[1]www.cerfacs.fr/cfd/avbp_code.php
[2]http://www.coria-cfd.fr/index.php/SiTCom-B

is affected (*cf.* 3). Above a certain ratio, the formation of a recirculation zone was shown to drastically reduce the 'dark core' length. A useful feature of LES is that unsteady features of the flow can be analyzed such as natural unstable modes or forced response to acoustic modulation. Understanding these phenomena may be crucial for the prevention of combustion instabilities in LRE.
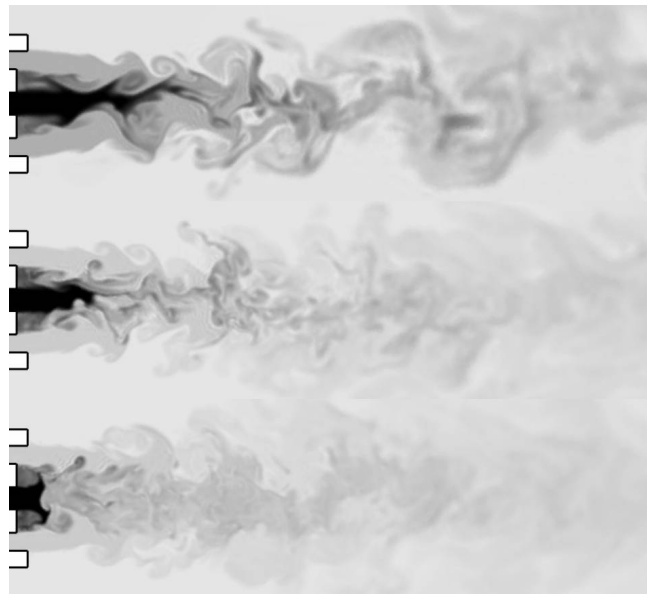
Figure 3: Longitudinal cut of density from cases N2 ($J = 1.05$), N6 ($J = 3.05$) and N8 ($J = 9.3$) of Schmitt *et al.* [32] (top to bottom). As the momentum flux ratio, J, is increased, the jet penetration is reduced. A recirculation bubble is eventually formed for the case with the higher momentum flux ratio (bottom picture). Images courtesy of T. Schmitt from EM2C.

Unfortunately, even for these relatively simple non reacting flows, few experimental diagnostics remain accurate at high-pressure resulting in a lack of validation. Apart from direct visualization, which is useful for qualitative validation, only mean density profiles are available. This means that neither instantaneous flow dynamics nor mixing can be directly confronted with experiments.

5 Turbulent combustion

Very few facilities can accommodate a supercritical-combustion test bench. Notably, AFRL in the USA and DLR in Germany have such capability [26] and have provided the scientific community with high-quality results for more than 15 years. In France, the Mascotte bench operated by ONERA [3] is equipped with optical access and Laser diagnostics that allow a detailed investigation of features such as flame stabilization [4] or the response to acoustic forcing [33, 34].

The availability of the Mascotte results drive the simulation community. For example, the team at CORIA have performed a 3D LES of the ignition of a single injector with methane and oxygen as reactants. A longitudinal cut of oxygen mass fraction is presented in 4. A temperature iso-surface at $T = 2000$ K shows the development of the initial burnt-gases pocket and a stoichiometric contour indicates where the mixture is most likely to burn. As in the non-reacting simulations of 3, one can see that the dense oxygen stream is broken at a
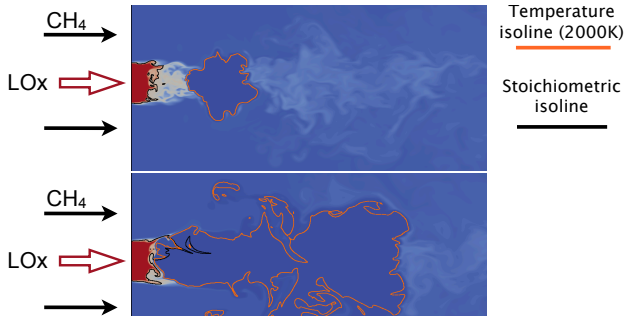
Figure 4: Evolution (top to bottom) of a pocket of burnt gases, representative of the ignition of a methane / oxygen coaxial injector of the Mascotte bench. Longitudinal cut of oxygen mass-fraction with $T = 2000$ K and stoichiometric iso-surfaces. Image courtesy of G. Ribert from CORIA.

very short distance from the injector because of the large momentum-flux ratio between the two streams. The recirculation of burnt gases in the wake of the oxygen stream is likely to favor ignition success and flame stabilization.

A detailed discussion of turbulent combustion modeling for LRE is beyond the scope of the present paper. Many strategies are possible, for example the simulations of 4 use a tabulated flamelet model [35] but when hydrogen is the fuel, its reactivity is so high that infinitely-fast chemical reaction is a good approximation [36]. However, when addressing phenomena such as flame stabilization near the injector, accounting for finite chemical rates through detailed mechanisms may be mandatory. For example, 2D simulations were conducted at CERFACS and IMFT in order to study the early development of the flame in the wake of the injector lip that separates the reactant streams [37, 38]. 5 shows how the thickness
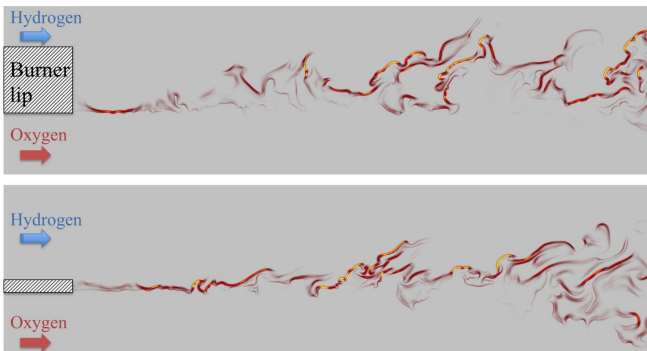
Figure 5: Instantaneous field of heat release rate behind a splitter plate. Splitter height is $h = 0.5$ mm and $h = 0.1$ mm at the top and bottom, respectively.

of the lip affects flame stabilization. These results are Direct Numerical Simulations (DNS) in the sense that no sub-grid turbulence or turbulent combustion models are used. A detailed 13-step kinetic scheme accounts for unsteady chemical effects: one can see in 5 that some regions exhibit much weaker heat-release rate. It was shown that they correspond to pockets of burnt gases entrained in the oxygen stream, resulting in the further oxidization of dissociated combustion products. Another topic that is currently being tackled with this configuration is the joint simulation of combustion in the fluid and heat transfer in the injector lip.

LES has proven to be a very powerful tool, predicting flame length or the influence of design parameters such

as the recess of the inner injector [39]. These computations were conducted on single injectors but as of this day, the frontier of supercritical-reacting-flows simulation is the simultaneous computation of multiple injectors. Thanks to the european PRACE program,[3] using 8.5 million CPU hours on the CURIE machine operated by GENCI, a joint effort of EM2C and CERFACS teams resulted in the computation of the five-injector configuration of the Mascotte test bench. 6 shows instantaneous
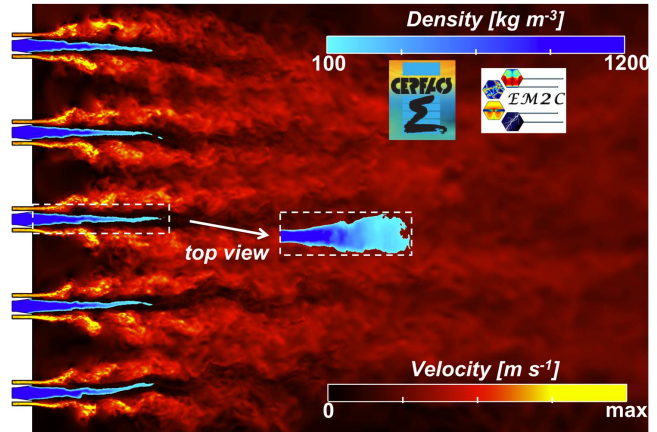
Figure 6: Longitudinal cut of instantaneous velocity and density fields in the five-injector MIC configuration of the Mascotte bench [34] under transverse acoustic modulation. Images courtesy of T. Schmitt from EM2C.

fields of density and velocity. In this simulation, the first transverse mode of the combustion chamber is excited so that the combustion is strongly modulated. The flames and dense-core lengths are greatly reduced by the transverse acoustic excitation, but the details of the individual flame responses vary, depending on their position relative to the acoustic field. The central flame, located at a velocity anti-node experiences a strong transverse flapping movement that flattens the dense core, as can be seen in the top view.

The central injector is singled out in 7 illustrating how it is strongly wrinkled by turbulence but more importantly how it is flattened by the transverse acoustic fluctuation. The ability to predict such deformation is one
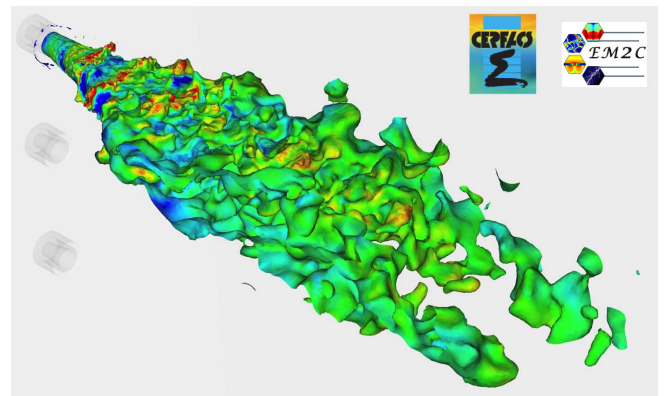
Figure 7: Zoom on the central injector of the MIC configuration of the Mascotte bench, highlighting the jet flattening in the spanwise direction. Temperature iso-surface colored by velocity. Images courtesy of T. Schmitt from EM2C.

of the assets of LES. It has a strong impact on mixing

---

[3]www.prace-ri.eu/IMG/pdf/prace_annual_report_2012.pdf

and turbulence and is key for the study of combustion instabilities in LRE.

6 Conclusions

The current status of numerical simulation of combustion in liquid rocket engines has been briefly reviewed, with a focus on the recent work conducted in various french laboratories. All the aspects of supercritical flows and supercritical combustion are covered, from the detailed modeling of thermodynamics and transport at high-pressure in simple configuration to the computation of multiple flames in engine-relevant configurations. For a broader view on all propulsion applications, the reader is referred to the review of Candel *et al.* [40].

Considerable progress was made in the last ten years so that mature modeling tools are now available to the community for the study of mixing, combustion and combustion instabilities at high pressure. Nevertheless, the lack of quantitative, local and instantaneous measurement techniques under these extreme thermodynamic conditions is a major hurdle. Validation cases are scarce and further developments of LES and combustion models are hazardous without validation. An other modeling issue that remains to be addressed is the transition from low-pressure two-phase regimes to supercritical conditions. Such model is required for the simulation of an ignition sequence of a LRE.

Considerations about the numerical challenges associated with supercritical combustion have intentionally been left out. In particular, dealing with the large density gradients and the associated non-linearities requires stabilizations techniques that may affect the accuracy of the simulation. Significant efforts will be needed on this front.

Finally, it appears that the next challenge is the simulation of a complete combustion chamber with dozens of injectors, from the injection dome to the nozzle. Numerical tools are in principle ready for this daunting task so that it seems likely that such simulation may be done in the next five years.

Acknowledgment

References

[1] W. R. Hawthorne, "Review: Theory of Combustion Instability in Liquid Propellant Rocket Motors, by Luigi Crocco and Sin-I Cheng.," *J. Fluid Mech.*, vol. 2, pp. 100–104, Mar. 1957.

[2] M. Oschwald and A. Schik, "Supercritical nitrogen free jet investigated by spontaneous Raman scattering," *Experiments in fluids*, vol. 27, no. 6, pp. 497–506, 1999.

[3] M. Habiballah, O. M., F. Grisch, L. Vingert, and P. Gicquel, "Experimental studies of high-pressure cryogenic flames on the MASCOTTE facility," *Combust. Sci. Tech.*, vol. 178, pp. 101–128, Jan. 2006.

[4] G. Singla, P. Scouflaire, C. Rolon, and S. Candel, "Planar laser-induced fluorescence of OH in high-pressure cryogenic LOx/GH2 jet flames," *Combust. Flame*, vol. 144, pp. 151–169, Jan. 2006.

[5] M. Benedict, G. Webb, and L. Rubin, "An Empirical Equation for Thermodynamic Properties of Light Hydrocarbons and Their Mixtures I. Methane, Ethane, Propane and n-Butane," *The Journal of Chemical Physics*, vol. 8, p. 334, 1940.

[6] D.-Y. Peng and D. B. Robinson, "A New Two-Constant Equation of State," *Ind. Eng. Chem., Fundam.*, vol. 15, no. 1, pp. 59–64, 1976.

[7] G. Soave, "Equilibrium constants from a modified Redlich-Kwong equation of state," *Chemical Engineering Science*, vol. 27, no. 6, pp. 1197–1203, 1972.

[8] G. Soave, "20 years of Redlich-Kwong equation of state," *Fluid Phase Equilibria*, vol. 82, pp. 345–359, 1993.

[9] J. M. Prausnitz, R. N. Lichtenhaler, and E. Gomes de Azevedo, *Molecular thermodynamics of fluid-phase equilibria.* Upper Saddle River: Prentice Hall, 3rd ed., 1998.

[10] B. E. Poling, J. M. Prausnitz, and O. John Paul, *The properties of gases and liquids.* New York: McGraw-Hill, 5th ed., 2001.

[11] R. S. Miller, K. G. Harstad, and J. Bellan, "Direct numerical simulations of supercritical fluid mixing layers applied to heptane-nitrogen," *J. Fluid Mech.*, vol. 436, pp. 1–39, June 2001.

[12] K. Harstad and J. Bellan, "Isolated fluid oxygen drop behavior in fluid hydrogen at rocket chamber pressures," *International Journal of Heat and Mass Transfer*, vol. 41, pp. 3537–3550, Nov. 1998.

[13] V. Giovangigli and L. Matuszewski, "Supercritical fluid thermodynamics from equations of state," *Physica D: Nonlinear Phenomena*, vol. 241, pp. 649–670, Mar. 2012.

[14] I. A. Hannoun, H. J. S. Fernando, and E. J. List, "Turbulence structure near a sharp density interface," *J. Fluid Mech.*, vol. 189, pp. 189–209, Apr. 1988.

[15] N. A. Okong'O and J. Bellan, "Turbulence and fluid-front area production in binary-species, supercritical, transitional mixing layers," *Physics of Fluids*, vol. 16, no. 5, p. 1467, 2004.

[16] L. C. Selle, N. A. Okong'O, J. Bellan, and K. G. Harstad, "Modelling of subgrid-scale phenomena in supercritical transitional mixing layers: an a priori study," *J. Fluid Mech.*, vol. 593, pp. 57–91, Nov. 2007.

[17] E. S. Taskinoglu and J. Bellan, "A posteriori study using a DNS database describing fluid disintegration and binary-species mixing under supercritical pressure: heptane and nitrogen," *J. Fluid Mech.*, vol. 645, p. 211, Feb. 2010.

[18] L. Pons, N. Darabiha, and S. Candel, "Pressure effects on nonpremixed strained flames," *Combust. Flame*, vol. 152, pp. 218–229, Jan. 2008.

[19] G. Ribert, N. Zong, V. Yang, L. Pons, N. Darabiha, and S. Candel, "Counterflow diffusion flames of general fluids : Oxygen / hydrogen mixtures," *Combust. Flame* , vol. 154, pp. 319–330, 2008.

[20] L. Pons, N. Darabiha, S. Candel, G. Ribert, and V. Yang, "Mass transfer and combustion in transcritical non-premixed counterflows," *Combustion Theory and Modelling*, vol. 13, pp. 57–81, Jan. 2009.

[21] L. Pons, N. Darabiha, S. Candel, T. Schmitt, and B. Cuenot, "The structure of multidimensional strained flames under transcritical conditions," *Comptes Rendus Mécanique*, vol. 337, pp. 517–527, June 2009.

[22] V. Giovangigli, L. Matuszewski, and F. Dupoirieux, "Detailed modeling of planar transcritical H2-O2-N2 flames," *Combustion Theory and Modelling*, vol. 15, no. 2, pp. 141–182, 2011.

[23] V. Giovangigli and L. Matuszewski, "Numerical simulation of transcritical strained laminar flames," *Combust. Flame* , vol. 159, pp. 2829–2840, Sept. 2012.

[24] S. Palle, C. Nolan, and R. Miller, "On molecular transport effects in real gas laminar diffusion flames at large pressure," *Physics of Fluids*, vol. 17, p. 103601, 2005.

[25] S. Palle and R. Miller, "Analysis of high-pressure hydrogen , methane , and heptane laminar diffusion flames: Thermal diffusion factor modeling," *Combust. Flame* , vol. 151, no. 4, pp. 581–600, 2007.

[26] M. Oschwald, J. Smith, R. Branam, J. Hussong, A. Schik, B. Chehroudi, and D. Talley, "Injection of fluids into supercritical environments," *Combust. Sci. Tech.* , vol. 178, no. 1, pp. 49–100, 2006.

[27] N. Zong and V. Yang, "Cryogenic Fluid Jets and Mixing Layers in Transcritical and Supercritical Environments," *Combust. Sci. Tech.* , vol. 178, pp. 193–227, Jan. 2006.

[28] W. Mayer, J. Telaar, R. Branam, G. Schneider, and J. Hussong, "Raman Measurements of Cryogenic Injection at Supercritical Pressure," *Heat and Mass Transfer*, vol. 39, pp. 709–719, Sept. 2003.

[29] T. Schmitt, L. Selle, B. Cuenot, and T. Poinsot, "Large-Eddy Simulation of transcritical flows," *Comptes Rendus Mécanique*, vol. 337, pp. 528–538, June 2009.

[30] T. Schmitt, L. Selle, A. Ruiz, and B. Cuenot, "Large-Eddy Simulation of Supercritical-Pressure Round Jets," *AIAA Journal* , vol. 48, pp. 2133–2144, Sept. 2010.

[31] G. Ribert, D. Taieb, X. Petit, G. Lartigue, and P. Domingo, "Simulation of supercritical flows in rocket-motor engines: application to cooling channel and injection system," *Progress in Propulsion Physics*, vol. 4, pp. 205–226, Mar. 2013.

[32] T. Schmitt, J. Rodriguez, I. a. Leyva, and S. Candel, "Experiments and numerical simulation of mixing under supercritical conditions," *Physics of Fluids*, vol. 24, no. 5, p. 055104, 2012.

[33] F. Richecoeur, S. Ducruix, P. Scouflaire, and S. Candel, "Experimental investigation of high-frequency combustion instabilities in liquid rocket engine," *Acta Astronautica*, vol. 62, pp. 18–27, Jan. 2008.

[34] Y. Méry, L. Hakim, P. Scouflaire, L. Vingert, S. Ducruix, and S. Candel, "Experimental investigation of cryogenic flame dynamics under transverse acoustic modulations," *Comptes Rendus Mécanique*, vol. 341, pp. 100–109, Jan. 2013.

[35] X. Petit, G. Ribert, and P. Domingo, "LOx/CH4 mixing and combustion under supercritical conditions," in *51st AIAA Aerospace Sciences Meeting including the New Horizons Forum and Aerospace Exposition*, Aerospace Sciences Meetings, American Institute of Aeronautics and Astronautics, Jan. 2013.

[36] T. Schmitt, Y. Méry, M. Boileau, and S. Candel, "Large-Eddy Simulation of oxygen/methane flames under transcritical conditions," *Proceedings of the Combustion Institute*, vol. 33, no. 1, pp. 1383–1390, 2011.

[37] A. Ruiz, B. Cuenot, L. Selle, and T. Poinsot, "The Flame Structure of a Turbulent Supercritical Hydrogen / Oxygen Flow Behind a Splitter Plate," in *47th AIAA/ASME/SAE/ASEE Joint Propulsion Conference & Exhibit*, (San Diego, California, USA), 2011.

[38] R. Mari, B. Cuenot, F. Duchaine, and L. Selle, "Stabilization mechanisms of a supercritical hydrogen / oxygen flame," in *Proc. of the Summer Program* , (Stanford), pp. 439–448, 2012.

[39] A. Ruiz, T. Schmitt, L. Selle, B. Cuenot, and T. Poinsot, "Effects of the Recess Length of a Coaxial Injector on a Transcritical LO2 / H2 Jet Flame," in *23rd ICDERS*, (Irvine, CA), 2011.

[40] S. Candel, D. Durox, T. Schuller, N. Darabiha, L. Hakim, and T. Schmitt, "Advances in combustion and propulsion applications," *European Journal of Mechanics - B/Fluids*, vol. 40, pp. 87–106, July 2013.

CFD-Simulation of LOX/H2 Injection, Mixing and Combustion at Supercritical Pressures

M. Jarczyk, S. Pohl, H. Müller and M. Pfitzner

Institut für Thermodynamik, Universität der Bundeswehr München, 85577 Neubiberg, Germany

Abstract

The final goal of the work presented here is the development and validation of a multiscale simulation procedure for the calculation of the mixing and combustion processes in a whole rocket combustion chamber. For the flow simulation a LES and a RANS method will be combined. The strongly three-dimensional and turbulent flow phenomena in the near injector region will be captured by LES while the RANS method will be applied in the rest of the combustion chamber for computational efficiency.

Due to the extreme operating conditions in rocket engines regarding propellant temperatures and chamber pressures, a special real gas treatment has to be applied for the prediction of the thermodynamic fluid behavior. Besides the thermodynamic modeling these real gas effects have to be accounted for in the numerical solution algorithm (not discussed here) and the combustion modeling.

A comprehensive numerical framework has been established to simulate reacting flows under conditions typically encountered in rocket combustion chambers. The model implemented into the commercial RANS code ANSYS CFX as well as the open source LES code OpenFOAM includes appropriate real gas relations based on the volume-corrected Peng-Robinson equation of state for the flow field and a real gas extension of a laminar flamelet combustion model.

Section 1 gives detailed information on the numerical and physical modeling established for the flow field and the combustion process. Real gas effects on counterflow diffusion flames as a basis of a flamelet combustion model are discussed in Section 2. Results of the RANS solver validation on the Mascotte [1, 2] test case are shown in Section 3. Section 4 describes the validation of the real gas LES solver on experimental data for pure fluid supercritical injection [3] and a validation of the numerical procedure for non-reacting coaxial H_2/O_2 flows at rocket combustor conditions.

1 Numerical and Physical Modeling

1.1 Governing Equations

The general compressible conservation equations for a multi-component flow can be written as:

$$\frac{\partial \rho}{\partial t} + \frac{\partial (\rho u_j)}{\partial x_j} = 0 \quad (1)$$

$$\frac{\partial (\rho u_i)}{\partial t} + \frac{\partial (\rho u_i u_j)}{\partial x_j} = -\frac{\partial p}{\partial x_i} + \frac{\partial \rho \tau_{ij}}{\partial x_j} \quad (2)$$

$$\frac{\partial \rho h}{\partial t} + \frac{\partial (\rho h u_i)}{\partial x_i} = -\frac{\partial q_i}{\partial x_i} + \frac{Dp}{Dt} \quad (3)$$

$$\frac{\partial \rho Y_\alpha}{\partial t} + \frac{\partial (\rho Y_\alpha u_i)}{\partial x_i} = -\frac{\partial}{\partial x_i} \left(\rho D \frac{\partial Y_\alpha}{\partial x_i} \right) + \dot{\omega}_\alpha \quad (4)$$

Here x_i are cartesian coordinates, t is the time, ρ is the density, u_i is the velocity component in direction i, h is the enthalpy and p is the thermodynamic pressure. τ_{ij} and q_i represent the viscous stress tensor and the heat flux. The mass fraction of species α is denoted by Y_α, D is a diffusion coefficient and $\dot{\omega}_\alpha$ is the species source term due to reaction.

$$\tau_{ij} = \mu \left(\frac{\partial u_i}{\partial x_j} + \frac{\partial u_j}{\partial x_i} - \frac{2}{3}\frac{\partial u_k}{\partial x_k}\delta_{ij} \right) \quad (5)$$

$$q_i = -\lambda \frac{\partial T}{\partial x_i} \quad (6)$$

In LES, a filtering operation is applied before the conservation equations (see 1 - 4) are solved. Only turbulent motions with length scales larger than the filter width are resolved while the subgrid scale (SGS) turbulence has to be modeled. The Smagorinsky model has been applied here. For RANS, a Favre averaging process is adopted in order to derive equations for a time averaged flow solution. In this case all turbulent motions have to be modeled. This is done by a k-ϵ-model in the present study. The thermophysical properties in the above equations, such as the thermal conductivity λ, the dynamic viscosity μ and the density ρ are related to the transported quantities using appropriate real-gas models.

1.2 Thermophysical Modeling

1.2.1 Thermodynamic Properties

The codes that have been used for the present simulations, as well as the combustion model, have been extended by the same thermophysical models. The cubic Peng-Robinson equation of state [4] has been chosen to describe the relation between the thermodynamic state variables.

$$p = \frac{RT}{V - b} - \frac{a(T)}{V^2 + 2Vb - b^2} \quad (7)$$

The molar volume is termed V and R is the universal gas constant. The constants $a(T)$ and b account for attractive forces between the molecules and for the finite volume of the molecules in the fluid. They can be calculated from the critical data T_c and p_c and the acentric factor ω of a substance.

As the Peng-Robinson equation of state is known to provide very good predictions for supercritical temperatures, but significant deviations in transcritical and subcritical regions an empirical correction method established by Harstad et al. [5] has been chosen for the final implementation.

For the critical data of all substances, the values published by Ribert [6] have been applied.

Real gas phenomena also have to be considered in the mixing process of pure components. For this purpose, an extended corresponding states principle has been applied in the present study. The multi-component mixture is assumed to behave like a pure real gas component but with coefficients a, b in the EOS modified appropriately through mixing rules. The mixture properties are also calculated using the PR equation of state with parameters determined from real gas mixing rules. Here, the van der Waals mixing rules [8] [4] have been applied. The binary interaction parameters k_{ij} are set to zero as there were no values available.

$$a = \sum_i \sum_j X_i X_j \sqrt{a_i a_j}(1 - k_{ij}) \quad , \quad b = \sum_i X_i b_i \quad (8)$$

For the final closure of the conservation equations, enthalpy h and constant-pressure specific heat capacity c_p have to be provided. They can be calculated as the sum of an ideal reference (subscript 0) value and a departure function accounting for real gas effects which is calculated consistently from the equation of state.

$$h(T, p) = h_0(T) + \int_{p_0}^{p} \left(V - T \left(\frac{\partial V}{\partial T} \right)_p \right) dp \quad (9)$$

$$c_p(T, p) = c_v(T, p) - \frac{T \left(\frac{\partial p}{\partial T} \right)_V^2}{\left(\frac{\partial p}{\partial V} \right)_T} \quad (10)$$

Species partial specific thermodynamic properties such as the species partial specific enthalpy, needed for the development of the combustion model, can be calculated from the chemical potential η_i as follows:

$$h_i(T, p, X_i) = -\frac{T^2}{M_i} \left(\frac{\partial (\eta_i/T)}{\partial T} \right)_{p, X_i} \quad (11)$$

Here, η_i is defined as $\eta_i(T, p, X_i) = G_{0i}^0(T) + RT \ln(p/p_0) + RT \ln(X_i \varphi_i)$, where G_{0i}^0 is the ideal gas Gibbs free enthalpy of the ith species at reference pressure and φ_i is the fugacity coefficient [4].

1.2.2 Transport properties

Close to the critical point, small changes of state evoke strong variations of the transport properties such that quantities like the thermal conductivity and the dynamic viscosity experience steep gradients. For this reason, an accurate evaluation of the transport properties for both, the pure components and the mixture is of vital importance for a reliable prediction of real gas flows. Within this work, the dynamic viscosity μ as well as the thermal conductivity λ are estimated based on an approach established by Chung [7].

In the calculation of laminar flamelets, molecular diffusion has a significant impact on the flame structure. Therefore a detailed diffusion modeling has been applied in the flamelet combustion model developed in the context of this work.

For the binary diffusion coefficients, the approach proposed by Fuller [8] is used as given in reference [4]. The mixture averaged diffusion coefficient of one component into the mixture is estimated using Bird's law given in [9]. Pressure effects are taken into account by an approach recommended by Takahashi [10]. Species diffusion caused by a temperature gradient (Soret-effect) is taken into account as described in reference [11] and [9]

for the light species H and H_2. Heat diffusion due to concentration gradients (Dufour-effect), however, is neglected in this study.

1.3 Combustion Modeling

1.3.1 Counterflow diffusion flames

The physical configuration employed within this study is the axisymmetric counterflow flame shown schematically in 1. Two opposing jets of fuel and oxidizer create a stagnation plane with a laminar diffusion flame stabilized at the location of stoichiometric mixture fraction. To ensure a reliable prediction of the flame behavior over the entire regime of thermodynamic states, the basic governing equations solved by the combustion simulation laboratory COSILAB [11] are extended by the volume-corrected Peng-Robinson equation of state with appropriate thermodynamic relations and property evaluation schemes.
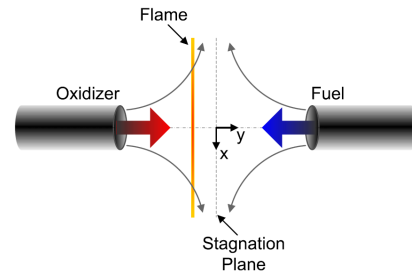
Figure 1: A schematic view of a counterflow diffusion flame configuration

Governing Equations
Along the axis of symmetry, the one-dimensional balance equations for mass, radial momentum, species mass fraction and energy are solved by COSILAB. A detailed description can be found in [12] and [11].

In order to generate flamelet libraries, an additional transport equation is solved for the mixture fraction Z.

$$\rho \frac{\partial Z}{\partial t} = \frac{\partial}{\partial y} \left(\rho D_Z \frac{\partial Z}{\partial y} \right) - \rho v \frac{\partial Z}{\partial y} \quad (12)$$

With the definition of the Lewis number as ratio of thermal to mass diffusivity, the mixture fraction diffusion coefficient D_Z is typically chosen such that the Lewis number of the mixture fraction is equal to unity ($Le_Z = 1$) [13].

$$Le_i = \frac{\lambda}{\rho c_p D_i} \quad (13)$$

1.3.2 Flamelet modeling

In the laminar flamelet model available in ANSYS CFX, the species mean mass fractions are stored in the flamelet library as a function of the mean mixture fractions $\widetilde{Z}$, its variance $\widetilde{Z''^2}$ and the scalar dissipation rate evaluated at stoichiometric conditions $\widetilde{\chi_{st}}$. They can therefore be calculated by weighting the flamelet solution with a statistically independent probability density function $\widetilde{P}$ and integration of the result as follows [14]:

$$\widetilde{Y_i} = \int_0^1 Y_i(Z, \widetilde{\chi_{st}}) \cdot \widetilde{P}(Z) \, dZ \quad (14)$$

$$= \int_0^1 Y_i(Z, \widetilde{\chi_{st}}) \cdot \frac{Z^{a-1}(1-Z)^{b-1}}{\int_0^1 Z^{a-1}(1-Z)^{b-1} \, dZ} \, dZ$$

As shown here, typically a β-function is used as the pdf of the mixture fraction. The parameters a and b are estimated from $a = \widetilde{Z}g$ and $b = (1 - \widetilde{Z})g$ where $g = \widetilde{Z}(1 - \widetilde{Z})/\widetilde{Z''^2} - 1$. The probability density function of the scalar dissipation rate is taken here as the delta function at the conditional Favre mean value $\widetilde{\chi_{st}}$. In CFX, the temperature is not included in the flamelet library but evaluated within the CFD code from the mixture enthalpy.

In order to couple the laminar flamelet solution with the turbulent flow field, the set of Favre-averaged governing equations including mass, momentum and enthalpy has to be supplemented by adding the transport equations for the mean mixture fraction $\widetilde{Z}$ and its variance $\widetilde{Z''^2}$ [14]. The system of equations has to be closed then by applying a suitable turbulence model.

$$\frac{\partial \left(\overline{\rho}\widetilde{Z}\right)}{\partial t} + \frac{\partial \left(\overline{\rho}\ \overline{u_j}\widetilde{Z}\right)}{\partial x_j} = \frac{\partial}{\partial x_j}\left\{\left(\overline{\eta} + \frac{\eta_t}{\sigma_Z}\right)\frac{\partial \widetilde{Z}}{\partial x_j}\right\} \quad (15)$$

$$\frac{\partial \left(\overline{\rho}\widetilde{Z''^2}\right)}{\partial t} + \frac{\partial \left(\overline{\rho}\ \overline{u_j}\widetilde{Z''^2}\right)}{\partial x_j} = \quad (16)$$

$$-\overline{\rho}\tilde{\chi} + \frac{\partial}{\partial x_j}\left\{\left(\overline{\eta} + \frac{\eta_t}{\sigma_{Z''^2}}\right)\frac{\partial \widetilde{Z''^2}}{\partial x_j}\right\} + 2\frac{\eta_t}{\sigma_Z}\left(\frac{\partial \widetilde{Z}}{\partial x_j}\right)^2$$

The scalar dissipation rate χ is a very important quantity since it couples the flamelet solutions with the flow field. With the mixture fraction diffusion coefficient D_Z chosen as thermal diffusivity, the scalar dissipation rate is defined as $\chi = 2D_Z\left(\nabla Z\right)^2$. The mean scalar dissipation rate is modeled by the correlation 17. The coefficient's default setting in CFX is given by $\sigma_Z = 0.9$, $\sigma_{Z''^2} = 0.9$ and $C_\chi = 2$.

$$\tilde{\chi} = C_\chi \frac{\tilde{\epsilon}}{\tilde{k}}\ \widetilde{Z''^2} \quad (17)$$

2 Real gas H_2/O_2 counter flow diffusion flames

The diagrams on the left side of 2 compare the flame profiles resulting for a counter flow diffusion flame using either ideal gas or real gas thermodynamics. The overall influence of the real gas equation of state is limited as the oxygen heats up very rapidly when entering the flame zone.

The right side of 2 shows the effect of diffusion modeling on the real gas flame profiles. Differential diffusion processes (DD) affect the flamelet structure significantly due to the high diffusivity of hydrogen. Special attention has to be payed here to element conservation, which can't be guaranteed locally.

More detailed investigations on the effects of real gas thermodynamics as well as diffusion modeling can be found in [12].

For the combustion modeling in the CFD, flamelet tables have been generated on the basis of the results shown above.

3 Real gas RANS simulation

3.1 Testcase

The RANS code has been validated using the test case RCM-3 presented on the 2nd International Workshop on
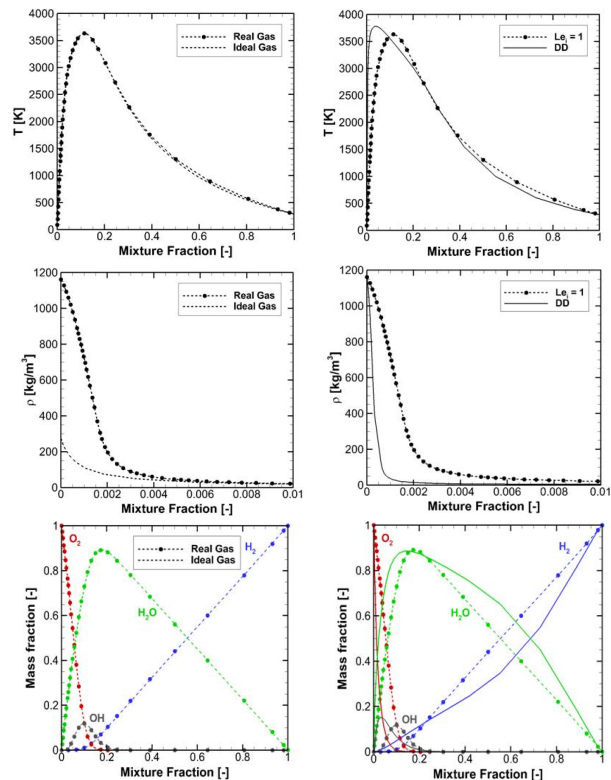
Figure 2: Comparison of flamelet structures for ideal and real gas modeling at $Le_i = 1$, p = 60 bar, as = 1000 s^{-1} (left). Comparison of real gas flamelet structures assuming DD or $Le_i = 1$, p = 60 bar, as = 1000 s^{-1} (right)

Rocket Combustion Modeling [2, 1]. Here a single coaxial injection element is fed with liquid oxygen at 85 K and gaseous hydrogen at 287 K. Pressures up to 100 bar can be achieved in the combustion chamber, representing supercritical conditions for hydrogen and transcritical conditions for oxygen ($T<T_c$). The operating conditions used for the workshop test case are summarized in 1.

The experimental high pressure combustion chamber consists of a square duct of 50 mm inner dimension with a length of 458 mm. For the investigations below the chamber has been modeled rotationally symmetrically with a radius of 28.81 mm, reproducing the internal chamber volume. At the end of the chamber a nozzle has been fitted with a minimum radius of 15 mm in order to avoid backflow at the end of the domain. The injector has been modeled realistically and was given a length of 50 mm to achieve a fully turbulent flow profile. For the simulation a two-dimensional model has been created. The computational grid consists of 200 x 1700 elements (radial x axial direction), providing a grid converged solution.

The inlet boundary conditions were set according to the mass flow rates and temperatures provided by the test case RCM-3 (1). At the outlet a pressure of 60 bar was prescribed. The walls of the chamber have been assumed to be smooth and adiabatic. The steady state flow field has been solved using the ANSYS CFX high resolution scheme, blending between first and second order accuracy in space in order to avoid oscillations in the flow field at an improved accuracy compared to a simple first order scheme.

Table 1: Boundary conditions for the Mascotte test case [1, 2]

Operating Conditions	H2	O2
Pressure, bar	60	60
Temperature, K	287	85
Massflow, kg/s	0.07	0.1

3.2 Results

3 compares the flame resulting for flamelet libraries without differential diffusion ($Le_i = 1$) and libraries considering DD in the calculation of the counter flow diffusion flames within the thin flame front and neglecting it elsewhere ($Le_i, Le_i = 1$).

Small differences in the temperature distribution can be found in the near injector region of the flame (not shown here). In this area the OH distribution resulting from the libraries with DD lies significantly above the results without DD. The overall flame shape however is almost not affected by considering DD effects.
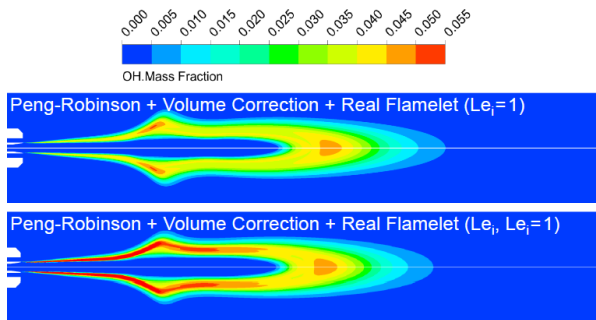
Figure 3: Comparison of OH mass fraction distribution for different real gas flamelet libraries applied along with the laminar flamelet combustion model

The OH distribution resulting from the CFD is compared to experimental results [1] in 4. Generally the flame predicted by the CFD is a little longer than in the experiment. Also the radial expansion of the flame is slightly overpredicted by the CFD. The overall flame shape however matches very well. Applying the mixed flamelet library, a good agreement is achieved for the OH concentration within the thin flame front downstream of the injector, which can't be reproduced without DD.

A comprehensive discussion of real gas RANS investigations can be found in [12] and [15].

4 LES Simulation

4.1 N2-Jet-Validation

4.1.1 Testcase

For a validation of the new OpenFOAM LES solver for trans- and supercritical jet flow, configurations representing the injection of liquid, cold nitrogen (LN2) into gaseous nitrogen (GN2) at ambient temperature have been chosen, where experimental data are available [3]. Here several combinations of injection temperature and velocity as well as chamber pressure have been studied experimentally. Three near critical cases (2) have been chosen for the validation of the real gas LES solver.
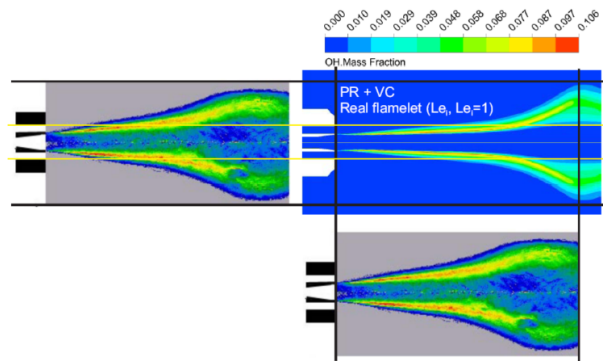
Figure 4: Experimentally measured OH* distribution [1, 2] compared to CFD simulations applying different real gas flamelet libraries

Table 2: Initial and boundary conditions for trans- and supercritical jet flows [3]

Testcases	Case 3	Case 4	Case 7
Jet velocity, m/s	4.9	5.4	4.5
Jet temperature, K	126.9	137	126.2
Chamber pressure, bar	39.7	39.7	50.1
Chamber temperature, K	298	298	298

The experimental mixing chamber is a square duct of 60x60 mm with a length of about one meter. The injector has a diameter of 2.2 mm and a length that assures a fully turbulent pipe flow at the injector exit. The numerical setup for the jet investigations has been chosen following Schmitt et al.[16]. The injector diameter is identical to the experiment and the chamber was given a length of 250 mm. In the numerical modeling, the mixing chamber has been assumed to be rotationally symmetric with a diameter of 122 mm. The geometry has been discretized using an O-grid with a total number of cells of about 1.7 million. The grid has been refined near the injector region, where the cell size is between 0.1 mm and 0.15 mm.

2 summarizes the initial and boundary conditions according to the chosen experimental setups. At the inlet a constant temperature combined with a time varying fully turbulent velocity profile has been prescribed, which has been extracted from an incompressible turbulent pipe flow. The chamber front wall has been assumed to be adiabatic and the outer chamber walls were given a constant temperature of 298 K. A wave transmissive boundary condition has been chosen for the outlet.

4.1.2 Results

On the left hand side of 5 snapshots of the density gradient magnitudes are shown. The isolines refer to the arithmetic mean density between the injector exit and the surrounding nitrogen ($\rho_{iso} = 0.5(\rho_{inj} + \rho_\infty)$) and illustrate the jet break-up. The two cases with injection temperatures below the pseudo-boiling temperature (Case 3 and Case 7) are characterized by a sharp density gradient that encloses the cold jet. The large density ratio between jet core and surrounding hinders the formation of Kelvin-Helmholtz vortices [16] and therefore delays the jet break-up. While for Case 4 coherent vor-

Table 3: Boundary conditions for the simulation of a non-reacting mixing process for the Mascotte configuration A-60 [1, 2].

Operating Condition	H2	O2
Pressure, bar	60	60
Temperature, K	287	85
Velocity, m/s	250	5

tices evolve close to the injector eventually leading to break-up, the jet surface stays rather smooth in this section for Case 3 and Case 7. On the right hand side the time-averaged density profiles on the symmetry axis are compared with the experimental data. All three cases are in excellent agreement with the experiments. Minor deviations can be observed in the region of jet break-up ($20 < x/R < 40$) for the transcritical cases 3 and 7 where the steep density decrease is not fully captured. The simulations for the supercritical Case 4, however, match the experiments particularly well.
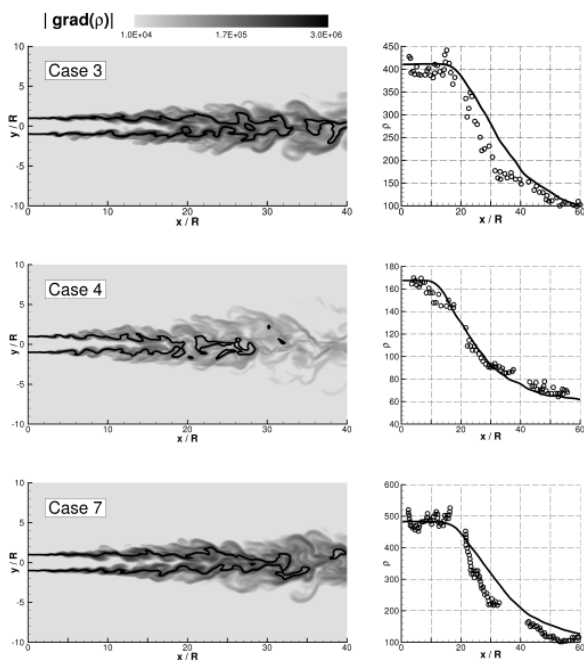
Figure 5: Magnitude of the density gradients for Case 3, Case 4 and Case 7. The black isoline denotes the arithmetic mean density between inlet and ambient nitrogen (left). Mean density profiles along the axisymmetric axis. ∘ Mayer et al., – OpenFOAM (right)

A more detailed discussion of the LES of non-reacting real gas flows can be found in [17] and [18].

4.2 H2-LOX-LES-Jet

4.2.1 Testcase

The boundary conditions for the non-reacting LES simulation of a H_2/O_2 coaxial injector are chosen according to the 'Proceedings of the 2nd International Workshop on Rocket Combustion Modeling' [2], like in Section 3.1.

For the CFD the combustion chamber is modeled again axially symmetric with a diameter of 50 mm and a length of 75 mm. For the correct reproduction of turbulent motion in the flow field a three dimensional model is created here. The detailed injector geometry has been neglected for the simulations shown below and the inlet boundary conditions are prescribed directly at the chamber entrance. The domain is discretized with a hexahedral O-grid of 1.5 million elements. In the near injector region the grid is refined to an element size of 0.1 mm to 0.15 mm.

3 summarizes the boundary conditions chosen for the simulations discussed below. A constant temperature and a constant velocity have been prescribed at the inlet boundaries. The chamber walls have been defined to be adiabatic. For the outlet a constant pressure boundary of 60 bar has been chosen.

4.2.2 Results

Due to the high density ratio ($\rho_{O_2}/\rho_{H_2} > 250$) and the large difference in injection velocity, this test case is a challenge for the numerical solver stability. Therefore this setup serves as a validation for the real gas capability of the applied numerical method.

Experimental data for the validation of a non-reacting coaxial injection of the Mascotte configuration is not yet available, but assumed to be generated in near future by the means of DNS in a cooperation with Technische Universität München (TUM).

The developed real gas LES solver showed a reasonable stability and the inert H_2/O_2 flow could be simulated successfully. 6 shows an instantaneous distribution of the density gradient magnitude. As expected there can be found a very steep density gradient in the mixing zone of the very cold oxygen core and the warm hydrogen coflow. As already investigated for the N_2 jet configurations, this strong gradient delays the jet breakup significantly.
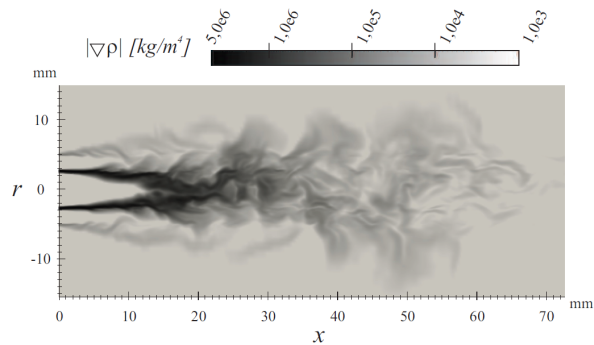
Figure 6: Instantaneous distribution of density gradient magnitude

Figure 7: Density iso-surface ρ=30 kg/m^3

7 shows an iso surface of the density at ρ=30 kg/m^3. In this condition the cold oxygen core is already strongly heated up and is therefore strongly disturbed by the hydrogen coflow. Like it is known from experimental investigations [19] the jet breaks up by separation of dense pockets from the cold oxygen core.

On the basis of the successful calculation of this non-reacting flow configuration the LES solver has been extended by a real gas flamelet model [20] and will be validated against experimental data in due time.

5 Conclusions

A comprehensive numerical framework has been established to simulate reacting flows under rocket engine conditions.

The real gas RANS solver has been successfully validated for reacting transcritical flows at the Mascotte flame [1, 2]. The general flame shape could be reproduced very well by the CFD, although the overall flame dimensions are slightly overpredicted. Considering differential diffusion effects in the combustion modeling, also the experimentally determined OH distribution could be predicted realistically.

The real gas LES code showed a very good accuracy in the prediction of non-reacting trans- and supercritical flows. Experimental results of cold nitrogen injection at elevated pressures [3] could be reproduced in perfect agreement. The solver could also be successfully tested for stable performance at coaxial injection of H_2 and O_2 at rocket combustor conditions.

In the near future, the real gas Flamelet model will be validated for LES applications at the Mascotte test case.

Finally a multi scale simulation of a whole rocket combustion chamber will be performed on the basis of these developments.

Acknowledgment

References

[1] S. Candel, G. Herding, R. Snyder, P. Scouflaire, C. Rolon, L. Vingert, M. Habiballah, F. Grisch, M. Péalat, P. Bouchardy, D. Stepowski, A. Cessou, and P. Colin, "Experimental Investigation of Shear Coaxial Cryogenic Jet Flames," *J. Prop. Pow.*, vol. Vol. 14 (5), pp. 826–834, 1998.

[2] M. Habiballah and S. Zurbach, "Test Case RCM-3, Mascotte single injector," in *Proceedings of the 2nd International Workshop on Rocket Combustion Modeling, Lampoldshausen, Germany*, 2001.

[3] W. Mayer, J. Tellar, R. Branam, G. Schneider, and J. Hussong, "Raman measurement of cryogenic injection at supercritical pressure.," *Heat and Mass Transfer*, vol. Vol. 39, pp. 709–719, 2003.

[4] B. E. Poling, J. M. Prausnitz, and J. P. O'Connell, *The Properties of Gases and Liquids*. Mc Graw Hill, 2. ed., 2004.

[5] K. Harstad, R. S. Miller, and J. Bellan, "Efficient High-Pressure State Equations," *AIChE Journal*, vol. Vol. 43(6), pp. 1605–1610, 1997.

[6] G. Ribert, N. Zong, V. Yang, L. Pons, N. Darabiha, and S. Candel, "Counterflow diffusion flames of general fluids: Oxygen/hydrogen mixtures.," *Comb. and Flame*, vol. 154, pp. 319–330, 2008.

[7] T.-H. Chung, M. Ajlan, L. L. Lee, and K. E. Starling, "Generalized Multiparameter Correlation for Nonpolar and Polar Fluid Transport Properties.," *Ind. & Eng. Chem. Res.*, vol. 27(4), pp. 671–679, 1988.

[8] E. Fuller, P. Schettler, and J. Giddings, "A new method for prediction of binary gas-phase diffusion coefficients.," *Industrial and Engineering Chemistry*, vol. 58(5), pp. 19–27, 1966.

[9] R. Kee, G. Dixon-Lewis, J. Warnatz, M. Coltrin, and J. Miller, "A Fortran Computer Code Package for the Evaluation of Gas-Phase, Multicomponent Transport Properties," *SAND86-8246.*, 1986.

[10] S. Takahashi, "Preparation of a generalized chart for the diffusion coefficients of gases at high pressures.," *J. Chem. Eng. Japan*, vol. 7(6), pp. 417–420, 1974.

[11] *COSILAB, Rotexo Software. Bochum 2011.*

[12] S. Pohl, M. Jarczyk, M. Pfitzner, and B. Rogg, "Real gas CFD simulations of hydrogen/oxygen supercritical combustion," *EUCASS Book of Selected Papers Vol. 4 Propulsion Physics*, vol. 4, pp. –, 2011.

[13] H. Pitsch and N. Peters, "A consistent flamelet formulation for non-premixed combustion considering differential diffusion effects.," *Comb. and Flame*, vol. 114(1-2), pp. 26–40, 1998.

[14] *CFX Software Package. Version 12.1, ANSYS Germany 2009.*

[15] M. Poschner and M. Pfitzner, "CFD-Simulation of the injection and combustion of LOX and H2 at supercritical pressures," in *AIAA-2010-1144, 48th AIAA - Aerospace Sciences Meeting*, 2010.

[16] T. Schmitt, L. Selle, B. Cuenot, and T. Poinsot, "Large-Eddy Simulation of transcritical flows," *Comptes rendus mécanique*, vol. Vol. 337, pp. 528–538, 2009.

[17] H. Mueller, C. A. Niedermeier, M. Jarczyk, M. Pfitzner, S. Hickel, and N. Adams, "Large Eddy Simulations of Trans- and Supercritical Injection," in *5TH European Conference for Aeronautics and Space Sciences (EUCASS)*, 2013.

[18] M. Jarczyk and M. Pfitzner, "Large Eddy Simulation of Supercritical Nitrogen Jets," in *Proceedings of the 50th AIAA Aerospace Science Meeting, AIAA-2012-1270*, 2012.

[19] M. Oschwald, J. J. Smith, R. Branam, J. Hussong, A. Schik, B. Chehroudi, and D. Talley, "Injection of Fluids into Supercritical Environments," *Comb. Sci. and Tech.*, vol. Vol. 178, pp. 49–100, 2006.

[20] H. Mueller, F. Ferraro, and M. Pfitzner, "Implementation of a Steady Laminar Flamelet Model for non-premixed combustion in LES and RANS simulations," in *8th International OpenFOAM Workshop, June 11-14 2013, Jeju, Korea*, 2013.

Full-Scale Apartment Fire Tests ('Rabot2012') in the Context of Fire Forecasting

T. Beji[1], S. Verstockt[2] and B. Merci[1]

[1] *Dept. of Flow, Heat and Combustion Mechanics, Ghent University - UGent (Belgium)*

[2] *Multimedia Lab, Dept. of Electronics and Information Systems, Ghent University - iMinds (Belgium)*

Abstract

This paper briefly describes a series of multi-compartment full-scale fire tests in an apartment located in a building in Ghent (Belgium), called the 'Rabot' tower. It is illustrative for the intense collaboration between two departments at Ghent University, combining strong expertise in combustion and fire dynamics on the one hand (Dept. of Flow, Heat and Combustion Mechs.) and on video data analysis on the other hand (Multimedia Lab - ELIS - iMinds) [1-6]. The 'Rabot' tests provide a set of valuable experimental data for testing of fire models (CFD and two-zone), as well as for testing monitoring of the fire. The fuel is of intermediate complexity and the ignition location has been chosen such that the initial flame spread can be followed. Measurement equipment includes thermocouple trees and velocity probes, as well as multi-view video footage (to which Video Fire Analysis, VFA, is applied through smoke and flame detection algorithms). The experimental set-up is described first, followed by a brief overview of the fire scenarios obtained in the four tests. Data processing in the context of fire forecasting is discussed as well. The entire data set is found on `http://multimedialab.elis.ugent.be/rabot2012/`

Introduction

During the past few years, fire forecasting has received more and more attention. Such forecasting is very interesting for e.g. fire services approaching the scene, so they can be assisted in their evaluation as to whether the situation is safe or not (and whether it will remain safe during the next minutes, depending on their actions). In [2] we describe how the use of real-time video data can be very beneficial for the quality and reliability of fire forecasting in a single compartment enclosure. The aspect 'Data Assimilation' (DA) is essential in this work. In laboratory tests, temperature measurements can be used for DA, but in real-life situations this is obviously not the case. However, in many complex buildings, security cameras are in place. The basic idea is therefore to apply smoke and flame detection algorithms to video footage of the fire scene. Reconstructing the flame/fire size can provide an estimate for the fire dimensions and heat release rate (HRR). This is then an important input parameter for the fire model. For the sake of forecasting, where positive lead times are required, CFD is too slow and two-zone models are more feasible.

In [2] the situation was simplified in that only a single compartment was studied, with the video camera positioned outside with a good view on the doorway. Below, we describe that this is no longer the case in the Rabot2012 tests. These tests are described next and finally some conclusions are drawn. The entire data set is found on `http://multimedialab.elis.ugent.be/rabot2012/`

Use of video data for fire forecasting

The use of real-time data from monitoring is indispensible in the context of fire forecasting. Using our multi-view fire analysis framework [1], which gives real-time information about the state of the environment, it should be able to improve and accelerate model-based predictions of the future state. By combining the information about the fire from models and real-time data, an estimate of the fire can be produced that is better than could be obtained from using the model or the data alone. This is the multi-disciplinary win-win of our approach. In the Rabot2012 tests, both the flame spread and smoke layer height are monitored by a set of cameras with different positions and viewpoints. In order to follow the temporal evolution of the flame height and spread, we extract the flame pixels from the consecutive video images. First, we perform a histogram based segmentation of the brightest objects using automatic thresholding. Subsequently, our low-cost flame feature analysis (consisting of bounding box disorder analysis and saturation maximization) filters out non-fire pixels and performs the flame segmentation. Finally, from the resulting flame objects, we can measure the distance to the ignition point in the three directions.

For the video-based estimation of the smoke layer height, we start from our single view fire analysis technique proposed in [8]. A commonly used technique for the determination of the smoke layer interface height [6], which relies on the second derivative of the temperature profile, was translated into a novel video analysis approach. By focusing on the change in image detail, i.e., the image energy, we are able to detect the smoke layer interface hint for each single camera. Furthermore, since we have multiple cameras monitoring the scene from different viewpoints, we can perform a more accurate/detailed analysis of hint. By focusing on the within- and between-variance of all multi-view hint estimations, a better (global) estimate of the smoke layer height is achieved.

a) Test 1 and 3

b) Test 2 and 4
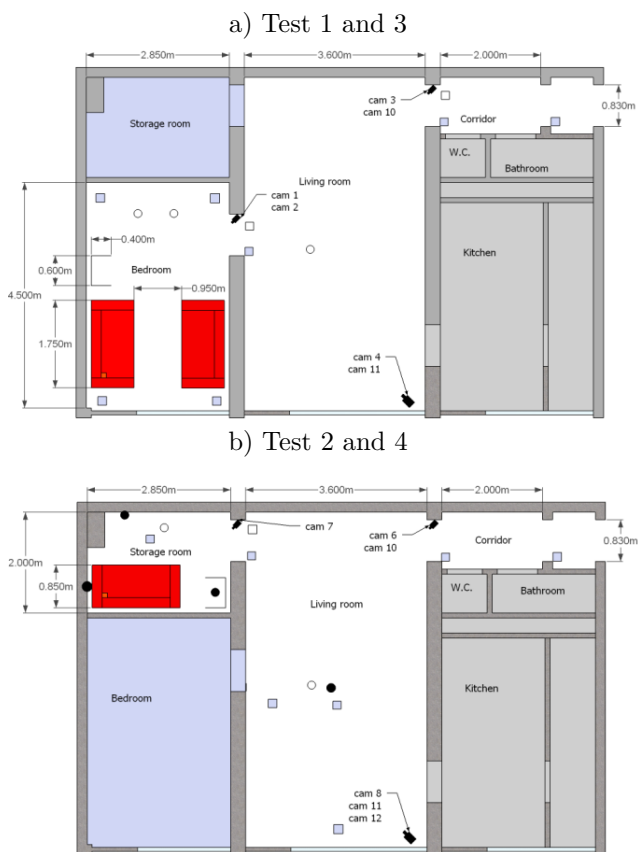
Figure 1: Top view sketch of apartment lay-out with furniture. Solid squares: thermocouple trees; open squares: bi-directional velocity probe trees; open circles: Gardon gauges; solid circles: copper plates; black symbols at the doorways and near the window of the living room: video cameras. The ignition source location is indicated by the small square on the sofa

Figure 2: Experimental profiles of smoke interface height evolution at the doorways between the fire room, the living room, the corridor and the outside for Tests 1 and 2

Rabot2012 tests: Set-up

The apartment consists of a storage room, a bedroom, a living room, a W.C., a bathroom, a kitchen and a corridor (Fig. 1). Two rooms have been used as 'fire' rooms: the bedroom in Tests 1 and 3 ($2.7m \times 4.4m \times 2.5m$) and the storage room in Tests 2 and 4 ($2.7m \times 2.0m \times 2.5m$). The entry to the kitchen has been sealed with a fire resistant panel for all four tests. The doors to the W.C. and bathroom were closed during all tests. The entrance to the apartment and the exit to the stairs were completely open. In Tests 1 and 3, the door to the living room was open and the door of the storage room was closed. In Tests 2 and 4, it was the other way around.

The ceiling consists of a 2 cm thick gypsum plasterboard on a 30 cm thick concrete slab. The wall linings consist of thin wall paper, 2 cm thick gypsum plasterboard, 3 cm thick fibre insulating board, and a 30 cm brick layer. The floor covering in the rooms is vinyl layer on a 30 cm thick concrete slab. The fuel packages consist of funiture items: identical sofas (polyurethane covered with a fabric) and identical bookshelves made of wood and filled with paper items of different densities.

The fire was ignited with a lighter and six small wooden cribs, soaked in heptane and placed in one corner of the first sofa. The initial flame spread over

the sofa could then be monitored with the video camera at the doorway. From the modelling perspective, the challenge is to predict this flame spread and the subsequent occurrence (or not) of secondary and tertiary ignition. If secondary (and/or tertiary) ignition occurs, it is also important to predict at what time this happens.

Additional calorimetry tests were performed in the lab at WFRGent, as support tests for characterization of the fuel load (i.e. HRR profiles of each of the burning items) in free-burn conditions (i.e. open atmosphere). Video Fire Analysis (VFA) has also been performed for these tests, monitoring flame spread and flame height with the flame detection algorithm. Furthermore, a small-scale calorimetry test has been performed on a sample of flexible polyurethane foam of 0.0088 m^2, taken from one of the sofas.

Rabot2012 tests: Scenarios

A brief chronological description of each of the four fire scenarios is provided here. Ignition time is taken as time t = 0 s.

In Test 1, 50 seconds after ignition, light smoke was escaped through the doorway into the living room. Thick black smoke filled the upper part of the bedroom and the living room within 2 min 15 s. Smoke was observed at the end of the entry corridor from around

t = 3 min 30 s onward. Flames covered half of the sofa after approx. 5 min 30 s after ignition. At t = 9 min 30 s the flame front reached the opposite corner of the sofa. The burning became more intense with a highly luminous flame. The bookshelf ignited and was completely engulfed in fire at t = 14 min. The intense simultaneous burning of the first sofa and the bookshelf resulted in a substantial heat build-up. The second sofa ignited at t = 16 min. Cracks were observed in the outside window and small pieces fell out just before complete breakage of the window at t = 30 min. The decay stage of the fire started at about t = 37 min.

In Test 2, the fire was confined to the sofa for about 7 to 8 minutes. At 5 min after ignition an oscillating layer of thick black smoke was formed in the living room. The amplitude of the oscillations became particularly high starting from 8 min 30 s. At 10 min 30 s after ignition continuous external flaming was recorded during 6.5 minutes. The intensity of external burning (size of external flames) reached its maximum value at around 11 min 30 s. The decay stage of the fire started at around 25 min. Test 3 was conducted in the same configuration as Test 1 (same fire room and furniture layout).

However, the walls and ceiling linings and the floor covering had suffered from damage after Test 1. As a result, the thermal boundary conditions of the enclosure are not identical. The initial flame spread stage could be observed up to 5 minutes after ignition. Then, due to the build-up of a layer of black thick smoke in the bedroom and the living room, the flame was not visible in the video footage anymore up to t = 14 min. The burning intensified and the flame became very luminous, reaching the opposite corner of the sofa at approx. t = 15 min 30. The bookshelf ignited by flame impingement and was completely engulfed in fire at t = 30 min. By that time the sofa was almost totally burnt. In contrast to Test 1, the two items did not burn simultaneously and the second sofa did not ignite. The fire decay started at 39 min 30 s. In Test 4, the configuration is the same as for Test 2. However, again the walls and ceiling linings and the floor covering had been damaged after Test 2 and the thermal boundary conditions of the enclosure are therefore not identical. The fire was confined to the sofa for approx. 7 to 8 minutes. The bookshelf was engulfed in fire shortly thereafter. The smoke layer in the living room started to oscillate strongly at 8 min. External flaming was observed only during a relatively short period of time (from 13 min 30 s to 15 min) and with a lower intensity. The decay stage started at 27 min 30 s.

Rabot2012 tests: Some results

Only some temperature results and video-based estimations of the smoke layer height are discussed here. A more detailed discussion is found in [9, 10].

Temperature measurements in the doorways can be used to calculate the neutral plane height, the upper layer temperature and the lower layer temperature for all compartments (i.e. fire room, living room and corridor). This is very relevant in the framework of zone modelling. Figure 2 shows some results for Tests 1 and 2.

As expected, the neutral plane height is the lowest between the fire room and the living room. It is about
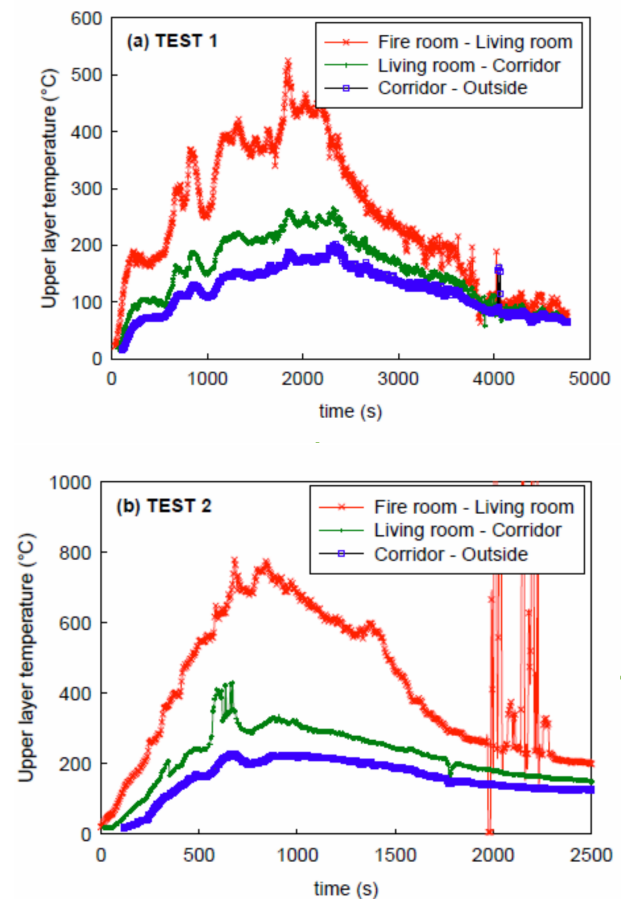
Figure 3: Experimental profiles of upper layer temperature at the doorways between at the doorways between the fire room, the living room, the corridor and the outside for Tests 1 and 2

25 cm higher in the door 'living room-corridor' and 50 cm higher in the door 'corridor-exterior'.

Figure 3 shows the calculated experimental profiles of upper layer temperature at the doorways. These results are in line with the fire scenarios as described. The most severe fire occurs in Test 2, as indicated by the highest upper layer temperature at the exit of the fire room (around 780 $°C$), with substantial external burning.

Video-based estimations of the smoke interface height for TEST1 and TEST2 are shown in Figure 4. In each of the tests, two cameras with a different position and field of view were used to monitor the living room. By focusing on the between-variance of the camera hint estimations, a better (global) estimate of the smoke layer height is achieved. Figure 4a (TEST1), for example, shows that the average hint of CAM3 and CAM4 already separate at t=130s. This can be an indication that it is not safe anymore to trust the cameras. Contrary, in Figure 4b (TEST2) we see that the estimations of CAM6 and CAM8 closely follow each other, indicating that their estimations can be trusted with high(er) probability.

The reason for having a closer fit of the camera measurements in TEST2 compared to TEST1 can be found in the fact that we lowered the cameras beneath the smoke layer after TEST1. In this way, we could decrease the noise caused by smoke and prolong the
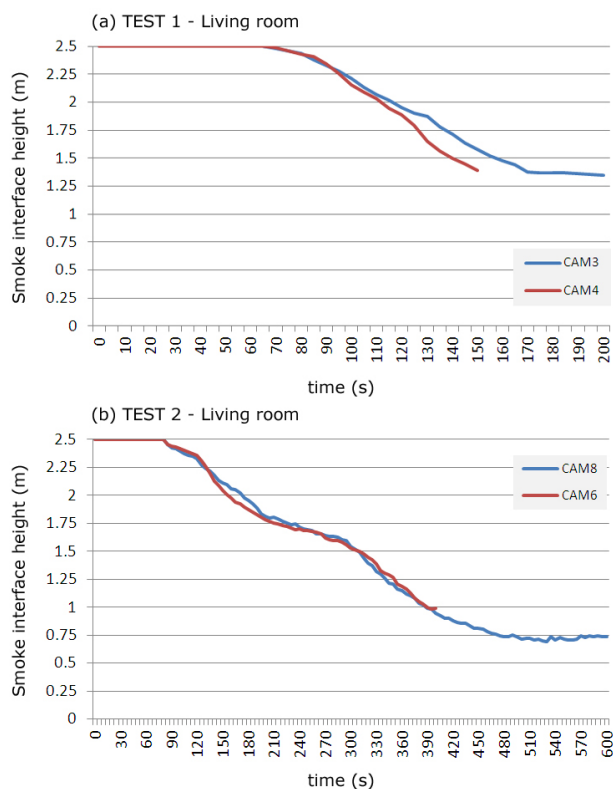
Figure 4: Video-based estimations of smoke interface height in the living room for Tests 1 and 2

video monitoring time. This has, of course, an impact on the practical applicability of the cameras in other applications (e.g., video surveillance). However, to study/forecast the fire evolution in real-time, it has proven to be far more effective.

Finally, it is important to remark that subjective evaluation of the video-based estimation of the smoke layer height with the temperature profiles in Figure 2 shows that the proposed approach is effective in detecting the smoke layer height. It can be seen that the trend of the video-based estimation(s) of hint in the living room follow the trend of the temperature measurements at the living room doors.

Conclusions

The paper illustrates the value of fruitful collaboration between a department with expertise in combustion and fire dynamics and a department within expertise in video data analysis. The specific case at hand is the multi-compartment full-scale ('Rabot') fire tests. These offer a comprehensive experimental dataset, useful to examine several aspects of enclosure fire dynamics. The fuel package (two or three realistic furniture items) is of intermediate complexity, making the tests tractable for modelers.

Regarding the fire monitoring aspect, the Video Fire Analysis (VFA) in real practical applications has been described. The VFA results are promising.

From the modeling viewpoint, the variety of scenarios, including flame spread over a sofa, the influence of the thermal boundary conditions, external flaming, multi-compartment heat and smoke spread, etc., is appealing. Finally, it has been explained that the data will

be used for fire forecasting purposes. The entire data set is found on `http://multimedialab.elis.ugent.be/rabot2012/`.

Acknowledgments

References

[1] S. Verstockt, S. Van Hoecke, N. Tilley, B. Merci, B. Sette, P. Lambert, C.-F. J. Hollemeersch and R. Van de Walle, "FireCube: A Multi-View Localization Framework for 3D Fire Analysis", Fire Safety Journal, Vol. 46 (5), pp. 262 - 275 (2011).

[2] T. Beji, S. Verstockt, R. Van de Walle and B. Merci, "On the Use of Real-Time Video to Forecast Fire Growth in Enclosures", Fire Technology (available online). DOI: 10.1007/s10694-012-0262-0

[3] T. Beji, S. Verstockt, R. Van de Walle and B. Merci, "Analysis of data assimilation based numerical simulations for prediction of smoke filling in large spaces", Journal of Fire Sciences, Vol. 30 (4), pp. 300 - 317 (2012).

[4] S. Verstockt, C. Poppe, S. Van Hoecke, C. Hollemeersch, B. Merci, B. Sette, P. Lambert, R. Van de Walle, "Silhouette-based multi-sensor smoke detection - Coverage analysis of moving object silhouettes in thermal and visual registered images", Machine Vision and Applications, Vol. 23, pp. 1243 - 1262 (2012).

[5] S. Verstockt, T, Beji, P. De Potter, S. Van Hoecke, B. Sette, B. Merci, R. Van de Walle, "Video driven fire spread forecasting (f)using multi-modal LWIR and visual flame and smoke data", Pattern Recognition Letters, Vol. 34 (1), pp. 62 - 69 (2013).

[6] S. Verstockt, S. Van Hoecke, T. Beji, B. Merci, B. Gouverneur, A. E. Cetin, P. De Potter, R. Van de Walle, "A multi-modal video analysis approach for car park fire detection", Fire Safety Journal, Vol. 57, pp. 44 - 57 (2013).

[7] N. Tilley, P., Rauwoens, B., Merci, "Verification of the accuracy of CFD simulations in small-scale tunnel and atrium fire configurations," Fire Safety Journal Vol. 46(4), pp. 186-193 (2011).

[8] T. Beji, S. Verstockt, R. Van de Walle and B. Merci, "Characterization of the Multi-compartment Full-Scale ('Rabot') Fire Tests", Experimental Thermal and Fluid Science (submitted).

[9] T. Beji, S. Verstockt, R. Van de Walle and B. Merci, "Characterization of the Multi-compartment Full-Scale ('Rabot') Fire Tests", Experimental Thermal and Fluid Science (submitted).

[10] S. Verstockt, T. Beji, B, Merci and R. Van de Walle, "RABOT2012 - Presentation of a Mult-View Video Dataset of the Full-Scale ('Rabot') Fire Tests", 7th International Seminar on Fire and Explosion Hazards, pp. 58-66 (2013).

ERCOFTAC Workshops and Summer Schools

Title	Location	Date	Organisers	Email addresses
4th Workshop on Turbulent Combustion Sprays	Cesme-Izmir, Turkey	8/09/2013	Gutheil, E. Masri, A.	gutheil@iwr.uni-heidelberg.de assaad.masri@sydney.edu.au
Fractal Flow Design - How to design bespoke turbulence and why?	Udine, Italy	9/09/2013 – 13/09/2013	Vassilicos, J.C.	cism@cism.it
Buoyancy Driven Mixing	Cambridge, UK	26/09/2013 - 27/09/2013	Woods, A.	andy@bpi.cam.ac.uk
Biological Fluid Mechanics - course	Delft, The Netherlands	?/10/2013	Poelma, Ch. van de Vosse, F.	c.poelma@tudelft.nl
ERCOFTAC Technologietag Süd- und Norddeutschland	Erlangen, Germany	11/10/2013	Becker, S.	ws@ipat.uni-erlangen.de
Mathematical Methods and Tools in Uncertainty Management and Quantification	Paris, France	24/10/2013 - 25/10/2013	Hirsch, C.	richard.seoud-ieo@ercoftac.org
J M Burgers Centre Course on Combustion	Eindhoven, The Netherlands	29/10/2013 - 1/11/2013	De Goey, L.P.H Van Oijen, J.A. Roekaerts, D	l.p.h.d.goey@tue.nl j.a.v.oijen@tue.nl d.j.e.m.rokaerts@tuedelft.nl
Best Practice For Engineering CFD II	Amsterdam, The Netherlands	14/11/2013-15/11/2013	Hirsch, C.	richard.seoud-ieo@ercoftac.org
Flow Control Technologies	Cranfield, UK	9/12/2013-10/12/2013	Choi, K-S.	richard.seoud-ieo@ercoftac.org
10th International ERCOFTAC Symposium on Engineering Turbulence Modelling and Measurements	Marbella, Spain	17/09/2014 - 19/09/2014	Leschziner, M. Rodi, W.	fgarcia@eventisimo.com
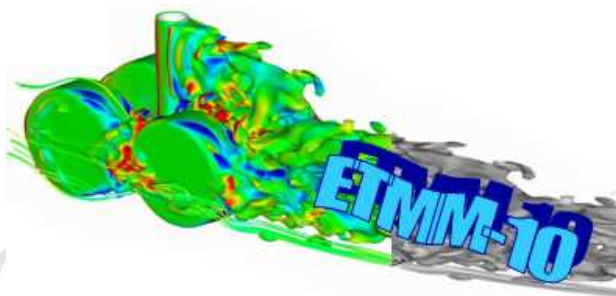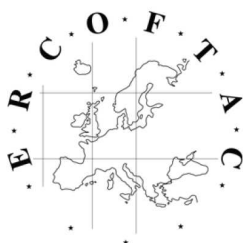
ETMM 10

10th International ERCOFTAC Symposium on
Engineering Turbulence Modelling and Measurements

17 - 19 September 2014
Don Carlos Resort, Marbella, Spain

Symposium website: www.etmm10.info

Organizers
Prof. Michael Leschziner, Chairman, Imperial College
Prof. Wolfgang Rodi, Co-chairman, Karlsruhe Institute of Technology
The ETMM Series of Conferences

Aims

The ETMM series of symposia aims to provide a bridge between researchers and practitioners in Flow,Turbulence and Combustion by reporting progress in the predominantly applied, industrially-oriented areas of turbulence research.This includes the development, improvement and application of statistical closures, simulation methods and experimental techniques for complex flow conditions that are relevant to engineering practice; the modelling of interactions between turbulence and chemistry, dispersed phases and solid structures; and the symbiosis of modelling, simulation and experimental research.

Major Themes

- Novel modelling and simulation methods for practically relevant turbulent flows, including interaction with heat and mass transfer, rotation, combustion and multi-phase transport
- Novel experimental techniques for flow, turbulence and combustion and new experimental studies and data sets
- Innovative applications of modelling, simulation and experimental techniques to complex flows, industrial configurations and optimisation problems
- High-speed aerodynamics, acoustics and flow control with emphasis on turbulence processes
- Modelling, simulation and measurements of environmental and bio-spherical flows

Abstracts are invited for submission by **15th January 2014**, via the Symposium Website.
Final manuscripts and updated abstracts are due by **1st July 2014**.

ERCOFTAC Special Interest Groups

1. Large Eddy Simulation
Geurts, B.J.
University of Twente, Holland.
Tel: +31 534 894 125
b.j.geurts@utwente.nl

4. Turbulence in Compressible Flows
Dussauge, Jean-Paul
IUSTI, Marseille
jean-paul.dussauge
@polytech.univmrs.fr

5. Environmental Fluid Mechanics
Armenio, V.
Universit di Trieste, Italy.
Tel: +39 040 558 3472
Fax: +39 040 572 082
armenio@dica.units.it

10. Transition Modelling
Dick, E.,
University of Ghent, Belgium.
Tel: +32 926 433 01
Fax: +32 926 435 86
erik.dick@ugent.be

12. Dispersed Turbulent Two Phase Flows
Sommerfeld, M.
Martin-Luther University, Germany.
Tel: +49 346 146 2879
Fax: +49 346 146 2878
martin.sommerfeld@iw.uni-halle.de

14. Stably Stratified and Rotating Flows
Redondo, J.M.
UPC, Spain.
Tel: +34 934 017 984
Fax: +34 934 016 090
redondo@fa.upc.edu

15. Turbulence Modelling
Jakirlic, S.
Darmstadt University of Technology, Germany.
Tel: +49 615 116 3554
Fax: +49 615 116 4754
s.jakirlic@sla.tu-darmstadt.de

20. Drag Reduction and Flow Control
Choi, K-S.
University of Nottingham, England.
Tel: +44 115 951 3792
Fax: +44 115 951 3800
kwing-so.choi@nottingham.ac.uk

24. Variable Density Turbulent Flows
Anselmet, F.
IMST, France.
Tel: +33 491 505 439
Fax: +33 491 081 637
anselmet@irphe.univ-mrs.fr

28. Reactive Flows
Angelberger, C.
IFP Energies Nouvelles, France
Tel: +33 147 527 420
christian.angelberger@ifpen.fr

32. Particle Image Velocimetry
Stanislas, M.
Ecole Centrale de Lille, France.
Tel: +33 320 337 170
Fax: +33 320 337 169
Michel.Stanislas@ec-lille.fr

33. Transition Mechanisms, Prediction and Control
Hanifi, A.
FOI, Sweden.
Tel: +46 855 503 197
Fax: +46 855 503 397
ardeshir.hanifi@foi.se

34. Design Optimisation
Giannakoglou, K.
NTUA, Greece.
Tel: +30 210 772 1636
Fax: +30 210 772 3789
kgianna@central.ntua.gr

35. Multipoint Turbulence Structure and Modelling
Cambon, C.
ECL Ecully, France.
Tel: +33 472 186 161
Fax: +33 478 647 145
claude.cambon@ec-lyon.fr

36. Swirling Flows
Braza, M.
IMFT, France.
Tel: +33 534 322 839
Fax: +33 534 322 992
braza@imft.fr

37. Bio-Fluid Mechanics
Poelma, C.
Delft University of Technology, Holland.
Tel: +31 152 782 620
Fax: +31 152 782 947
c.poelma@tudelft.nl

38. Micro-thermofluidics
Borhani, N.
EPFL, Switzerland.
Tel: +41 216 933 503
Fax: +41 216 935 960
navid.borhani@epfl.ch

39. Aeroacoustics
Bailly, C.
Ecole Centrale de Lyon, France.
Tel: +33 472 186 014
Fax: +33 472 189 143
christophe.bailly@ec-lyon.fr

40. Smoothed Particle Hydrodynamics
Le Touze, D.
Ecole Centrale de Nantes, France
Tel: +33 240 371 512
Fax: +33 240 372 523
David.LeTouze@ec-nantes.fr

41. Fluid Structure Interaction
Longatte, E.
EDF, France.
Tel: +33 130 878 087
Fax: +33 130 877 727
elisabeth.longatte@edf.fr

42. Synthetic Models in Turbulence
Nicolleau, F.
University of Sheffield, England.
Tel: +44 114 222 7867
Fax: +44 114 222 7890
f.nicolleau@sheffield.ac.uk

43. Fibre Suspension Flows
Lundell, F.
The Royal Institute of Technology, Sweden.
Tel: +46 87 906 875
frederik@mech.kth.se

44. Fundamentals and Applications of Fractal Turbulence
Fortune, V.
Universit de Poitiers, France.
Tel: +33 549 454 044
Fax: +33 549 453 663
veronique.fortune@lea.univ-poitiers.fr

45. Uncertainty Quantification in Industrial Analysis and Design
Meyers, J.
Katholieke Universiteit Leuven, Belgium.
Tel: +32 163 225 02
Fax: +32 163 229 85
johan.meyers@mech.kuleuven.be

ERCOFTAC Pilot Centres

Alpe - Danube - Adria
Gergely, K.
Department of Fluid Mechanics,
Budapest University of Technology and
Economics
Bertalan L. utca 4-6
1111 Budapest, Hungary
Tel: +36 1 463 4073
Fax: +36 1 463 4072
kristof@ara.bme.hu

Belgium
Geuzaine, P.
Cenaero,
CFD Multi-physics Group,
Rue des Fréres Wright 29,
B-6041 Gosselies,
Belgium.
Tel: +32 71 919 334
philippe.geuzaine@cenaero.be

Czech Republic
Bodnar, T.
Institute of Thermomechanics AS CR,
5 Dolejskova,
CZ-18200 Praha 8,
Czech Republic.
Tel: +420 224 357 548
Fax: +420 224 920 677
bodnar@marian.fsik.cvut.cz

France - Henri Bénard
Cambon, C.
Ecole Centrale de Lyon.
LMFA, B.P. 163,
F-69131 Ecully Cedex,
France.
Tel: +33 4 72 18 6161
Fax: +33 4 78 64 7145
claude.cambon@ec-lyon.fr

France South
Braza, M.
IMF Toulouse,
CNRS UMR - 5502,
Allée du Prof. Camille Soula 1,
F-31400 Toulouse Cedex, France.
Tel: +33 534 322 839
Fax: +33 534 322 992
Braza@imft.fr

France West
Danaila, L.
CORIA, University of Rouen,
Avenue de l'Université BP12,
76801 Saint Etienne du Rouvray
France.
Tel: +33 232 953 702
luminita.danaila@coria.fr

Germany North
Gauger, N.R.
Computational Mathematics
Group
RWTH Aachen University
Schinkelstr. 2
D-52062 Aachen, Germany
Tel: +49 241 80 98 660
Fax: +49 241 80 92 600
gauger@mathcces.rwth-aachen.de

Germany South
Becker, S.
Universität Erlangen, IPAT
Cauerstr. 4
91058 Erlangen
Germany
Tel: +49 9131 85 29451
Fax: +49 9131 85 29449
sb@ipat.uni-erlangen.de

Greece
M. Founti.
National Tech. University Of Athens,
School of Mechanical Engineering,
Lab. of Steam Boilers and
Thermal Plants,
Heroon Polytechniou 9,
15780 Zografou, Athens, Greece
Tel: +30 210 772 3605
Fax: +30 210 772 3663
mfou@central.ntua.gr

Iberian East
Onate, E.
Universitat Politecnica de Catalunya,
Edificio C-1, Campus Norte,
Gran Capitan s/n,
E-08034 Barcelona,
Spain.
Tel: +34 93 401 6035
Fax: +34 93 401 6517
onate@cimne.upc.es

Iberian West
Theofilis, V.
Research Professor of Fluid Mechanics
School of Aerospace Engineering
Technical University of Madrid (UPM)
Tel: +34 91 336 3298
Fax: +34 91 336 3295
vassilios.theofilis@upm.es

Italy
Rispoli, F.
Universita di Roma "La Sapienza",
Roma, Italy
Tel: +39 064 458 5225
franco.rispoli@uniroma1.it

Netherlands
Ooms, G.
J.M. Burgerscentrum,
National Research School for Fluid
Mechanics,
Mekelweg 2,
NL-2628 CD Delft, Netherlands.
Tel: +31 15 278 1176
Fax: +31 15 278 2979
g.ooms@tudelft.nl

Nordic
Wallin, S.
Swedish Defence Research Agency FOI,
Information and Aeronautical Systems,
S-16490 Stockholm,
Sweden.
Tel: +46 8 5550 3184
Fax: +46 8 5550 3062
stefan.wallin@foi.se

Poland
Rokicki, J.
Warsaw University of Technology,
Inst. of Aeronautics & Applied
Mechanics,
ul. Nowowiejska 24,
PL-00665 Warsaw, Poland.
Tel: +48 22 234 7444
Fax: +48 22 622 0901
jack@meil.pw.edu.pl

Switzerland
Jenny, P.
ETH Zürich,
Institute of Fluid Dynamics,
Sonneggstrasse 3,
8092 Zürich, Switzerland.
Tel: +41 44 632 6987
jenny@ifd.mavt.ethz.ch

United Kingdom
Standingford, D.
Zenotech Ltd.
University Gate East, Park Row,
Bristol, BS1 5UB
England.
Tel: +44 117 302 8251
Fax: +44 117 302 8007
david.standingford@zenotech.com
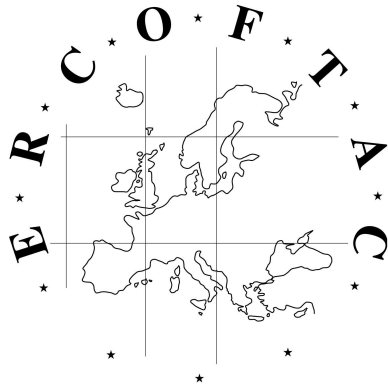
Best Practice Guidelines for Computational Fluid Dynamics of Dispersed Multi-Phase Flows

Editors

Martin Sommerfeld, Berend van Wachem
&
René Oliemans

The simultaneous presence of several different phases in external or internal flows such as gas, liquid and solid is found in daily life, environment and numerous industrial processes. These types of flows are termed multiphase flows, which may exist in different forms depending on the phase distribution. Examples are gas-liquid transportation, crude oil recovery, circulating fluidized beds, sediment transport in rivers, pollutant transport in the atmosphere, cloud formation, fuel injection in engines, bubble column reactors and spray driers for food processing, to name only a few. As a result of the interaction between the different phases such flows are rather complicated and very difficult to describe theoretically. For the design and optimisation of such multiphase systems a detailed understanding of the interfacial transport phenomena is essential. For single-phase flows Computational Fluid Dynamics (CFD) has already a long history and it is nowadays standard in the development of air-planes and cars using different commercially available CFD-tools.

Due to the complex physics involved in multiphase flow the application of CFD in this area is rather young. These guidelines give a survey of the different methods being used for the numerical calculation of turbulent dispersed multiphase flows. The Best Practice Guideline (BPG) on Computational Dispersed Multiphase Flows is a follow-up of the previous ERCOFTAC BPG for Industrial CFD and should be used in combination with it. The potential users are researchers and engineers involved in projects requiring CFD of (wall-bounded) turbulent dispersed multiphase flows with bubbles, drops or particles.

Table of Contents
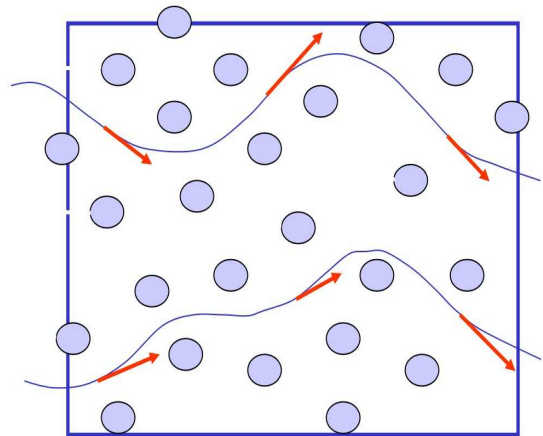
Copies of the Best Practice Guidelines can be acquired electronically from the ERCOFTAC website:

www.ercoftac.org

Or from:

ERCOFTAC CADO
Crown House
72 Hammersmith Road
London W14 8TH, United Kingdom

Tel: +44 207 559 1429
Fax: +44 207 559 1428
Email: magdalena.jakubczak@ercoftac.org

The price per copy (not including postage) is:

ERCOFTAC members

First copy	*Free*
Subsequent copies	75 Euros
Students	75 Euros

Non-ERCOFTAC academics	140 Euros
Non-ERCOFTAC industrial	230 Euros
EU/Non EU postage fee	10/17 Euros